sciendo

Contributions to Geophysics and Geodesy Vol. 49/2, 2019 (109–132)

Relaxation time spectra of basaltic lavas between 500–1150 °C reveal patterns of Kramers–Kronig inconsistency of the complex viscoelastic shear modulus

Martin BEDNÁRIK*, Igor KOHÚT

Earth Science Institute of the Slovak Academy of Sciences, Division of Geophysics, Dúbravská cesta 9, P. O. Box 106, 840 05 Bratislava, Slovak Republic

Abstract: An important, yet until now neglected, aspect of the viscoelastic behaviour of lavas is the Kramers–Kronig consistency of their complex viscoelastic shear modulus. The most general linear viscoelastic model – the generalized Maxwell body with continuous relaxation time spectrum – produces a consistent storage and loss modulus, as can be verified by Kramers–Kronig formulae. We reprocessed the original datasets of the high-precision laboratory data by *James et al. (2004)* supplied as pairs of magnitude of the complex viscoelastic shear modulus and the loss angle. We introduce the magnitude-borne and loss-angle-borne logarithmic relaxation time spectra and their ratio as a suitable indicator of the linear viscoelastic inconsistency. The basaltic lavas from Etna, Hawai'i and Vesuvius have shown a general convergence to the ideal consistency with increasing temperature, although each sample with an individual inconsistency pattern. The biggest surprise is the inconsistency ratio rising to ∼20 in Etna 1992 top sample at 786 °C. Such a high inconsistency level still waits for an explanation and for the discoveries of its class-mates either in laboratory or field experiments.

Key words: viscoelasticity, generalized Maxwell body, Kramers–Kronig relationships, relaxation time spectrum, viscoelastic modulus inconsistency

1. Introduction

The basis for our curret work is provided by the study of *James et al. (2004)*. The amount and the quality of the laboratory viscoelastic data prompted us to reprocess it again, focusing on the phenomenon of viscoelastic inconsistency not addressed in the original study. We shall briefly summarize its

*corresponding author: e-mail: geofmabe@savba.sk

doi: 10.2478/congeo-2019-0006

essence relevant to our study in the sequel.

The basaltic lava samples from Etna, Hawai'i and Vesuvius, heated up to temperatures between $\sim 500\,^{\circ}\mathrm{C}$ and $1150\,^{\circ}\mathrm{C}$ and fixed between Al rods of the apparatus (*Bagdassarov and Dingwell, 1993*), were subject to small forced harmonic torques ($\sim 10^{-3}\,\mathrm{N\,m}$) generated by a synthesiser at frequencies between 0.002 and 20 Hz. The angular deformation across the sample was measured by pairs of capacitive pick-ups responding to the movement of pure iron plates located at the ends of the Al wings of the rods. The shear modulus and phase difference between the applied torque and the angular displacement were calculated from the phase and amplitude parameters of the sinusoids fitted to the recorded signals.

Two samples from Etna were collected from lava erupted in 1992. One of these samples was taken from the top surface, the other one from the base ($\sim$10 cm down from the surface), and thus they represent samples with different cooling regimes. The surface sample has smaller vesicles (~ 0.2 to 0.5 mm, 15 to 20 vol. %) and smaller crystal content ($\sim$20 to 30 vol. %) than the basal sample ($\sim$20 vol. % of 1 to 2 mm vesicles and $\sim$30 vol. % phenocrysts). No chemical composition of the samples was given either by the study itself, or by precedent studies. A further sample was collected from near the south east cone in 1999, from the least vesicular area found in a recently emplaced flow near hornito H3 (*Calvari and Pinkerton, 2002*) at the top of the active flow field. The sample was used to study mainly the crack-healing-related phenomena. The Etna 1999 sample data were not included in the dataset made available to us by the authors.

The Hawai'ian basalt was sampled in the east rift eruption zone of Kilauea from a lava flow from a pahoehoe toe in September, 1984 (eruption temperature $\sim 1147\,^{\circ}\mathrm{C}$). This pahoehoe lava flow corresponds to the episode 25 of the eruption Pu'u 'O'o of Kilauea Volcano. Its chemical composition has been presented in *Garcia et al. (1992)* and *Bagdassarov (2000)*. The vesicularity varies around 50 vol. %. The sample has $\sim$10 vol. % of olivine quenched from magma during sampling and a few percent of other phenocrysts.

The Vesuvius samples were collected from the 1834 flow at Cava Ranieri approximately 6.3 km ESE of the central cone of Vesuvius by the group from University College of London. Chemical analysis of the samples is given in *Belkin et al. (1993)*. The same sample was also used by *Rocchi et al. (2004)*

in experiments to determine Young's modulus and tensile strength.

The most important findings of *James et al. (2004)* with respect to our study are the temporal variations in complex shear modulus and internal friction at $\sim 800\,^{\circ}\mathrm{C}$. They suggest that, over durations of up to 120 hours, structural adjustments were occurring within some of the samples. This time-varying behaviour of lava samples is attributed to the slow closing (healing) of microcracks resulting in the apparent stiffening of lava samples under annealing. Thus, those parts of lava flows that underwent slow cooling have more elastic properties. Regions which cool faster possess smaller shear moduli and higher internal friction due to thermal microcracking.

Since the publication of *James et al. (2004)*, several other studies on rheological properties of lavas and other geomaterials were performed using the methods of mechanical spectroscopy (bending and torsional tests). We shall list here the ones addressing the factors that influence viscoelasticity at various time scales, temperatures and pressures: *Wagner (2004), Fontaine et al. (2005), Fontaine et al. (2008), Okumura et al. (2010), Takei et al. (2011), McCarthy et al. (2011), Chien (2014)* and *Okumura et al. (2016)*. Some of them could serve as a source of data for potential future viscoelastic consistency tests.

2. Consistency of viscoelastic storage and loss shear modulus according to Kramers–Kronig relationships

A causal and time-invariant linear system shall have a complex frequency response (FR) whose real and imaginary parts are consistent, i.e. complying with Kramers–Kronig relationships. Let us test whether the linear viscoelastic shear modulus represented by the generalized Maxwell body fits into this category.

The shear stress response $\tau\,(t)$ of the linear viscoelastic shear modulus of the generalized Maxwell body with finite number of Maxwell modes to the unit step in engineering shear strain:

$$\gamma\,(t) = \gamma\,\theta(t)\,, \tag{1}$$

where γ is a constant and

$$\theta(t) = \begin{cases} 0 & \text{for } t < 0 \\ 1 & \text{for } t \geq 0 \end{cases},$$

is

$$\tau(t) = \begin{cases} 0 & \text{for } t < 0 \\ \gamma \sum_{n=0}^{N} g_n \exp\left(-t/\tau_n\right) & \text{for } t \geq 0 \end{cases}. \tag{2}$$

The Laplace transform of (1) and (2) yields $\gamma(s) = \gamma/s$ and $\tau(s) = \gamma \sum_{n=0}^{N} \frac{g_n \tau_n}{1 + s\tau_n}$, respectively. The shear modulus of the generalized Maxwell model then reads:

$$G(s) = \frac{\tau(s)}{\gamma(s)} = \gamma \sum_{n=0}^{N} \frac{g_n \tau_n}{1 + s\tau_n} \Big/ (\gamma/s) = \sum_{n=0}^{N} \frac{g_n \tau_n \, s}{1 + s\tau_n}. \tag{3}$$

For a viscoelastic solid, one of relaxation times τ_n is infinite. Let us choose $\tau_0 \to \infty$. Then:

$$G(s) = g_0 + \sum_{n=1}^{N} \frac{g_n \tau_n \, s}{1 + s\tau_n}. \tag{4}$$

The substitution of $s = \mathrm{j}\omega$ yields the complex shear modulus:

$$G(\mathrm{j}\omega) = g_0 + \sum_{n=1}^{N} \frac{g_n \tau_n^2 \, \omega^2 + \mathrm{j} g_n \tau_n \omega}{1 + \tau_n^2 \omega^2} \tag{5}$$

denoted also as $G^*(\omega)$. The relaxed modulus G_R and unrelaxed modulus G_U are:

$$G_R = \lim_{\omega \to 0} G(\mathrm{j}\omega) = g_0, \quad G_U = \lim_{\omega \to \infty} G(\mathrm{j}\omega) = \sum_{n=0}^{N} g_n = G_R + \sum_{n=1}^{N} g_n. \tag{6}$$

The real part of (5) is the storage modulus:

$$G'(\omega) = g_0 + \sum_{n=1}^{N} \frac{g_n \tau_n^2 \, \omega^2}{1 + \tau_n^2 \omega^2}, \tag{7}$$

the imaginary part is the loss modulus:

$$G''(\omega) = \sum_{n=1}^{N} \frac{g_n \tau_n \omega}{1 + \tau_n^2 \omega^2} \,. \tag{8}$$

Let us verify that the storage (7) and loss modulus (8) satisfy the Kramers–Kronig relationships (*Kronig, 1926; Kramers, 1927*):

$$G'(\omega) = \lim_{\omega \to \infty} G'(\omega) - \frac{2}{\pi} \, \mathrm{PV} \int_0^\infty \frac{\omega' \, G''(\omega') - \omega \, G''(\omega)}{\omega'^2 - \omega^2} \, \mathrm{d}\omega' \,, \tag{9}$$

$$G''(\omega) = \frac{2\omega}{\pi} \, \mathrm{PV} \int_0^\infty \frac{G'(\omega') - G'(\omega)}{\omega'^2 - \omega^2} \, \mathrm{d}\omega' \,, \tag{10}$$

where PV denotes the Cauchy principal value of the integral.

Before we substitute (7) and (8) to (9) and (10), let us note that:

$$\begin{aligned} \mathrm{PV} \int_0^\infty \frac{\mathrm{d}\omega'}{\omega'^2 - \omega^2} &= \lim_{\varepsilon \to 0^+} \left(\int_0^{\omega - \varepsilon} \frac{\mathrm{d}\omega'}{\omega'^2 - \omega^2} + \int_{\omega + \varepsilon}^\infty \frac{\mathrm{d}\omega'}{\omega'^2 - \omega^2} \right) = \\ &= \lim_{\varepsilon \to 0^+} \left(- \frac{\operatorname{arctanh}((\omega - \varepsilon)/\omega)}{\omega} + \frac{\operatorname{arctanh}(\omega/(\omega + \varepsilon))}{\omega} \right) = 0 \,. \end{aligned} \tag{11}$$

This means that in (9) and (10), any integrand with a constant numerator integrates to zero. The presence of the "null" terms (cf. e.g. *Rusu et al., 2005*) $-\dfrac{\omega \, G''(\omega)}{\omega'^2 - \omega^2}$ and $-\dfrac{G'(\omega)}{\omega'^2 - \omega^2}$ in (9) and (10), respectively, is a trick aimed at cancelling the singular term $\omega'^2 - \omega^2$ in the denominator of the integrand for suitably shaped $G'(\omega)$ and $G''(\omega)$, thus turning the integral from a singular into a non-singular one, as we shall see in the sequel.

The substitution of (7) and (8) to (9) yields:

$$\begin{aligned} G'(\omega) &= g_0 + \lim_{\omega \to \infty} \sum_{n=1}^{N} \frac{g_n \tau_n^2 \, \omega^2}{1 + \tau_n^2 \omega^2} - \frac{2}{\pi} \sum_{n=1}^{N} \int_0^\infty \frac{g_n \tau_n}{1 + \tau_n^2 \omega'^2} \mathrm{d}\omega' = \\ &= g_0 + \sum_{n=1}^{N} g_n - \frac{2}{\pi} \sum_{n=1}^{N} \frac{\pi \, g_n}{2 \, (1 + \tau_n^2 \omega^2)} = g_0 + \sum_{n=1}^{N} \frac{g_n \tau_n^2 \, \omega^2}{1 + \tau_n^2 \omega^2} \,, \end{aligned} \tag{12}$$

which is the same as (7). Similarly, the substitution of (7) to (10) yields (omitting the term g_0 in (7) which integrates to 0 according to (11)):

$$G''(\omega) = \frac{2\omega}{\pi}\sum_{n=1}^{N}\int_0^{\infty}\frac{g_n\tau_n^2}{1+\tau_n^2\omega'^2}\mathrm{d}\omega' = \frac{2\omega}{\pi}\sum_{n=1}^{N}\frac{\pi\, g_n\tau_n}{2\,(1+\tau_n^2\omega^2)} = \sum_{n=1}^{N}\frac{g_n\tau_n\omega}{1+\tau_n^2\omega^2}, \quad (13)$$

which is the same as (8).

Thus, according to the Kramers–Kronig relationships, the storage and loss modulus of a viscoelastic solid with a finite number of Maxwell modes uniquely determine each other.

For $\tau_n > 0$, $G(s)$ is a minimum-phase function and $\ln G(s)$ is analytic for $Re(s) > 0$. Then the logarithm of the magnitude $\alpha(\omega) = \ln|G^*(\omega)|$ and the phase $\varphi(\omega)$ in $\ln G^*(\omega) = \alpha(\omega) + \mathrm{j}\varphi(\omega)$ form also a unique pair of functions (except for a constant term in $\alpha(\omega)$) coupled for instance by Bayard–Bode relationships (*Bode, 1945*):

$$\varphi(\omega) = \frac{1}{\pi}\int_{-\infty}^{\infty}\frac{\mathrm{d}\alpha(u)}{\mathrm{d}u}\,\ln\coth\frac{|\,u\,|}{2}\mathrm{d}u \quad (14)$$

and

$$\alpha(\omega) = \lim_{\omega\to 0}\alpha(\omega) - \frac{1}{\pi}\int_{-\infty}^{\infty}\frac{\mathrm{d}\,(\varphi(u)/\exp(u))}{\mathrm{d}u}\,\ln\coth\frac{|\,u\,|}{2}\mathrm{d}u \quad (15)$$

or

$$\alpha(\omega) = \lim_{\omega\to\infty}\alpha(\omega) - \frac{1}{\pi}\int_{-\infty}^{\infty}\frac{\mathrm{d}\,(\varphi(u)\exp(u))}{\mathrm{d}u}\,\ln\coth\frac{|\,u\,|}{2}\mathrm{d}u\,, \quad (16)$$

where $u = \ln(\omega'/\omega)$.

The reader can try to apply the formulae (14), (15) and (16) to $\alpha(\omega)$ and $\varphi(\omega)$ of a viscoelastic model with finite number of Maxwell modes only to discover that they fail to yield closed symbolic forms of the integrals. If we are not interested in asymptotic estimates, but in exact general transformations between $\alpha(\omega)$ and $\varphi(\omega)$ of a generalized Maxwell model with discrete

modes, the Bayard–Bode formulae are practically useless. In the next section, we shall offer alternative formulae practically applicable to generalized Maxwell body with both discrete and continuous relaxation spectrum and suitable for testing the consistency of $\alpha(\omega)$ and $\varphi(\omega)$.

3. Methods

3.1. Relaxation time spectra as consistency test tools

The formulae (7) and (8) could be used to extract the discrete spectra g_n, $n \in \{0, 1, \ldots, N\}$ for each of the sampled functions $G'(\omega)$, $G''(\omega)$ separately. The respective discrete spectra g'_n and g''_n could then be compared to assess the inconsistency of $G'(\omega)$ and $G''(\omega)$. The difficulty with the discrete spectra is the arbitrariness of both input sampling of $G'(\omega)$ and $G''(\omega)$ in frequency domain and output sampling of $g'_n(\tau_n)$ and $g''_n(\tau_n)$ in the domain of relaxation times, resulting in non-uniqueness and non-representativeness of the latter. Moreover, the formulae (7) and (8) do not have a form suitable for an effective numerical implementation of the inversion process, with a high potential of its failure.

We shall present a solution of this problem based on widely used continuous logarithmic relaxation spectra, comprehensively presented e.g. in *Ferry (1980)*. The shear stress response of a viscoelastic solid with continuous relaxation spectrum $H(\ln\tau)$ to unit step (1) is:

$$\tau(t) = \begin{cases} 0 & \text{for } t < 0 \\ \gamma\left(g_0\,\theta(t) + \int\limits_{-\infty}^{\infty} H(\ln\tau)\exp\left(-t/\tau\right)\mathrm{d}(\ln\tau)\right) & \text{for } t \geq 0 \end{cases}. \tag{17}$$

After performing the Laplace transform, the shear modulus in the s-domain is:

$$G(s) = g_0 + \int\limits_{-\infty}^{\infty} \frac{s\,\tau\,H(\ln\tau)}{1 + s\,\tau}\,\mathrm{d}(\ln\tau) \tag{18}$$

and the storage and loss modulus are:

$$G'(\omega) = g_0 + \int_{-\infty}^{\infty} \frac{\omega^2 \tau^2 H(\ln \tau)}{1 + \omega^2 \tau^2} \, \mathrm{d}(\ln \tau) \,, \tag{19}$$

$$G''(\omega) = \int_{-\infty}^{\infty} \frac{\omega \tau H(\ln \tau)}{1 + \omega^2 \tau^2} \, \mathrm{d}(\ln \tau) \,. \tag{20}$$

Now it is natural to introduce the logarithmic frequency and relaxation time variables Ω, Θ (T cannot be used because it shall denote temperature). The substitution of $\tau = \exp(\Theta)$ and $\omega = \exp(\Omega)$ yields:

$$G'(\Omega) = g_0 + \int_{-\infty}^{\infty} \frac{\exp(2\Omega + 2\Theta) \, H(\Theta)}{1 + \exp(2\Omega + 2\Theta)} \, \mathrm{d}\Theta \,, \tag{21}$$

$$G''(\Omega) = \int_{-\infty}^{\infty} \frac{\exp(\Omega + \Theta) \, H(\Theta)}{1 + \exp(2\Omega + 2\Theta)} \, \mathrm{d}\Theta \,. \tag{22}$$

The kernel of the integral in (22):

$$K''(\Omega, \Theta) = \frac{\exp(\Omega + \Theta)}{1 + \exp(2\Omega + 2\Theta)} \tag{23}$$

is, for a fixed Θ, a bell-shaped function of Ω. The bell has its maximum at $\Omega_C = -\Theta$ and is exactly symmetric with respect to Ω_C. This bell shape is of utmost importance for the numerical implementation of the $G''(\Omega)$ to $H(\Theta)$ inversion. On the other hand, the kernel of the integral in (21)

$$K'(\Omega, \Theta) = \frac{\exp(2\Omega + 2\Theta)}{1 + \exp(2\Omega + 2\Theta)} \tag{24}$$

has an unpleasant form of a smoothened ramp growing from 0 to 1 as Ω goes from $-\infty$ to ∞.

The desired bell-shaped kernel appears in:

$$\begin{aligned} \frac{\mathrm{d}G'(\Omega)}{\mathrm{d}\Omega} &= \int_{-\infty}^{\infty} \frac{\mathrm{d}}{\mathrm{d}\Omega} \left(\frac{\exp(2\Omega + 2\Theta)}{1 + \exp(2\Omega + 2\Theta)} \right) H(\Theta) \mathrm{d}\Theta = \\ &= \int_{-\infty}^{\infty} \frac{2 \exp(2\Omega + 2\Theta)}{(1 + \exp(2\Omega + 2\Theta))^2} \, H(\Theta) \mathrm{d}\Theta \,. \end{aligned} \tag{25}$$

In this case, the kernel

$$\frac{\mathrm{d}K'(\Omega,\Theta)}{\mathrm{d}\Omega} = \frac{2\exp(2\Omega+2\Theta)}{(1+\exp(2\Omega+2\Theta))^2} \tag{26}$$

forms a bell centred at $\Omega_C = -\Theta$ and exactly symmetric with respect to Ω_C. Compared to (23), the bell (26) is narrower.

The main idea of the $G''(\Omega)$ to $H(\Theta)$ and $\dfrac{\mathrm{d}G'(\Omega)}{\mathrm{d}\Omega}$ to $H(\Theta)$ inversion is based on the fact that due to the bell shape of the respective kernel, the value $H(\Theta)$ influences the functions $G''(\Omega)$, $\dfrac{\mathrm{d}G'(\Omega)}{\mathrm{d}\Omega}$ mainly at $\Omega = -\Theta$. The details will be provided in the section 3.2.

The experimental data from the harmonic measurements of the viscoelastic (shear) modulus are very often supplied in the form of samples of the magnitude of the complex modulus $|G^*(\omega)|$ and of the loss angle $\varphi(\omega)$. Both these datasets are likely to be contaminated by measurement errors characteristic to each of them. Computing $G'(\omega)$, $G''(\omega)$ out of $|G^*(\omega)|$, $\varphi(\omega)$ would produce an undesirable mixture of errors of $|G^*(\omega)|$ and $\varphi(\omega)$. An ideal approach to $|G^*(\omega)|$, $\varphi(\omega)$ is therefore their totally separate processing. We have realized that the Bayard–Bode relationships do not provide a reasonable option for the direct test of consistency of $|G^*(\omega)|$, $\varphi(\omega)$. We shall show that there is a viable alternative approach very similar to the use of relaxation time spectrum $H(\Theta)$ in (22) and (25).

Just for the purpose of a short derivation within this paragraph, let us consider the complex viscoelastic modulus $G^*_{01}(\omega)$ containing only the 0-th and the 1-st Maxwell mode. To avoid a variable confusion in the sequel, let us change g_0, g_1 to k_0, k_1 in advance. Then the modulus reads:

$$G^*_{01}(\omega) = k_0 + \frac{\omega^2\tau^2 k_1 + \mathrm{j}\omega\tau_1 k_1}{1+{\tau_1}^2\omega^2}\,. \tag{27}$$

The tangent of its phase $\tan\varphi_{01}(\omega)$, where

$$\varphi_{01}(\omega) = \arctan\frac{\omega\tau_1 k_1/k_0}{1+\omega^2\tau_1^2\,(1+(k_1/k_0))}\,, \tag{28}$$

has the same structure as the rational function $\dfrac{g_n\tau_n\omega}{1+\tau_n^2\omega^2}$ – the summand of (8). Let us introduce $p_1 = k_1/k_0$ and compare the rational functions in (8) and (28) term by term: $g_n\tau_n = p_1\tau_1$, $\tau_n^2 = \tau_1^2\,(1+p_1)$. Then

$$p_1 = \left(g_n^2 + g_n\sqrt{4+g_n^2}\right)\Big/ 2 \tag{29}$$

and

$$\tau_1 = \tau_n \Big/ \sqrt{(1+p_1)} \tag{30}$$

transform (28) to

$$\varphi_n(\omega) = \arctan\frac{g_n\tau_n\omega}{1+\tau_n^2\omega^2}\,, \tag{31}$$

which can be summed to the total phase

$$\varphi(\omega) = \sum_{n=1}^{N} \arctan\frac{g_n\tau_n\omega}{1+\tau_n^2\omega^2}\,. \tag{32}$$

Here, unlike in (8), g_n is dimensionless. Analogically to the transition from discrete (8) to continuous (20) representation, we can introduce a dimensionless relaxation time spectrum $h(\Theta)$ and write:

$$\varphi(\Omega) = \int_{-\infty}^{\infty} \arctan\frac{\exp(\Omega+\Theta)\,h(\Theta)}{1+\exp(2\Omega+2\Theta)}\mathrm{d}\Theta\,. \tag{33}$$

We have to substitute (29) and (30) also to $G_{01}^*(\omega)$ in (27), denote $|G_n^*(\omega)|$ $= |G_{01}^*(\mathrm{j}\omega)|$ and express it in terms of k_0, g_n and τ_n:

$$|G_n^*(\omega)| = k_0\sqrt{1+\frac{g_n^2}{2}+\frac{g_n}{2}\sqrt{4+g_n^2}}\,\exp\left(\operatorname{arctanh}\frac{g_n\tanh(\ln\omega\tau_n)}{\sqrt{4+g_n^2}}\right). \tag{34}$$

Alternatively, after the substitution of

$$p_2 = k_1 \Big/ (k_0+k_1) = \left(-g_n^2 + g_n\sqrt{4+g_n^2}\right)\Big/ 2\,, \tag{35}$$

$$\tau_1 = \tau_n \Big/ \sqrt{(1-p_2)}\,, \tag{36}$$

$$|G_n^*(\omega)| = (k_0 + k_1)\sqrt{1 + \frac{g_n^2}{2} - \frac{g_n}{2}\sqrt{4 + g_n^2}} \times \\ \times \exp\left(\operatorname{arctanh}\frac{g_n \tanh(\ln \omega\tau_n)}{\sqrt{4 + g_n^2}}\right). \tag{37}$$

Then the total magnitude of the shear modulus corresponding to the total phase $\varphi(\omega)$ (32) is:

$$|G_n^*(\omega)| = G_R \prod_{n=1}^{N} \sqrt{1 + \frac{g_n^2}{2} + \frac{g_n}{2}\sqrt{4 + g_n^2}} \times \\ \times \exp\left(\operatorname{arctanh}\frac{g_n \tanh(\ln \omega\tau_n)}{\sqrt{4 + g_n^2}}\right). \tag{38}$$

or

$$|G_n^*(\omega)| = G_U \prod_{n=1}^{N} \sqrt{1 + \frac{g_n^2}{2} - \frac{g_n}{2}\sqrt{4 + g_n^2}} \times \\ \times \exp\left(\operatorname{arctanh}\frac{g_n \tanh(\ln \omega\tau_n)}{\sqrt{4 + g_n^2}}\right). \tag{39}$$

In the case of continuous relaxation spectrum $h(\Theta)$ as in (33) (in the sequel, denoted as h for brevity), the integral forms corresponding to the latter two expressions are:

$$\ln|G_n^*(\Omega)| = \ln G_R + \frac{1}{2}\int_{-\infty}^{\infty} \ln\left(1 + \frac{h^2}{2} + \frac{h}{2}\sqrt{4 + h^2}\right) \mathrm{d}\Theta + \\ + \int_{-\infty}^{\infty} \operatorname{arctanh}\frac{h \tanh(\Omega + \Theta)}{\sqrt{4 + h^2}}\, \mathrm{d}\Theta\,, \tag{40}$$

$$\ln|G_n^*(\Omega)| = \ln G_U + \frac{1}{2}\int_{-\infty}^{\infty} \ln\left(1 + \frac{h^2}{2} - \frac{h}{2}\sqrt{4 + h^2}\right) \mathrm{d}\Theta + \\ + \int_{-\infty}^{\infty} \operatorname{arctanh}\frac{h \tanh(\Omega + \Theta)}{\sqrt{4 + h^2}}\, \mathrm{d}\Theta\,. \tag{41}$$

Similarly to the kernel $K'(\Omega,\Theta)$ in (24), also the integrand

$$K(\Omega,\Theta)=\operatorname{arctanh}\frac{h\tanh(\Omega+\Theta)}{\sqrt{4+h^2}} \tag{42}$$

is a smooth ramp-like function of Ω. Therefore, for the purpose of $|G^*(\omega)|$ to $h(\Theta)$ inversion, we have to use the formula:

$$\frac{\mathrm{d}\ln|G^*(\Omega)|}{\mathrm{d}\Omega}=\int_{-\infty}^{\infty}\frac{\mathrm{d}K(\Omega,\Theta)}{\mathrm{d}\Omega}\,\mathrm{d}\Theta=\int_{-\infty}^{\infty}\frac{h\sqrt{4+h^2}}{2+h^2+2\cosh 2(\Omega+\Theta)}\,\mathrm{d}\Theta\,. \tag{43}$$

The integrand $\mathrm{d}K(\Omega,\Theta)/\mathrm{d}\Omega$ is a symmetric bell-shaped function of Ω centred at $-\Theta$. Once $h(\Theta)$ is known, it can be supplied back to (40) and (41) to yield G_R and G_U, respectively. The first terms in (40) and (41) are analogical to (9) in Kramers–Kronig or (15) and (16) in Bayard–Bode relationships, since $G_R=\lim\limits_{\omega\to 0}|G^*(\omega)|$, $G_U=\lim\limits_{\omega\to\infty}|G^*(\omega)|$ (cf. (6)). Note that G_R and G_U can be evaluated at any Ω. Their constancy over the frequency range indicates the quality of the inversion.

The quantity $h(\Theta)$ does not meet all usual expectations of a spectrum. The integral transformations (33) and (43) are (unlike (22)) non-separable into the classical spectral form $\int\limits_{-\infty}^{\infty}k(\Omega,\Theta)\,h(\Theta)\mathrm{d}\Theta$ and nonlinear in $h(\Theta)$. For our numerical implementation of the $h(\Theta)$ search, this is not a problem, as far as rough proportionality (the greater $h(\Theta)$, the greater $\varphi(-\Theta)$) is preserved. The phase $\varphi(\Omega)$ and the spectrum $h(\Theta)$ have roughly the same order of magnitude (cf. 52). For crustal rocks then $\varphi(\Omega)\to 0$, $h(\Theta)\to 0$. The reader can expand the functions used in the expressions (33) and (43) in Taylor series to see that for $h(\Theta)\to 0$ they converge to the usual integral transformation $\int\limits_{-\infty}^{\infty}k(\Omega,\Theta)\,h(\Theta)\mathrm{d}\Theta$.

In experimental practice, the formulae (22) and (25) give different $H(\Theta)$ spectra and the formulae (43) and (33) give different $h(\Theta)$ spectra. Therefore, we will speak of $G'(\omega)$-, $G''(\omega)$-, $|G^*(\omega)|$- and $\varphi(\omega)$-borne relaxation spectra and denote them accordingly: $H'(\Theta)$, $H''(\Theta)$, $h_{|G^*|}(\Theta)$ and $h_\varphi(\Theta)$. The method of *Winter (1997)*, giving a single discrete parsimonious spectrum for jointly inverted $G'(\omega)$, $G''(\omega)$ would be the less successful, the less $G'(\omega)$ and $G''(\omega)$ comply with Kramers–Kronig relationships.

With the introduction of the unscaled relaxation time spectrum $h(\Theta)$, we filled the grey field in the table of inversion schemes for viscoelastic consistency tests (Table 1).

Table 1. Inversion methods for viscoelastic consistency tests.

inversion	direct	via spectrum
$G'(\omega) \leftrightarrow G''(\omega)$	Kramers–Kronig	standard $G'(\omega) \leftrightarrow H(\Theta) \leftrightarrow G''(\omega)$
$\ln \lvert G^*(\omega)\rvert \leftrightarrow \varphi(\omega)$	Bayard–Bode	our solution $\ln \lvert G^*(\omega)\rvert \leftrightarrow h(\Theta) \leftrightarrow \varphi(\omega)$

The measured and Kramers–Kronig inverted moduli $G'(\omega)$, $G''(\omega)$ are not as suitable consistency test tools as the relaxation time spectra $H(\Theta)$ or $h(\Theta)$ because of the ambiguity, which of $G'(\omega)$, $G''(\omega)$ shall be preferred as the comparison basis.

3.2. Numerical implementation of the consistency test based on the relaxation spectra

The numerical implementation of the spectral consistency test can be divided into three parts: data pre-processing, their inversion to spectra and the post-processing of spectra to retrieve additional characteristics (G_R, G_U, misfits of the spectra etc.). All the stages are implemented in a script in the computational environment Mathematica® by Wolfram Research.

We shall first describe the inversion itself, because it poses requirements to the input data to be met in the pre-processing stage. As an example, let us explain the inversion of $G''(\Omega)$ to $H(\Theta)$. The integral $G''(\Omega) = \int_{-\infty}^{\infty} \frac{\exp(\Omega+\Theta)\, H(\Theta)}{1+\exp(2\Omega+2\Theta)} \mathrm{d}\Theta$ (22) shall first be discretized. The infinitesimal integration step $\mathrm{d}\Theta$ shall be approximated by constant finite step $\Delta\Theta$ and the infinite integration range shall be approximated by finite range $\langle \Theta_{\min}, \Theta_{\max} \rangle$ such that $\langle -\Omega_{\max}, -\Omega_{\min} \rangle \subset \langle \Theta_{\min}, \Theta_{\max} \rangle$, where $\langle \Omega_{\min}, \Omega_{\max} \rangle$ is the frequency range of the $G''(\Omega)$ data. Typically, $\Theta_{\min} \approx -2\,\Omega_{\max}$, $\Theta_{\max} \approx -2\,\Omega_{\min}$. The original $G''(\Omega)$ must be extrapolated to the range $\Omega \in \langle -\Theta_{\max}, -\Theta_{\min} \rangle$.

The inversion shall be iterative according to the cyclic scheme:

$$G_i''(\Omega) = \sum_{n=1}^{N} \frac{\exp(\Omega + \Theta_n)\, H_{i-1}(\Theta_n)}{1 + \exp(2\Omega + 2\Theta_n)} \Delta\Theta\,, \tag{44}$$

$$c_i(\Theta_n) = G''(-\Theta_n) \Big/ G_i''(-\Theta_n)\,, \tag{45}$$

$$H_i(\Theta_n) = c_i(\Theta_n)\, H_{i-1}(\Theta_n)\,, \tag{46}$$

where i denotes the iteration number starting with $i = 1$. The $H_0(\Theta_n) = 1$ for all n can be used as start model. The ratio (45) of the original (inter- or extrapolated) data to their i-th synthetic approximation (44) gives the correction coefficients $c_i(\Theta_n)$ that will improve the estimate of $H_i(\Theta_n)$ (46). In (44), Mathematica allows us to use symbolic, continuous representation of $G_i''(\Omega)$.

With $G''(\Omega) \geq 0$ and $H_0(\Theta_n) > 0$, the repetition of (44÷46) can never arrive at $H_i(\Theta_n) < 0$. The correction coefficients themselves provide a suitable convergence criterion, as:

$$\lim_{i\to\infty} c_i(\Theta_n) = \begin{cases} 1 & \text{for } \mathrm{G''(-\Theta_n) > 0} \\ \\ 0 & \text{for } \mathrm{G''(-\Theta_n) = 0} \end{cases}. \tag{47}$$

At $c_i(\Theta_n)$ approaching to either 1 or 0 for all n, the best possible approximation of $G_i''(\Omega)$ to $G''(\Omega)$ and $H_i(\Theta_n)$ to $H(\Theta_n)$ will be achieved within the bounds of the discretization and integration range truncation errors.

The convergence can be accelerated by a correction predictor more courageous than (45):

$$c_i(\Theta_n) = \Big(G''(-\Theta_n) \Big/ G_i''(-\Theta_n)\Big)^{\beta}\,, \tag{48}$$

where $\beta \in \langle 1, 2)$. As β approaches 2, the more uneven (oscillatory) the convergence is. At $\beta = 2$, the process diverges.

The schemes of inversion of other FRs to their respective time relaxation spectra are analogical to (44÷46).

The preprocessing should supply easily invertible data. We have to assure that $G''(\Omega) \geq 0$, $\dfrac{\mathrm{d}G'(\Omega)}{\mathrm{d}\Omega} \geq 0$, $\varphi(\Omega) \geq 0$, $\dfrac{\mathrm{d}\ln|G^*(\Omega)|}{\mathrm{d}\Omega} \geq 0$. It is usually not a problem with the first and third quantity in the list, but in $G'(\Omega)$,

$\ln|G^*(\Omega)|$ it often happens that on a part of their frequency range, they decrease with frequency. There, the negative values of $\dfrac{\mathrm{d}G'(\Omega)}{\mathrm{d}\Omega}$, $\dfrac{\mathrm{d}\ln|G^*(\Omega)|}{\mathrm{d}\Omega}$ shall be replaced by 0.

The truncation of the integration range is based on the assumptions $\lim\limits_{\Theta\to-\infty} H(\Theta) = 0$, $\lim\limits_{\Theta\to\infty} H(\Theta) = 0$, $\lim\limits_{\Theta\to-\infty} h(\Theta) = 0$, $\lim\limits_{\Theta\to\infty} h(\Theta) = 0$. If we want $H(\Theta)$, $h(\Theta)$ to go to zero already at $\Theta_{\min}$, $\Theta_{\max}$, we have to make sure that $G''(\Omega)$, $\dfrac{\mathrm{d}G'(\Omega)}{\mathrm{d}\Omega}$, $\varphi(\Omega)$, $\dfrac{\mathrm{d}\ln|G^*(\Omega)|}{\mathrm{d}\Omega}$ also go to zero at $\Omega = -\Theta_{\max}$, $\Omega = -\Theta_{\min}$. If it is not the case with the original (extrapolated) data, we have to apply band-pass filtering. A very abrupt transition from nonzero to (almost) zero values is not desirable, as it produces truncation artefacts in the relaxation spectrum. The filter must therefore offer a good trade-off between suppression in the stopband and smoothness around the cut-off frequencies.

We have very good experiences with the band-pass filter of the type:

$$F(\Omega-\Omega_0) = \left(1+\sqrt{\left(\frac{\Omega-\Omega_0}{\Omega_{thr}}\right)^{2n}}\right)^{-1}, \tag{49}$$

where Ω_0 is the central frequency of the passband and Ω_{thr} is the cut-off frequency. $F(\Omega-\Omega_0)$ is an even function of $\Omega-\Omega_0$ even for an odd n, thus widening the set of candidates for its optimum order.

The lower are n and Ω_{thr}, the more the filter influences the data in the middle of the passband. As a consequence, the relaxation spectrum of the filtered FR may considerably differ from that of the original FR even in the passband. To minimize this effect, the original FR should be pre-deformed with the reciprocal band-stop filter and only then fitted by a polynomial of a suitably low order.

Let us denote the original data generally as $D(\Omega-\Omega_0)$. We have to produce the pre-deformed data:

$$D_{BS}(\Omega-\Omega_0) = D(\Omega-\Omega_0)\Big/F(\Omega-\Omega_0)\,, \tag{50}$$

and fit it by the polynomial $P(\Omega-\Omega_0)$.

Then the optimal continuous representation of the original data within the passband of the filter is:

$$D_{BP}(\Omega - \Omega_0) = P(\Omega - \Omega_0)F(\Omega - \Omega_0)\,. \tag{51}$$

In the passband, the band-stop filter implicitly present in the pre-deformed data (50) cancels with the explicitly present band-pass filter in (51). In the stopbands, the band-pass filter prevails and suppresses the original FR. The main idea is very similar to that of pre-emphasis – de-emphasis signal processing.

When filtering $\ln|G^*(\Omega)|$, $G'(\Omega)$ or $\int\varphi(\Omega)$, $\int G''(\Omega)$, the order of the fitting polynomial $P(\Omega - \Omega_0)$ shall be equal to that of the filter (49). The desired band-pass filtering effect becomes obvious after the differentiation of the former quantities. In the stopbands, the values of derivatives will be negative and replaced by zero. If we accept a non-ideal stopband suppression, it is possible to fit $\varphi(\Omega)$ and $G''(\Omega)$ directly as well. The polynomials that fit them must then be of a lower order than the filter (49).

The lower n, the smoothest the transition from non-zero to zero values is and the smaller the cut-off artefacts in the corresponding spectra are.

Applying the same kind of filtering (51) to both sides of the couple subject to Kramers–Kronig relationships introduces their violation. This violation is however relevant only to the stopbands, where we do not expect to have any useful data.

A cleaner trick to suppress the stopbands is to subtract from the filtered FR a constant, whose equivalent in terms of constant ΔH or Δh we shall return to $H(\Theta)$ or $h(\Theta)$, respectively, at the very end. For instance, according to:

$$\Delta G'' = \int_{-\infty}^{\infty} \frac{\exp(\Omega + \Theta)\,\Delta H}{1 + \exp(2\Omega + 2\Theta)}\,\mathrm{d}\Theta = \frac{\pi}{2}\,\Delta H\,, \tag{52}$$

a constant $\Delta G''$ subtracted from $G''(\Omega)$ shall be compensated by a constant $\Delta H = 2\Delta G''/\pi$ added to $H(\Theta)$. The negative values of thus lowered $G''(\Omega)$ are replaced by 0. This operation does not introduce any inconsistency with Kramers–Kronig relationships and is physically justified: a nonzero constant extrapolation of $H(\Theta)$ or $h(\Theta)$ to the zones not covered by data may be a more realistic estimate than their zero extrapolation. If we apply the same procedure to the linearized version of (33), we get $\Delta h = 2\Delta\varphi/\pi$. Similarly, we obtain also $\Delta H = \Delta\,(\mathrm{d}G'/\mathrm{d}\Omega)$, $\Delta h = \Delta\,(\mathrm{d}\ln|G^*(\Omega)|/\mathrm{d}\Omega)$.

One of the roles of the post-processing is to provide an independent check of the iteration outcome. Once $H(\Theta)$ is known, from (21) we yield $G_R = g_0$, which shall be constant over $\langle \Omega_{\min}, \Omega_{\max} \rangle$. For this purpose G_U can be used, as well. Its calculation requires G_R, though:

$$G_U = \lim_{\Omega \to \infty} G'(\Omega) = G_R + \int_{-\infty}^{\infty} H(\Theta)\, \mathrm{d}\Theta\,. \tag{53}$$

Once $h(\Theta)$ is known, the formulae (40) and (41) can be used to obtain G_R and G_U, respectively. G_R and G_U and can be used as indicators of the consistency, as well. For this purpose, the spectra couples shall be obtained by compatible procedures, resulting in their nearly equal range of non-zero values.

An important part of the post-processing is the presentation of the results. The ratios $H'(\Theta)/H''(\Theta)$ and $h_{|G^*|}(\Theta)/h_\varphi(\Theta)$ or their reciprocals are particularly suitable for the inconsistency assessment provided the division by zero is avoided either by the subtract-return pre-processing or some other suitable means.

4. Results

The $h_{|G^*|}(\Theta)/h_\varphi(\Theta)$ ratios of the samples Etna 1992 top, Etna 1992 base, Hawai'i and Vesuvius are presented in Fig. 1 to 4. They are almost identical with the respective $H'(\Theta)/H''(\Theta)$ ratios. Therefore, the latter will not be presented here. The feature common to all samples is the convergence of $h_{|G^*|}(\Theta)/h_\varphi(\Theta)$ to 1 (ideal linear viscoelasticity) with the temperature increasing to the melting point.

At 500–600 °C, the scatter of the measured FRs allows for a large arbitrariness of their fits. Thus, the evidence for the convergence to ideal linear anelasticity with the temperature decrease is rather weak, but still visible in the case of Etna 1992 top. The biggest surprise is the very large $h_{|G^*|}(\Theta)/h_\varphi(\Theta)$ ratio (almost 20) of the Etna 1992 top sample at 786 °C. The measured $|G^*(\omega)|$, $\varphi(\omega)$ at 786 °C are very smooth and raise no doubts about their reliability. The batman-shaped transitions in $h_{|G^*|}(\Theta)/h_\varphi(\Theta)$ are due to the band-pass filtering of $\ln|G^*(\Omega)|$ and narrow kernel in (43).

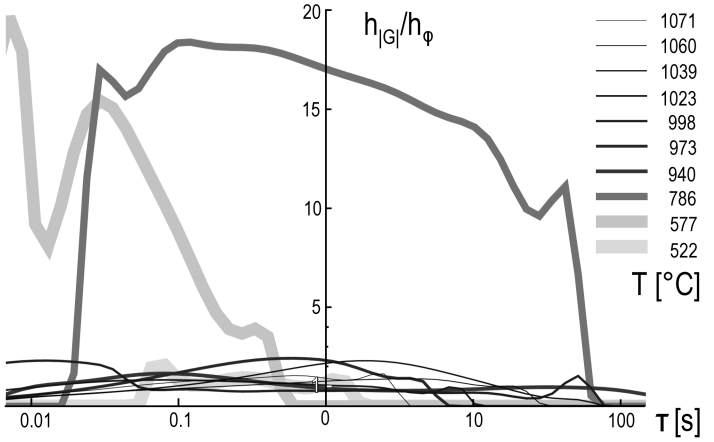

Fig. 1. Linear viscoelastic consistency of the Etna 1992 top sample.

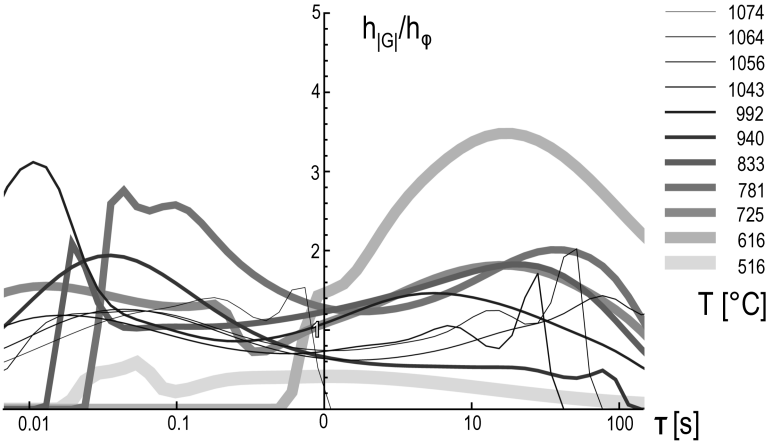

Fig. 2. Linear viscoelastic consistency of the Etna 1992 base sample.

The effects of $\varphi(\Omega)$ filtering on $h_\varphi(\Theta)$ are broader transitions without ringing, because the kernel in (33) is broader than in (43). Still, the filtering artefact is rather local and does not contaminate the whole spectrum. For the purpose of independent spectrum retrieval by the reader, we attached the source data of the Etna 1992 top sample in the Appendix (Table 2).

Similar, but not that pronounced inconsistencies can be seen in the samples Etna 1992 base ($h_{|G^*|}(\Theta)/h_\varphi(\Theta) \to 4$ already at 616 °C) and Hawai'i

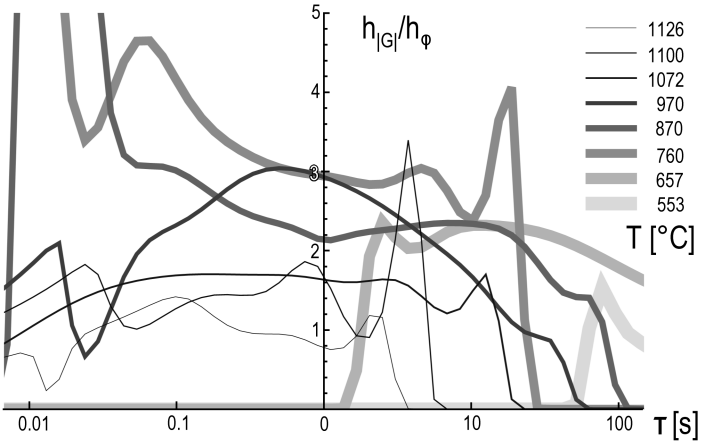

Fig. 3. Linear viscoelastic consistency of the Hawai'i sample.

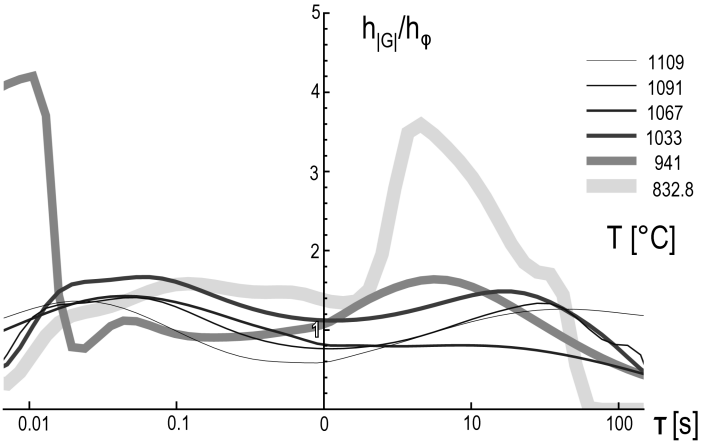

Fig. 4. Linear viscoelastic consistency of the Vesuvius sample.

$(h_{|G^*|}(\Theta)/h_\varphi(\Theta) \to 3$ at 760 °C and 870 °C). In the case of Vesuvius, the peak $h_{|G^*|}(\sim 4\,\mathrm{s})/h_\varphi(\sim 4\,\mathrm{s}) \to 4$ at 832.8 °C (Fig. 4) is an artefact due to a sudden drop of $h_\varphi(\Theta)$ to the Δh_φ baseline, while $h_{|G^*|}(\Theta)$ continues its smooth run.

While the transition of the samples Etna 1992 and Vesuvius to the full consistency comes rather suddenly above ~ 900 °C, the Hawai'i sample shows a more smooth decrease to $h_{|G^*|}(\Theta)/h_\varphi(\Theta) = 1$. The curiosity of

the Hawai'i dataset at 553 °C is $|G^*(\omega)|$ decreasing with frequency almost on the whole range of ω. Such behaviour is totally incompatible with the generalized Maxwell model. Therefore, we have a flat zero line of $h_{|G^*|}(\Theta)/h_\varphi(\Theta)$ at 553 °C in Fig. 3. At lower temperatures, the decrease of $|G^*(\omega)|$ happens occasionally also in other samples and causes $h_{|G^*|}(\Theta)/h_\varphi(\Theta)$ to drop to zero. In Fig. 3 we also see the gradual retreat of the curves from lower frequencies with increasing temperature. This is due to an experimental fact mentioned by *James et al. (2004)* – at lower frequencies, the sample started to flow.

The best consistency is shown by the Vesuvius sample, owing also to the fact that the measurements start there only as high as at 832.8 °C.

5. Discussion

The unexpected discovery of viscoelastic inconsistency as large as 20 in terms of $h_{|G^*|}(\Theta)/h_\varphi(\Theta)$ ratio in Etna 1992 top sample demonstrates the importance of prompt consistency screening of any data deemed to be generated by a linear system. An early discovery by the authors themselves would have incited a thorough search for a possible error. With the error ruled out, one could concentrate on physics behind that strange behaviour. Now we are left with measurements of a single sample at a single temperature 786 °C with neighbours as much as 200 °C afar. The measurement with the original sample is unrepeatable, because in the course of being heated up to 1100 °C, the sample was completely annealed and lost its original material structure. Our experience with the rest of the dataset prepared by the authors who are specialists in this kind of measurements makes the probability of a huge error quite low and the matter is thus worth discussing it further.

The chemical and crystalline composition, although not stated, is roughly the same as in Etna 1992 base sample. The latter does not show any exceptional behaviour at 781 °C (Fig. 2). Thus, a sudden crystal phase change cannot be blamed for the inconsistency. The authors of the original study identified the mechanism of crack healing as a possible cause of quality factor and shear modulus increase during the annealing. Due to the more intensive cooling of the surface of the lava flow, the Etna 1992 top sample exhibited more thermally-induced microcracking than Etna 1992 base. It is possible

that at 786 °C, the measurements are covering a non-equilibrium state in the middle of the crack healing process: the transformation of cracks into elliptical/spherical pores already decreased the loss angle, but the migration of volatiles out of the material and the decrease of the pore volume leading to shear factor increase is still in progress or waiting for higher temperatures. The high frequency torsions might propel the migration of volatiles more intensively than the low frequencies. Such extra stiffening with increasing frequency can add to the classical linear stiffening effect and increase $h_{|G^*|}(\Theta)$.

An alternative explanation is that even in an equilibrium multicomponent/multiphase system, especially at the possible onset of an additional relaxation mechanism (diffusion creep), one component can prevailingly influence the loss factor, the other the magnitude of the shear modulus. There can also be complicated nonlinear interactions between the components.

6. Conclusions

The main achievements of our current work are:

a) The introduction of $|G^*(\omega)|$-borne and $\varphi(\omega)$-borne relaxation time spectra, $h_{|G^*|}(\Theta)$ and $h_\varphi(\Theta)$, makes a totally separate treatment of the original $|G^*(\omega)|$, $\varphi(\omega)$ datastreams possible. The naturally unscaled spectra $h_{|G^*|}(\Theta)$, $h_\varphi(\Theta)$ are very well suited for comparing the attenuation of materials with very different scales of viscoelastic moduli. As an alternative to $h_{|G^*|}(\Theta)/h_\varphi(\Theta)$, the ratio $H'(\Theta)/H''(\Theta)$ can be used as viscoelastic consistency indicator and yields very similar results. The only serious methodological disadvantage of the latter approach is the mixing of the original $|G^*(\omega)|$, $\varphi(\omega)$ frequency responses and their errors.

b) Our method of iterative inversion of the frequency responses to relaxation time spectra is very stable, provided that the FRs are suitably prefiltered. The quality of the inversion can be checked by the calculation of the relaxed or unrelaxed shear modulus G_R, G_U. Ideally, they should be independent of Ω.

c) With temperature increase from 500 °C to 1100 °C, the viscoelastic consistency of all examined lava samples improves to the ideal linear viscoelasticity. Nevertheless, each sample has a specific fingerprint. In the

Etna 1992 samples, there is a not very convincing evidence for fairly good consistency at $\sim 500\,^{\circ}\mathrm{C}$, then there is a loss of consistency between $\sim 600\,^{\circ}\mathrm{C}$ and $\sim 800\,^{\circ}\mathrm{C}$, especially dramatic in Etna 1992 top sample at $786\,^{\circ}\mathrm{C}$, where $h_{|G^*|}(\Theta)/h_{\varphi}(\Theta)$ approaches 20. This inconsistency level remains a mystery and a very strong motivation for a further search for extreme inconsistencies. If zones with that high inconsistency really occur within the lithosphere, then there could be a chance to detect them by seismic tomography.

Acknowledgements. The experimental viscoelastic data was made available to us by the courtesy of Dr. Michael James from Lancaster Environment Centre at the Lancaster University, UK. The symbolical and numerical computations were performed and figures plotted in the computational environment Mathematica® 9 by Wolfram Research, Inc. The figures were finalised in the cartographic vector drawing software OCAD® 12 by OCAD AG. The authors are grateful to the Slovak grant agency VEGA (grant No. 01/0462/16) for the partial support of this work.

References

Bagdassarov N. S., Dingwell D. B., 1993: Frequency dependent rheology of vesicular rhyolite. J. Geophys. Res., **98**, B4, 6477–6487, doi: 10.1029/92JB02690.

Bagdassarov N. S., 2000: Anelastic and viscoelastic behaviour of partially molten rocks and lavas. In: Bagdassarov N. S., Laporte D., Thompson A. (Eds.): Physics and chemistry of partially molten rocks. Kluwer, Dordrecht, pp. 29–66, doi: 10.1007/978-94-011-4016-4_2.

Belkin H. E., Kilburn C. R. J., De Vivo B., 1993: Sampling and major element chemistry of the recent (A.D. 1631–1944) Vesuvius activity. J. Volcanol. Geotherm. Res., **58**, 1-4, 273–290, doi: 10.1016/0377-0273(93)90113-6.

Bode H. W., 1945: Network Analysis and Feedback Amplifier Design. D. Van Nostrand, New York, 1945.

Calvari S., Pinkerton H., 2002: Instabilities in the summit region of Mount Etna during the 1999 eruption. Bull. Volcanol., **63**, 8, 526–535, doi: 10.1007/s004450100171.

Chien S.-Y., 2014: Rheological and Seismic Properties of Solid-Melt Systems: A Mechanical Spectroscopy Study. Springer Theses, doi: 10.1007/978-3-319-03098-2.

Ferry J. D., 1980: Viscoelastic Properties of Polymers, 3rd ed. John Wiley & Sons: New York.

Fontaine F. R., Ildefonse B., Bagdassarov N., 2005: Temperature dependence of shear wave attenuation in partially molten gabbronorite at seismic frequencies. Geophys. J. Int., **163**, 3, 1025–1038, doi: 10.1111/j.1365-246X.2005.02767.x.

Fontaine F. R., Ildefonse B., Neuville D. R., Mainprice D., 2008: Influence of viscosity variation of basaltic and andesitic melts on seismic attenuation in partially molten gabbronorite. Phys. Earth Planet. Inter., **167**, 3-4, 223–229, doi: 10.1016/j.pepi.2008.04.010.

Garcia M. O., Rhodes J. M., Ho R., Ulrich G., Wolfe E., 1992: Petrology of lavas from episodes 2-47 of the Puu OO eruption of Kilauea Volcano, Hawaii: evaluation of magmatic processes. Bull. Volcanol., **55**, 1-2. 1–16, doi: 10.1007/BF00301115.

James M. R., Bagdassarov N., Müller K., Pinkerton H., 2004: Viscoelastic behaviour of basaltic lavas. J. Volcanol. Geotherm. Res., **132**, 2-3, 99–113, doi: 10.1016/S0377-0273(03)00340-8.

Kramers H. A., 1927: The diffusion of light by atoms (La diffusion de la lumière par les atomes). Atti Cong. Intern. Fisica, (Transactions of Volta Centenary Congress) Como 2, 545–557 (in French).

Kronig R. d. L., 1926: On the theory of the dispersion of X-rays. J. Opt. Soc. Am., **12**, 6, 547–557, doi: 10.1364/JOSA.12.000547.

McCarthy C., Takei Y., Hiraga T., 2011: Experimental study of attenuation and dispersion over a broad frequency range: 2. The universal scaling of polycrystalline materials. J. Geophys. Res., **116**, B09207, doi: 10.1029/2011JB008384.

Okumura S., Nakamura M., Nakano T., Uesugi K., Tsuchiyama A., 2010: Shear deformation experiments on vesicular rhyolite: Implications for brittle fracturing, degassing, and compaction of magmas in volcanic conduits. J. Geophys. Res. Solid Earth, **115**, B6, doi: 10.1029/2009JB006904.

Okumura S., Kushnir A. R. L., Martel C., Champallier R., Thibault Q., Takeuchi S., 2016: Rheology of crystal-bearing natural magmas: Torsional deformation experiments at 800 °C and 100 MPa. J. Volcanol. Geotherm. Res., **328**, 237–246, doi: 10.1016/j.jvolgeores.2016.11.009.

Rocchi V., Sammonds P., Kilburn C. R. J., 2004: Fracturing of Etnean and Vesuvian rocks at high temperatures and low pressures. J. Volcanol. Geotherm. Res., **132**, 2-3, 137–157, doi: 10.1016/S0377-0273(03)00342-1.

Rusu C., Kuosmanen P., Astola J., 2005: Hilbert transform of discrete data: a brief review. In: Astola J., Egiazarian K., Saramäki T. (Eds.): Proceedings of The 2005 International TICSP Workshop on Spectral Methods and Multirate Signal Processing. SMMSP 2005, Riga, Latvia, 20–22 June 2005, pp. 79–84.

Takei Y., Fujisawa K., McCarthy C., 2011: Experimental study of attenuation and dispersion over a broad frequency range: 1. The apparatus. J. Geophys. Res., **116**, B09204, doi: 10.1029/2011JB008382.

Wagner N., 2004: Mechanical Spectroscopy on Volcanic Glasses. Dissertation (in German), FSU-Jena. Online, accessed 6 August 2018, available from: http://www.db-thueringen.de/servlets/DerivateServlet/Derivate-2594.

Winter H. H., 1997: Analysis of dynamic mechanical data: Inversion into a relaxation time spectrum and consistency check. J. Nonnewton. Fluid Mech., **68**, 2-3, 225–239, doi: 10.1016/S0377-0257(96)01512-1.

Appendix

Table 2. The frequency responses of the magnitude of shear modulus and the loss angle for the Etna 1992 top sample at 786 °C (*James et al., 2004*).

f [Hz]	$\|G^*\|$ [GPa]	loss angle [rad]
0.002	7.8984	0.029311
0.005	8.6888	0.02522
0.01	9.6538	0.023243
0.02	10.968	0.019216
0.05	11.665	0.016594
0.1	12.721	0.013335
0.2	15.352	0.0120599
0.5	17.345	0.01170799
1	18.169	0.0102132
2	19.268	0.0088959
5	20.627	0.0064447
10	21.312	0.0046908
20	21.669	0.0039605

sciendo

Contributions to Geophysics and Geodesy Vol. 49/2, 2019 (133–151)

A new method for complete quantitative interpretation of gravity data due to dipping faults

El-Sayed ABDELRAHMAN, Mohamed GOBASHY, Eid ABO-EZZ, Tarek EL-ARABY

Geophysics Department, Faculty of Science, Cairo University, Egypt;
e-mail: sayed5005@yahoo.com, bouguer3000@yahoo.com, aboezz2000@yahoo.com, tmelaraby@sci.cu.edu.eg

Abstract: We have developed a simple method to determine completely the model parameters of a buried dipping fault from gravity data (depths to the centers of the upper and lower portions of the faulted thin slab, dip angle, and amplitude coefficient). The method is based on defining the anomaly values at the origin and at four symmetrical points around the origin on the gravity anomaly profile. By defining these five pieces of information, the dip angle is determined for each value of the depth of the lower portion of the faulted thin slab by solving iteratively one nonlinear equation of the form $f(\alpha) = 0$. The computed dip angles are plotted against the values of the depth representing a continuous depth-dip curve. The solution for the depth to the lower portion of the faulted thin slab (down-thrown block) and the dip angle of the buried fault is read at the common intersection of the depth-dip curves. Knowing the depth to the center of the lower portion of the faulted layer and the dip angle, the problem of determining the depth to the center of the upper portion of the faulted slab (up-thrown block) is transformed into the problem of solving iteratively a nonlinear least-squares equation, $f(z) = 0$. Because the depths and the dip angle are known, the amplitude coefficient, which depends on the thickness and density contrast of the thin slab, is determined using a linear least-squares equation. The method is applied to theoretical data with and without random errors. The validity of the method is tested on real gravity data from Egypt. In all cases examined, the model parameters obtained are in good agreement with the actual ones and with those given in the published literature.

Key words: gravity interpretation, dipping faults, iterative methods, least squares method, depth-curves method, noise

1. Introduction

The dipping fault model is frequently used in gravity interpretation to find the depth and the dip angle of a class of faulted structures. Estimation

doi: 10.2478/congeo-2019-0007

of these parameters from gravity anomalies has drawn considerable attention. Fault interpretation using gravity modeling methods, e.g., 2D (*Tanner, 1967*), 2.5D (*Chakravarthi, 2011*), or 3D (*Cordell and Henderson, 1968*) involves personal judgments and requires density information as part of the input, along with depth and dip angle information obtained from geological and/or other geophysical data. Other methods use fixed simple geometry for interpreting gravity anomalies due to dipping faults (*Geldart et al., 1966; Paul et al., 1966; Green, 1976; Thompson, 1982; Gupta, 1983; Lines and Treitel, 1984; Abdelrahman et al., 1989; Gupta and Pokhriyal, 1990; Reid et al., 1990; Abdelrahman et al., 2003; Phillips et al., 2007; Utyupin and Mishenin, 2012*). The advantage of fixed geometry methods over continuous modeling methods is that they require neither density, dip angle, nor depth information, and they can be applied if little or no factual information other than the gravity data is available.

Very recently, *Abdelrahman et al. (2013), Essa (2013)* and *Abdelrahman and Essa (2015)* developed methods to determine only the depth to the upper portion of the faulted thin slab as well as the dip angle of the faulted structure from gravity data using numerical techniques. However, the drawback of these methods is that they assume that the throw of the fault is extremely large, i.e., the depth to the lower portion of the thin slab approaches infinity. This assumption will lead definitely to large errors in estimating the model parameters of the faulted structure from real gravity data.

In this paper, we have developed a simple method to determine completely the model parameters of a buried dipping fault from the residual gravity anomaly. Using the anomaly values at the origin and four symmetrical points on the gravity anomaly profile, the problem of determining the depth to the center of the lower portion of the thin slab and the dip angle is transformed into the problem of solving one nonlinear equation to construct depth-dip angle curves. Knowing the depth and the dip angle computed from the constructed curves, the problem of determining the depth to the center of the upper portion of the faulted thin slab determination is transformed into the problem of solving iteratively a nonlinear least-squares equation, whereas the amplitude coefficient is determined using a simple linear least-squares equation. The accuracy of the result abstained by the procedures depends upon the accuracy to which the origin of the residual

anomaly profile can be determined from geological and/or other geophysical data. Also for this method to be valid, we assume that the thickness of the faulted layer is small compared to the depth of the up-thrown faulted block, i.e. the layer can be approximated by a thin sheet located at its center. The thin sheet approximation is valid and correct within 2% if the thickness is equal to or less than the depth. The method is applied to theoretical data with and without random errors. The validity of the method is tested on real gravity data from Egypt.

2. The method

The formula for the residual gravity anomaly generated along the profile normal to the strike of a 2-D dipping faulted thin slab having infinite strike length is given by the following equation (*Telford et al., 1976*):

$$g(x_i, z, h, \alpha) = K\left[\pi + \operatorname{atan}\left(\frac{x_i}{z} + \cot\alpha\right) - \operatorname{atan}\left(\frac{x_i}{h} + \cot\alpha\right)\right], \tag{1}$$

where z and h are the depths to the centers of the upper and the lower portions of the layer, respectively, α is the angle of dip measured counter-clockwise from surface, $K = 2\gamma\sigma t$, is the amplitude coefficient related to the thickness (t) and density contrast (σ) of the faulted slab, γ is the universal gravitational constant, and x_i is the horizontal coordinate position. The two-dimensional gravity dipping fault model is shown in Fig. 1.

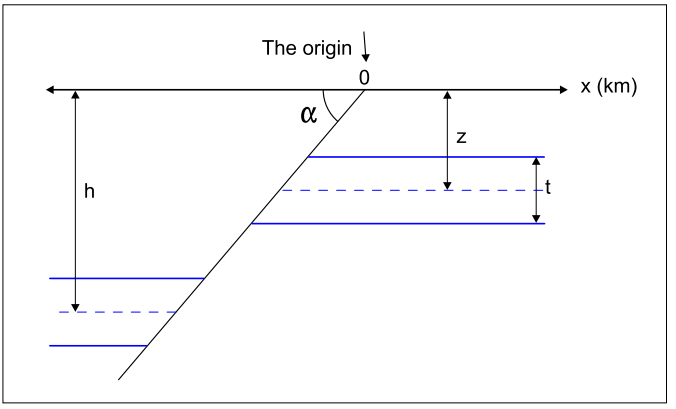

Fig. 1. Geometry of the dipping faulted thin slab model.

Equation (1) can be written as:

$$g(x_i, z, h, \alpha) = \frac{g(0)}{\pi}\left[\pi + \operatorname{atan}\left(\frac{x_i}{z} + \cot\alpha\right) - \operatorname{atan}\left(\frac{x_i}{h} + \cot\alpha\right)\right], \tag{2}$$

where $g(0) = K\pi$ is the anomaly value at the origin of the residual anomaly profile.

Equation (2) gives the following values at $x_i = \pm N$ and $\pm M$:

$$g(N) = \frac{g(0)}{\pi}\left[\pi + \operatorname{atan}\left(\frac{N}{z} + \cot\alpha\right) - \operatorname{atan}\left(\frac{N}{h} + \cot\alpha\right)\right], \tag{3}$$

$$g(-N) = \frac{g(0)}{\pi}\left[\pi + \operatorname{atan}\left(\frac{-N}{z} + \cot\alpha\right) - \operatorname{atan}\left(\frac{-N}{h} + \cot\alpha\right)\right], \tag{4}$$

$$g(M) = \frac{g(0)}{\pi}\left[\pi + \operatorname{atan}\left(\frac{M}{z} + \cot\alpha\right) - \operatorname{atan}\left(\frac{M}{h} + \cot\alpha\right)\right], \tag{5}$$

$$g(-M) = \frac{g(0)}{\pi}\left[\pi + \operatorname{atan}\left(\frac{-M}{z} + \cot\alpha\right) - \operatorname{atan}\left(\frac{-M}{h} + \cot\alpha\right)\right], \tag{6}$$

where $g(N)$, $g(-N)$, $g(M)$, and $g(-M)$ are the anomaly values at four symmetrical points around the origin.

Equations (3–6), can be simplified as:

$$\tan\left[\pi D(N) + \operatorname{atan}\left(\frac{N}{h} + \cot\alpha\right)\right] - \cot\alpha = \frac{N}{z}, \tag{7}$$

$$\tan\left[\pi D(-N) + \operatorname{atan}\left(\frac{-N}{h} + \cot\alpha\right)\right] - \cot\alpha = \frac{-N}{z}, \tag{8}$$

$$\tan\left[\pi D(M) + \operatorname{atan}\left(\frac{M}{h} + \cot\alpha\right)\right] - \cot\alpha = \frac{M}{z}, \tag{9}$$

$$\tan\left[\pi D(-M) + \operatorname{atan}\left(\frac{-M}{h} + \cot\alpha\right)\right] - \cot\alpha = \frac{-M}{z}, \tag{10}$$

where

$$D(N) = \frac{g(N)}{g(0)} - 1, \qquad D(-N) = \frac{g(-N)}{g(0)} - 1,$$

$$D(M) = \frac{g(M)}{g(0)} - 1\,, \qquad D(-M) = \frac{g(-M)}{g(0)} - 1\,.$$

Adding Eq. (7) to Eq. (8), and adding Eq. (9) to Eq. (10) will eliminate (z) and the following equations are obtained:

$$\tan\left[\pi D(N) + \operatorname{atan}\left(\frac{N}{h} + \cot\alpha\right)\right] + \\ + \tan\left[\pi D(-N) + \operatorname{atan}\left(\frac{-N}{h} + \cot\alpha\right)\right] = 2\cot\alpha\,, \tag{11}$$

and

$$\tan\left[\pi D(M) + \operatorname{atan}\left(\frac{M}{h} + \cot\alpha\right)\right] + \\ + \tan\left[\pi D(-M) + \operatorname{atan}\left(\frac{-M}{h} + \cot\alpha\right)\right] = 2\cot\alpha\,. \tag{12}$$

Using equations (11–12), we obtain after simple mathematical manipulation the following nonlinear equation in the dip angle (α) and the depth to the center of the lower portion of the faulted thin slab (h).

$$\alpha = \operatorname{datan}\left(\tan\left\langle \operatorname{atan}(T_1 + T_2 - T_3) - \pi D(-M)\right\rangle + \frac{M}{h}\right), \tag{13}$$

where

$$T_1 = \tan\left[\pi D(N) + \operatorname{atan}\left(\frac{N}{h} + \cot\alpha\right)\right],$$

$$T_2 = \tan\left[\pi D(-N) + \operatorname{atan}\left(\frac{-N}{h} + \cot\alpha\right)\right],$$

$$T_3 = \tan\left[\pi D(M) + \operatorname{atan}\left(\frac{M}{h} + \cot\alpha\right)\right].$$

The dip angle (α) can be obtained by solving Eq. (13) using a simple iteration method (*Press et al., 2007*) if h is known. The iterative form of equation (13) is given as:

$$\alpha_f = f(\alpha j)\,, \tag{14}$$

where (α_j) is the initial dip and (α_f) is the revised dip; (α_f) will be used

as the α_j for the next iteration. The iteration stops when $|\alpha_f - \alpha_j| \leq e$, where e is a small predetermined real number close to zero.

Thus, the dip angle of the faulted thin slab is determined by solving one non linear equation $f(\alpha) = 0$. Any initial guess for α works well because there is always one minimum, provided that (h) remains fixed in the process.

However, Eq. (13) can be used also not only to determine the dip angle (α) of the buried structure but also to simultaneously estimate the depth (h) to the center of the lower block of the faulted structure. The procedure is as follows:

1. Determine the origin of the observed gravity anomaly profile ($x_i = 0$) using geological and/or other geophysical data.
2. Digitize the observed gravity anomaly profile at several points with a suitable interval.
3. Eq. (13) is then applied to the input data yielding dip solutions α for all possible h values for fixed N and M values. The computed α values are plotted against h values representing a continuous depth-dip curve. The depth-dip curves should intersect at a single point, i.e., the value of α at the point of intersection is the dip angle of the faulted structure, and the value of h gives the depth to the center of the lower portion of the faulted thin slab. Theoretically, any two curves associated with two different values of N and M are just enough to simultaneously determine α and h. In practice, more than two values of N and M might be necessary because of the presence of noise in data.

Substituting the computed depth (h_c) and the computed dip angle (α_c) as fixed parameters in Eq. (2), we obtain:

$$g(x_i, z) = \frac{g(0)}{\pi} W(x_i, z)\,, \tag{15}$$

$$\text{where} \quad W(x_i, z) = \left[\pi + \operatorname{atan}\left(\frac{x_i}{z} + \cot\alpha_c\right) - \operatorname{atan}\left(\frac{x_i}{h_c} + \cot\alpha_c\right)\right].$$

Applying the least-squares method, the unknown z in Eq. (15) can be obtained by minimizing:

$$\varphi(z) = \sum_{i=1}^{P} \left[L(x_i) - \frac{g(0)}{\pi} W(x_i, z)\right]^2, \tag{16}$$

where $L(x_i)$ denoted the observed residual gravity anomaly at x_i.

Setting the derivative of $\phi(z)$ to zero with respect to z leads to:

$$f(z) = \sum_{i=1}^{P} \left[L(x_i) - \frac{g(0)}{\pi} W(x_i, z) \right] W^*(x_i, z) = 0, \qquad P = 1, 2, 3 \ldots, \tag{17}$$

where $W^*(x_i, z) = \dfrac{\mathrm{d}}{\mathrm{d}z} W(x_i, z)$.

Eq. (17) can be solved for z using the standard methods for solving non-linear equations. Here Eq. (17) is solved by a simple iteration method (*Press et al., 2007*). The iterative form of Eq. (17) is given as:

$$z_f = \left(\frac{\displaystyle\sum_{i=1}^{P} \left(\frac{x_i \, L(x_i)}{1 + \left(\frac{x_i}{z_j} + \cot \alpha_c \right)^2} \right)}{\displaystyle\sum_{i=1}^{P} \frac{g(0)}{\pi} \left[\frac{x_i \left(\pi + \operatorname{atan}\left(\frac{x_i}{z_j} + \cot \alpha_c \right) - \operatorname{atan}\left(\frac{x_i}{h_c} + \cot \alpha_c \right) \right)}{{z_j}^2 \left[1 + \left(\frac{x_i}{z_j} + \cot \alpha_c \right)^2 \right]} \right]} \right)^{1/2}, \tag{18}$$

where z_j is the initial depth parameter and z_f is the revised depth parameter; z_f will be use as the z_j for the next iteration. The iteration stops when $|z_f - z_j| \leq e$, where e is a small predetermined real number close to zero.

Thus, the depth to the center of the upper portion of the faulted thin slab is determined by solving one non linear equation $f(z) = 0$. Any initial guess for (z) works well because there is always one minimum, provided that (α_c) and (h_c) remain fixed in the process.

Substituting the depths (z_c) and (h_c) and the dip angle (α_c) in Eq. (1) as fixed parameters, we obtain:

$$g(x_i) = K \left[\pi + \operatorname{atan}\left(\frac{x_i}{z_c} + \cot \alpha_c \right) - \operatorname{atan}\left(\frac{x_i}{h_c} + \cot \alpha_c \right) \right]. \tag{19}$$

Finally, applying the least-squares method to Eq. (19), the unknown amplitude coefficient (K) can be determined from:

$$K_c = \frac{\displaystyle\sum_{i=1}^{P} L(x_i) \left[\pi + \operatorname{atan}\left(\frac{x_i}{z_c} + \cot \alpha_c \right) - \operatorname{atan}\left(\frac{x_i}{h_c} + \cot \alpha_c \right) \right]}{\displaystyle\sum_{i=1}^{P} \left[\pi + \operatorname{atan}\left(\frac{x_i}{z_c} + \cot \alpha_c \right) - \operatorname{atan}\left(\frac{x_i}{h_c} + \cot \alpha_c \right) \right]^2}. \tag{20}$$

In this way, the problem of determining the depth (h) and the dip angle (α) is transformed into the problem of constructing the depth-dip curves and the problem of depth (z) determination is transformed into the problem of solving a nonlinear least-squares equation, $f(z) = 0$, whereas the amplitude coefficient (K) is determined using a simple linear least-squares equation. Eqs. (13, 18, 20) are ready for determining the model parameters of a buried faulted structure from observed gravity data using a personal computer.

An interpretation scheme based on the above equations for analyzing field data is illustrated in Fig. 2.

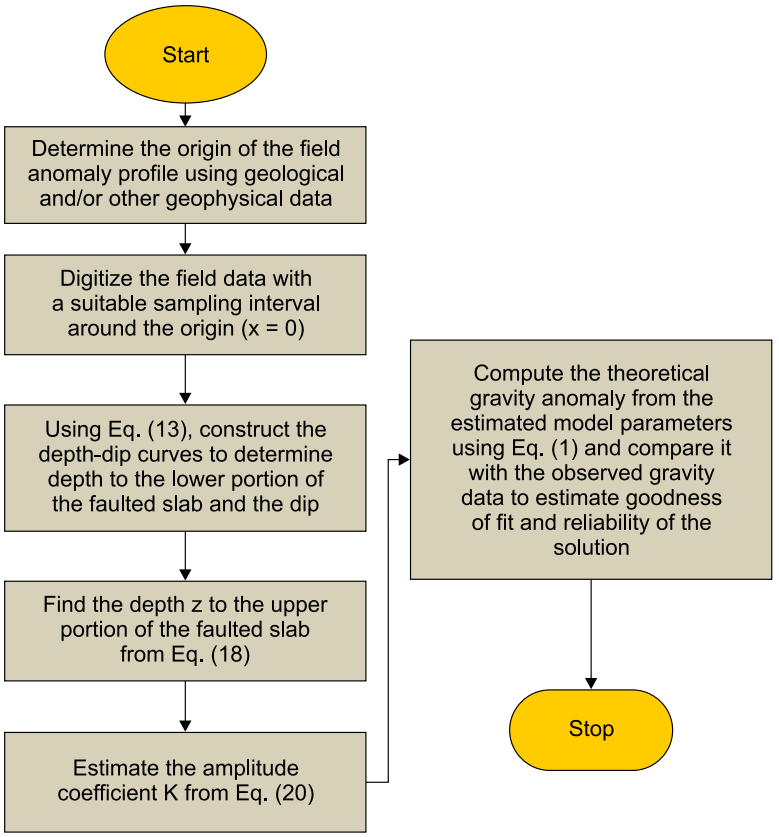

Fig. 2. Generalized scheme for depths, dip angle, and amplitude coefficient determination.

3. Theoretical examples:

3.1. Error response of the method

Fig. 3 shows a synthetic gravity anomaly due to a dipping fault (K = 100 mGal, z = 8 km, h = 12 km, α = 75°, profile length = 40 km, and sample interval = 1 km). The synthetic gravity anomaly was interpreted using our method (Eqs. (13, 18, 20)) to determine, respectively, the depth to the center of the lower portion, the dip angle, the depth to the center of the upper portion, and the amplitude coefficient of the faulted structure. Fig. 4 shows the intersection of the depth-dip curves at the correct location h = 12 km and α = 75°. The computed depth to the center of the upper portion and the amplitude coefficient determined from Eqs. (18, 20) were, respectively, z = 8 km, and K = 100 mGal. Perfect results are obtained when using synthetic noise-free data.

Moreover, the synthetic gravity anomaly was contaminated with 5% random Gaussian error using the following equation:

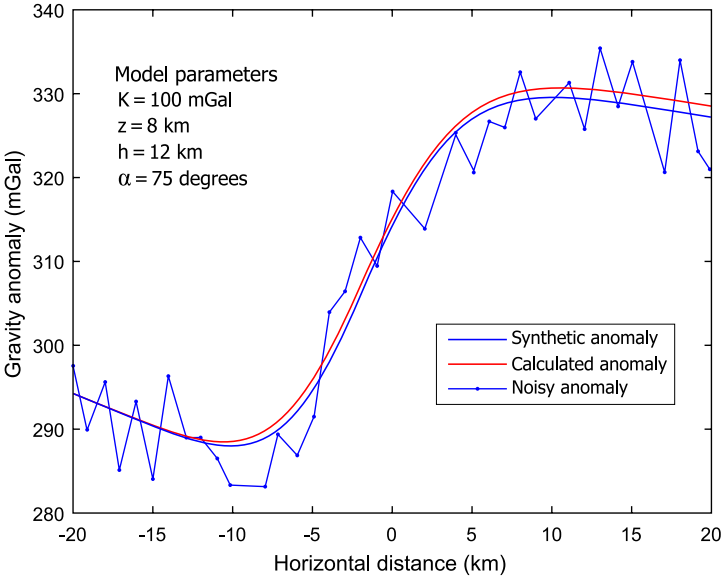

Fig. 3. A synthetic gravity anomaly with and without random errors of a buried dipping fault thin slab. The model parameters are: K = 100 mGal, z = 8 km, h = 12 km, and α = 75°. The computed gravity anomaly using the estimated model parameters from noisy data is also illustrated.

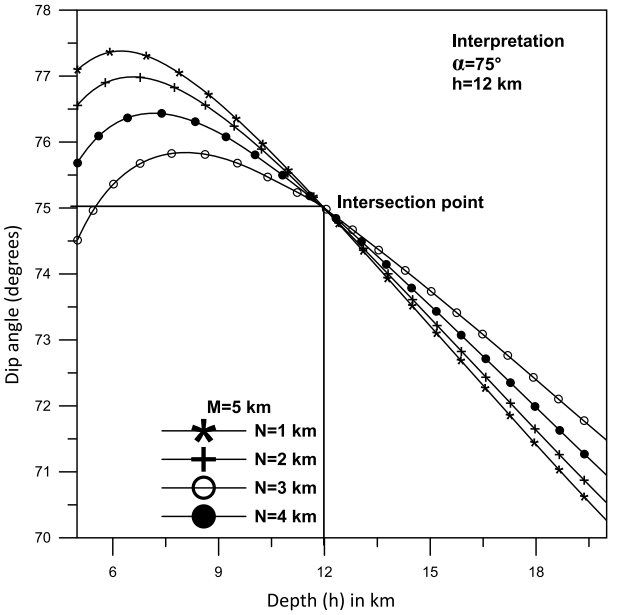

Fig. 4. Interpretation of the data in Fig. 3 using the depth-dip curves method.

$$\Delta g_{rnd1}(x_i) = \Delta g_1(x_i)\,[1 + (\mathrm{RND}(i) - 0.5) * 0.05]\,, \tag{21}$$

where $\Delta \mathrm{g}_{rnd1}(x_i)$ is the contaminated anomaly value at x_i and $\mathrm{RND}(i)$ is a pseudo-random number whose range is (0, 1). The interval of the pseudo random number is an open interval, i.e. it does not include the extremes values 0 and 1.

The depth-dip curves method (Eq. 13) was then applied to the noisy gravity anomaly (Fig. 3). The results are plotted in Fig. 5. In this case, the depth-dip curves intersect each other at $h = 12.5\,\mathrm{km}$ and $\alpha = 74.8°$. Using these values, Eqs. (18, 20) were then used to estimate the depth to the center of the upper portion and the amplitude coefficient of the fault. The result is: $z = 8.3\,\mathrm{km}$ and $K = 100.3\,\mathrm{mGal}$. The calculated gravity anomaly using the estimated model parameters is shown also in Fig. 3. This figure shows the numerical fitting between the noisy and the calculated synthetic anomaly values. The best fit is considered as a good criterion for accepting the solution in this example and noisy field conditions. The solution for all the model parameters is in good agreement with the actual model parameters.

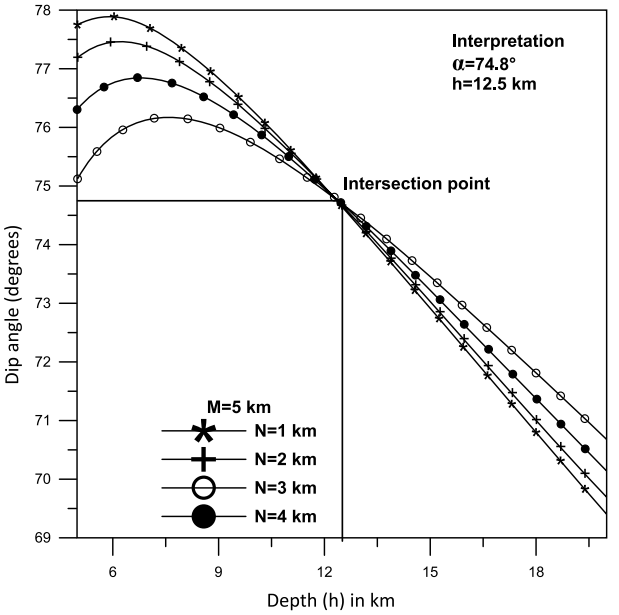

Fig. 5. Interpretation of the data in Fig. 3 after adding 5% random errors using the present depth-dip curves method.

This demonstrates that our method will give reliable results when applied to noisy gravity data as well.

3.2. Effect of wrong origin

Uncertain knowledge of the origin may lead to error in the model parameters (z, h, α, K) when interpreting real data. In this subsection we investigate this effect. The origin of the dipping faulted thin slab was assumed to be chosen incorrectly by introducing errors (offset) of ± 500 m in the horizontal coordinate x_i using synthetic data ($K = 100$ mGal, $z = 8$ km, $h = 12$ km, $\alpha = 75°$, profile length $= 40$ km, and sample interval $= 1$ km). Following the same interpretation method, the results are shown in Fig. 6 and Table 1.

It was verified numerically that Eqs. (13, 18, 20) give an acceptable error of 7.5% in the model parameters. Fig. 7 shows the gravity anomaly profiles computed using the estimated model parameters (Table 1) compared with the synthetic gravity anomaly. In spite of the error in the calculated model

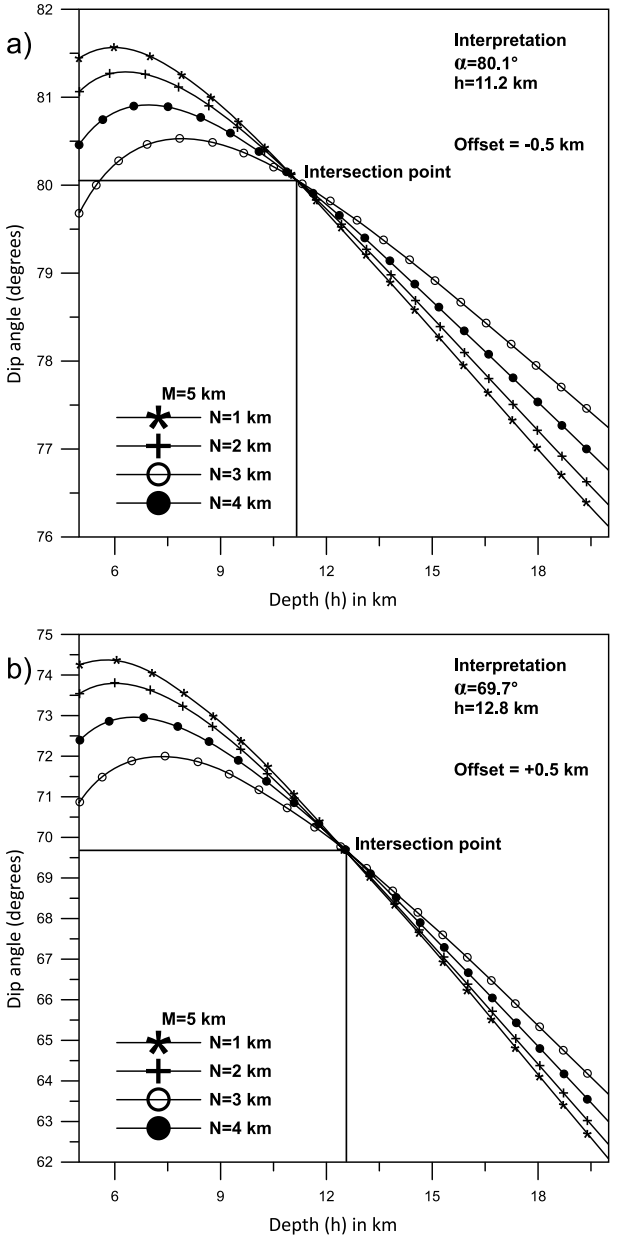

Fig. 6. Data interpretation of Fig. 3 in which offset of ± 0.5 km is introduced into the horizontal position x_i.

Table 1. Numerical results obtained from synthetic example ($K = 100$ mGal, $z = 8$ km, $h = 12$ km, $\alpha = 75°$, and profile length = 40 km) after adding ±500 m errors into the horizontal coordinate x_i.

Parameters	**Offset = −500 m**		**Offset = +500 m**	
	Computed values	% of error	Computed values	% of error
Depth z (km)	7.4	−7.5	8.61	7.6
Depth h (km)	11.2	−6.7	12.8	6.7
Dip angle α (degrees)	80.1	6.8	69.7	−7.1
Amplitude coefficient K (mGal)	99.5	0.5	100.5	0.5

parameters, the overall fitting between the computed and actual gravity anomalies in case the offset is ±500 m is clear. On the other hand when using larger offset values, the method may result in an instable interpretation curves. However, since the interpretation requires only a relatively short

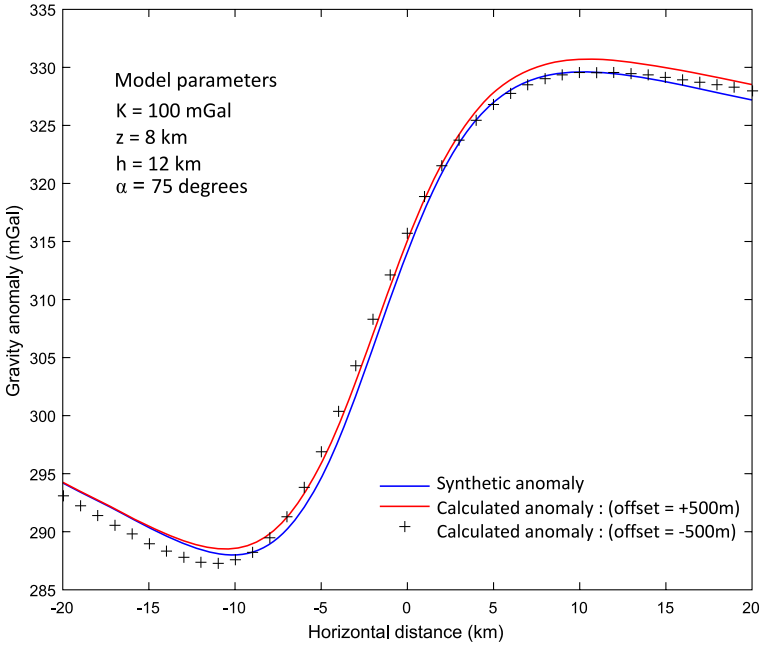

Fig. 7. Synthetic and calculated gravity anomalies using the estimated model parameters after introducing offset of ±500 m.

profile length, the problem may be solved effectively and economically by increasing the number of measurements made within the restricted length of the profile. At the same time, using a relatively short length of profile, results in a very high rejection of neighboring disturbances. Generally, the accuracy of the result obtained by the present method depends upon the accuracy of which the origin of the fault is determined from geological and/or other geophysical.

3.3. Effect of using different observation points $N's$ and $M's$

In the above examples, we have used a fixed M value and different N values to construct the depth-dip curves. In this subsection, we test a large range of $N's$ and $M's$ to investigate whether or not our method would give consistent results.

The synthetic gravity anomaly due to a dipping fault ($K = 100$ mGal, $z = 8$ km, $h = 12$ km, $\alpha = 75°$, profile length $= 40$ km, and sample interval $= 1$ km) shown previously in Fig. 3 was interpreted using the present depth-dip curves method using a large range of $N's$ and $M's$. The results are shown in Fig. 8. It is verified that the depth-dip curves intersect at the correct solution $h = 12$ km and $\alpha = 75°$. The depth-dip curves shown in Fig. 8 are similar to the depth-dip curves shown in Fig. 4 but they are not identical because of using different N and M values. This demonstrates that our method will give consistent results when using a large range of $N's$ and $M's$.

4. Field example

A Bouguer gravity anomaly profile over the Gazal fault, south Aswan, Egypt is interpreted to determine the model parameters (z, h, α, K). The Bouguer anomaly profile over Gazal fault is shown in Fig. 9. The fault affected both the basement and sedimentary rocks and crops out at the surface (*Abdelrahman et al., 1999*). The depth to the basement is found to be about 200 m as obtained from drilling information (*Evans et al., 1991*). In this example, the fault trace point is determined on the gravity profile, as usual, by projecting the point of intersection between the fault and the

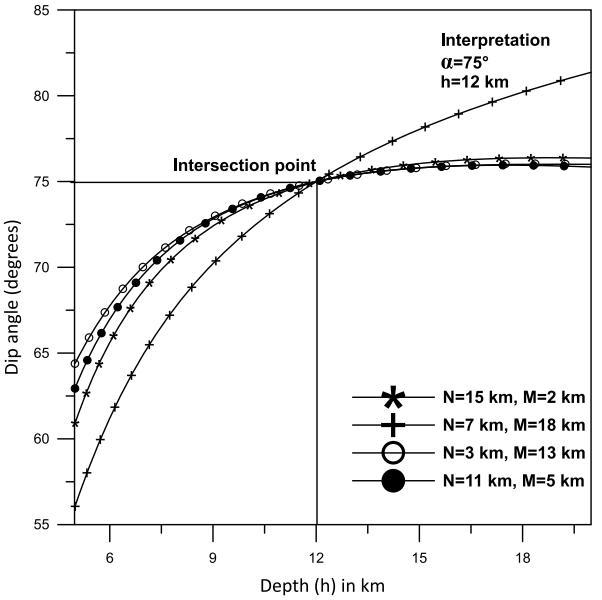

Fig. 8. Interpretation of the data in Fig. 3 using the depth-dip curves method applying a large range of $N's$ and $M's$ values.

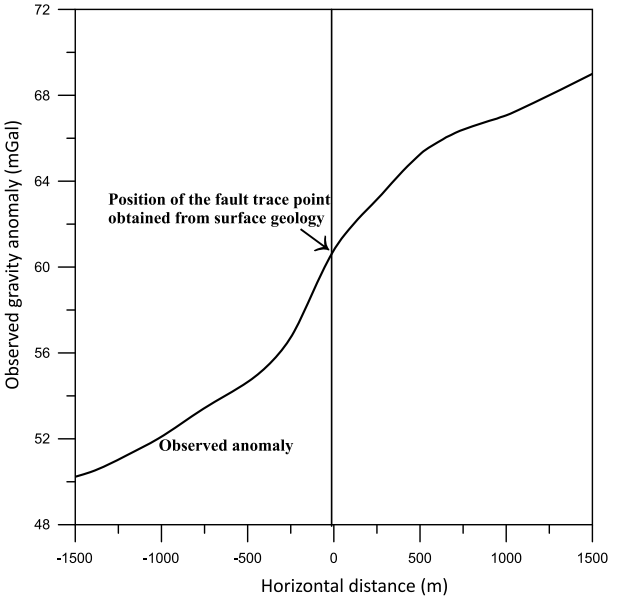

Fig. 9. Gazal Fault gravity anomaly, south Aswan, Egypt.

ground surface vertically. The gravity profile has been digitized at an interval of 62.5 m. Eq. (13) is applied to the gravity anomaly profile using five combinations of N and M points to construct the depth-dip curves (Fig. 10). This figure shows that the curves can be interpreted to intersect at $h = 315$ m and $\alpha = 65°$. Eqs. (18, 20) are used then to determine the depth to the center of the upper portion of the fault slab and the amplitude coefficient. The complete interpretation is: $z = 162$ m, $h = 315$ m, $\alpha = 65°$, and $K = 19.4$ mGal. This suggests that Gazal fault resembles a dipping fault ($\alpha = 65°$) where the center of the upper portion of the faulted slab is buried at a depth of 162 m and the center of the lower portion of the faulted slab is located at a depth of 315 m. The depth to the center to the upper portion of the faulted bed and the dip angle obtained by the present method generally agrees well with those obtained from drilling information and by *Abdelrahman et al. (2013), Essa (2013)* and *Abdelrahman and Essa (2015)* as summarized in Table 2. However, the amplitude coefficient obtained by

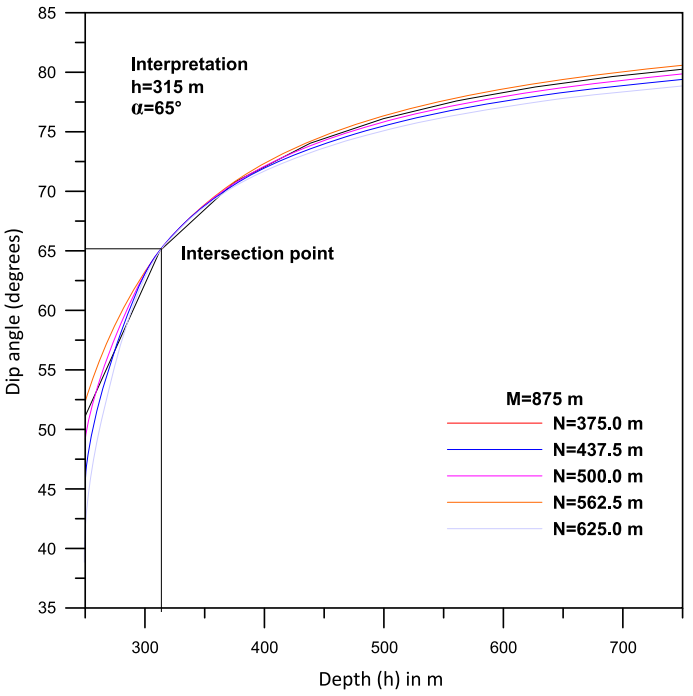

Fig. 10. Data interpretation of Fig. 9 using the depth-dip curves method.

Table 2. Comparative results of the Gazal field example.

Parameters	Abdelrahman et al. method (2013)	Essa method (2013)	Abdelrahman and Essa method (2015)	**present method**
Depth z (m)	173	208	202	162
Depth h (m)	–	–	–	315
Dip angle α (Degrees)	62.5	40	58	65
Amplitude coefficient K (mGal)	–	–	2.4	19.42

the present method is extremely larger than that obtained by *Abdelrahman and Essa (2015)*. This is because of the fact that the gravity anomaly over Gazal fault consists of a residual component due to Gazal fault and a regional component represented by a first order polynomial (*Abdelrahman and Essa, 2015*). It is evident from this field example that our method gives a complete insight from gravity data concerning the nature of Gazal fault structure.

5. Conclusions

The problem of determining the depths to the center of the upper and lower portions, dip angle, and amplitude coefficient of a buried dipping faulted thin slab from observed gravity data can be solved using the present method. The present approach is capable of determining completely the model parameters of the buried structure from the gravity data given in a small area over the buried structure, i.e., from the small segment of the gravity profile above the origin. The depths, dip angle, and the amplitude coefficient obtained by present method might be used to gain a complete geologic insight concerning the subsurface. The advantages of the present method over previous graphical and numerical techniques used to interpret gravity data due to dipping faults are: 1) all the four model parameters can be obtained, and 2) the method gives good results when the gravity anomaly is contaminated with Gaussian random noise.

Finally, we envisage the newly introduced method will result in the future development of new methods to interpret completely gravity gradient data due to dipping faults.

Acknowledgements. The authors would like to thank the editors and the capable anonymous reviewer for their excellent suggestions and thorough review that improved our original manuscript. The authors would like also to thank Prof. Afif Saad (previous Associate Editor of Potential Field Methods, GEOPHYSICS) for reviewing critically and editing the manuscript.

References

Abdelrahman E. M., Essa K., Abo-Ezz, E. R., 2013: A least-squares window curves method to interpret gravity data due to dipping faults. J. Geophys. Eng., **10**, 2, 025003, doi: 10.1088/1742-2132/10/2/025003.

Abdelrahman E. M., Essa K. S., 2015: Three least-squares minimization Approaches to interpret gravity data due to dipping faults. Pure Appl. Geophys., **172**, 2, 427–438, doi: 10.1007/s00024-014-0861-4.

Abdelrahman E. M., Bayoumi A. I., El-Araby H. M., 1989: Dip angle determination of fault planes from gravity data. Pure Appl. Geophys., **130**, 4, 735–742, doi: 10.1007/BF00881608.

Abdelrahman E. M., El-Araby H. M., El-Araby T. M., Abo-Ezz E. R., 2003: A least-squares derivatives analysis of gravity anomalies due to faulted thin slabs. Geophysics, **68**, 2, 535–543, doi: 10.1190/1.1567222.

Abdelrahman E. M., Radwan A. H., Issawy E. A., Al-Araby H. M., Al-Araby T. M., Abo-Ezz E. R. 1999: Gravity interpretation of vertical faults using correlation factors between successive least-squares residual anomalies. The Mining Pribram Symp. on Mathematical Methods in Geology, MC2-1–6.

Chakravarthi V., 2011: Automatic gravity optimization of 2.5D strike listric fault sources with analytically defined fault planes and depth-dependent density. Geophysics, **76**, 2, I21–I31, doi: 10.1190/1.3541957.

Cordell L., Henderson R. G., 1968: Iterative three-dimensional solution of gravity anomaly data using a digital computer. Geophysics, **33**, 4, 596–601, doi: 10.1190/1.1439955.

Essa K. S., 2013: Gravity interpretation of dipping faults using the variance analysis method. J. Geophys. Eng., **10**, 1, 015003, doi: 10.1088/1742-2132/10/1/015003.

Evans K., Beavan J., Simpson D., 1991: Estimating aquifer parameters from analysis of forced fluctuations in well level: An example from the Nubian Formation near Aswan, Egypt: 1. Hydrogeological background and large-scale permeability estimates. J. Geophys. Res., **96**, B7, 12127–12137, doi: 10.1029/91JB00955.

Geldart L. P., Gill D. E., Sharma B., 1966: Gravity anomalies of two dimensional faults. Geophysics, **31**, 2, 372–397, doi: 10.1190/1.1439781.

Green R., 1976: Accurate determination of the dip angle of a geological contact using the gravity method. Geophys. Prospect., **24**, 2, 265–272, doi: 10.1111/j.1365-2478.1976.tb00924.x.

Gupta O. P., 1983: A least-squares approach to depth determination from gravity data. Geophysics, **48**, 3, 357–360, doi: 10.1190/1.1441473.

Gupta O. P., Pokhriyal S. K., 1990: New formula for determining the dip angle of a fault from gravity data. SEG Expanded Abstract, **9**, 646–649, doi: 10.1190/1.1890290.

Lines L. R., Treitel S., 1984: A review of least-squares inversion and its application to geophysical problems. Geophys. Prospect., **32**, 3, 159–186, doi: 10.1111/j.1365-2478.1984.tb00726.x.

Paul M. K., Datta S., Banerjee B., 1966: Direct interpretation of two dimensional Structural fault from gravity data. Geophysics, **31**, 5, 940–948, doi: 10.1190/1.1439825.

Phillips J. D., Hansen R. O., Blakely R. J., 2007: The use of curvature in potential-field interpretation. Exploration Geophysics, **38**, 2, 111–119, doi: 10.1071/EG07014.

Press W. H., Teukolsky S. A., Vetterling W. T., Flannery B. P., 2007: Numerical Recipes, The Art of Scientific Computing, Third edition, Cambridge University Press, Cambridge, 1235 p.

Reid A. B., Allsop J. M., Granser H., Millett A. J., Somerton I. W., 1990: Magnetic interpretation in the three dimensions using Euler deconvolution. Geophysics, **55**, 1, 80–91, doi: 10.1190/1.1442774.

Tanner J. G., 1967: An automated method of gravity interpretation. Geophys. J. Roy. Astr. Soc., **13**, 339–347, 1-3, doi: 10.1111/j.1365-246X.1967.tb02164.x.

Telford W. M., Geldart L. P., Sheriff R. E., Key D. A., 1976: Applied geophysics. Cambridge University Press, London, 860 p.

Thompson D. T., 1982: EULDPTH: A new technique for making computer-depth estimates from magnetic data. Geophysics, **47**, 1, 31–37, doi: 10.1190/1.1441278.

Utyupin Yu. U., Mishenin S. G., 2012: Locating the sources of potential fields in aerial data using the singularity method. Russ. Geol. Geophys., **53**, 10, 1111–1116, doi: 10.1016/j.rgg.2012.08.011.

sciendo

Contributions to Geophysics and Geodesy Vol. 49/2, 2019 (153–180)

Marquardt inverse modeling of the residual gravity anomalies due to simple geometric structures: A case study of chromite deposit

Ata ESHAGHZADEH[1,*], Alireza DEHGHANPOUR[2], Sanaz SEYEDI SAHEBARI[3]

[1] Graduate student of geophysics, Institute of Geophysics, University of Tehran, Iran
e-mail: eshagh@alumni.ut.ac.ir, tel: +98 936 0161579

[2] Graduate student of geophysics, Islamic Azad University, Science and Research Branch, Tehran, Iran; e-mail: a.r.dehghanpour@gmail.com, tel: +98 9173054665

[3] Instructor, Roshdiyeh Higher Education Institute, Tabriz, Iran
e-mail: seyedi.sahebari@yahoo.com, +98 9141107646

Abstract: In this paper, an inversion method based on the Marquardt's algorithm is presented to invert the gravity anomaly of the simple geometric shapes. The inversion outputs are the depth and radius parameters. We investigate three different shapes, i.e. the sphere, infinite horizontal cylinder and semi-infinite vertical cylinder for modeling. The proposed method is used for analyzing the gravity anomalies from assumed models with different initial parameters in all cases as the synthetic data are without noise and also corrupted with noise to evaluate the ability of the procedure. We also employ this approach for modeling the gravity anomaly due to a chromite deposit mass, situated east of Sabzevar, Iran. The lowest error between the theoretical anomaly and computed anomaly from inverted parameters, determine the shape of the causative mass. The inversion using different initial models for the theoretical gravity and also for real gravity data yields approximately consistent solutions. According to the interpreted parameters, the best shape that can imagine for the gravity anomaly source is the vertical cylinder with a depth to top of 7.4 m and a radius of 11.7 m.

Key words: chromite deposit, gravity anomaly, Marquardt's algorithm, simple geometric shapes

1. Introduction

Non-uniqueness is a feature in the inverse modeling of the residual gravity anomaly as can assign a set of the measured gravity field data on the

*corresponding author

doi: 10.2478/congeo-2019-0008

ground to the geometrical distributions of the subsurface mass with various shapes or physical parameters such as density and depth. One way to eliminate this ambiguity is to put a suitable geometry to the anomalous body with a known density followed by inversion of gravity anomalies (*Chakravarthi and Sundararajan, 2004*). Although simple models may not be geologically realistic, they are usually are sufficient to analyze sources of many isolated anomalies (*Abdelrahman and El-Araby, 1993b*). The interpretation of such an anomaly aims essentially to estimate the parameters such as shape, depth, and radius of the gravity anomaly causative body such as geological structures, mineral mass and artificial underground structures.

Several graphical and numerical methods have been developed for analyzing residual gravity anomalies caused by simple bodies, such as *Saxov and Nygaard (1953)* and *Bowin et al. (1986)*. The methods include, for example, Fourier transform (*Odegard and Berg, 1965; Sharma and Geldart, 1968*); Mellin transform (*Mohan et al., 1986*); Walsh transforms techniques (*Shaw and Agarwal, 1990*); ratio techniques (*Hammer, 1977; Abdelrahman et al.,1989*); least-squares minimization approaches (*Gupta, 1983; Lines and Treitel, 1984; McCowan and Abdelrahman, 1990; Abdelrahman et al., 1991*) and different neural networks (*Salem et al., 2001; Osman et al., 2006, 2007; Al-Garni, 2013; Eshaghzadeh and Kalantari, 2015; Eshaghzadeh and Hajian, 2018*); effective quantitative interpretations using the least-squares method (*Gupta, 1983*) based on the analytical expression of simple moving average residual gravity anomalies are yet to be developed. *Abdelrahman and El-Araby (1993a)* introduced an interpretive technique based on fitting simple models convolved with the same moving average filter as applied to the measured gravity. A simple method proposed by *Essa (2007)* is used to determine the depth and shape factor of simple shapes from residual gravity anomalies along the profile. Another automatic method, the least-squares method, was proposed by *Asfahani and Tlas (2008)*, by which the depth and amplitude coefficient can be determined.

In this paper, a simultaneous non-linear inversion based on Marquardt optimization is developed to estimate the radius and depth parameters of the simple structures such as sphere, infinite horizontal cylinder and semi-infinite vertical cylinder. The Marquardt inversion method has been used for modeling the geological structures such as faulted beds (*Chakravarthi and Sundararajan, 2005*), anticlinal and synclinal structures (*Chakravarthi*

and Sundararajan, 2007, 2008), multiple prismatic structures (*Chakravarthi and Sundararajan, 2006*). The validity of the method is tested on synthetic gravity data with and without random noise and also on a real gravity data set from Iran.

2. Gravity of simple geometry

In gravity, fields of many simple bodies are symmetric about the location of the source. For example, the general gravity g effect caused by simple models (such as a sphere, an infinite horizontal cylinder, and a semi-infinite vertical cylinder as shown in Fig. 1) at point $p(x_i, z)$ is given as (*Abdelrahman et al., 1989*):

$$g(x_i, z, q) = K \frac{z^m}{(x_i^2 + z^2)^q}\,, \tag{1}$$

where z is the depth, $m = 1$ for a sphere or a horizontal cylinder and $m = 0$ for a vertical cylinder, q,is a value (shape factor) characterizing the nature of the source ($q = 0.5$ for a vertical cylinder, $q = 1$ for a horizontal cylinder, and $q = 1.5$ for a sphere) and K is an amplitude factor related to the radius R and density contrast ρ of the source, as:

$$K = \begin{cases} (4/3)\pi G\,\rho R^3 & \text{for a sphere,} \\ 2\pi G\,\rho R^2 & \text{for a horizontal cylinder,} \\ \pi G\,\rho R^2 & \text{for a vertical cylinder,} \end{cases} \tag{2}$$

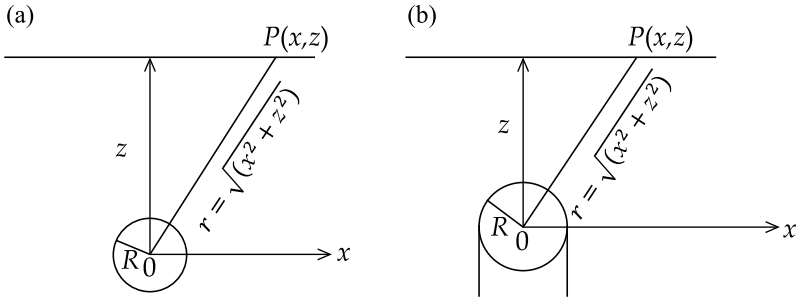

Fig. 1. (a) sphere and infinite horizontal cylinder models, (b) semi-infinite vertical cylinder model.

where G is the universal gravitational constant. For optimizing the gravity anomaly using Marquardt inversion, the gravity derivatives than the radius (radius derivative) and depth (vertical derivative) must be calculated. The radius and vertical derivative for the sphere model can be computed by equations 3 and 4, respectively, as:

$$\frac{\partial g}{\partial R} = 4\pi G\,\rho R^2 \left[\frac{z}{(x^2+z^2)^{3/2}}\right], \tag{3}$$

$$\frac{\partial g}{\partial z} = \frac{4}{3}\pi G\,\rho R^3 \left[\frac{x^2-2z^2}{(x^2+z^2)^{5/2}}\right], \tag{4}$$

corresponding expressions for the horizontal cylinder model can be written by:

$$\frac{\partial g}{\partial R} = 4\pi G\,\rho R \left[\frac{z}{(x^2+z^2)}\right], \tag{5}$$

$$\frac{\partial g}{\partial z} = 4\pi G\,\rho R^2 \left[\frac{x^2-z^2}{(x^2+z^2)^2}\right], \tag{6}$$

and for the vertical cylinder model the radius and vertical derivatives, respectively, give as following relationship:

$$\frac{\partial g}{\partial R} = 2\pi G\,\rho R \left[\frac{1}{(x^2+z^2)^{1/2}}\right], \tag{7}$$

$$\frac{\partial g}{\partial z} = -\pi G\,\rho R^2 \left[\frac{z}{(x^2+z^2)^{3/2}}\right]. \tag{8}$$

3. Methodology

The inversion of gravity anomalies is implicitly a mathematical process, trying to fit the computed gravity anomalies to the theoretical ones in the least-squares approach and then estimating the two parameters namely depth (z) and radius (R). The process of the inversion begins with computing the theoretical gravity anomaly of the simple geometry using equation (1).

The difference between the theoretical gravity $g_{obs}(x_i)$, and calculated gravity anomaly of an initial assumed model $g_{cal}(x_i)$, can be estimated by a misfit function, J (*Chakravarthi and Sundararajan, 2007*), as:

$$J = \sum_{i=1}^{N} \left[g_{obs}(x_i) - g_{cal}(x_i) \right]^2 , \tag{9}$$

N is the number of theoretical gravity data. We have employed the Marquardt's algorithm (*Marquardt, 1963*) given by *Chakravarthi and Sundararajan (2006)* for minimizing the misfit function until the normal equations can be solved for over all modifications of the two unknowns structural parameters (depth and radius), as:

$$\sum_{i=1}^{N} \sum_{k=1}^{2} \frac{\partial g(x_i)}{\partial a_j} \frac{\partial g(x_i)}{\partial a_k} (1 + \delta\lambda) \, \mathrm{d}a_k = \sum_{i=1}^{n} \left[g_{obs}(x_i) - g_{cal}(x_i) \right] \frac{\partial g(x_i)}{\partial a_j} , \quad \text{for } j = 1, 2 , \tag{10}$$

where $\mathrm{d}a_k$, $k = 1$ and 2 are the amendments to the two model parameters of the simple geometry structure, i.e. depth and radius. Partial derivatives required in the above system of equation (10) are calculated by the equations (3) to (8) according to the shape of the considered model. Also,

$$\delta = \begin{cases} 1 & \text{for } k = j, \\ 0 & \text{for } k \neq j, \end{cases}$$

and λ is the damping factor. The advancements, $\mathrm{d}a_k$, $k = 1$ and 2 evaluated from equation (10) are then added to or subtracted from the available parameters estimated from last iteration and the process repeats until the misfit, J, in equation (9) descends below a predetermined allowable error or the damping factor obtains a large value which is greater than allowable amount or the repetition continues until the end of the considered number for iterations (*Chakravarthi and Sundararajan, 2008*).

4. Theoretical examples

In this section, the performance of the foregoing method are investigated for the gravity anomalies of the three simple geometric models, i.e. sphere, infinite horizontal cylinder and semi-infinite vertical cylinder, with and without added random noise.

4.1. Sphere model

Fig. 2a shows the theoretical and calculated gravity field variations with 1 m interval along a 100 m profile due to an initial sphere model with the parameters $z = 25$ m and $R = 15$ m and an assumed sphere model with parameters $z = 30$ m and $R = 12$ m (Fig. 2b) where the maximum is the center of the profile. The density contrast is given as $\rho = 1000$ kg/m^3. Hence, the input initial parameters are $z = 30$ m and $R = 12$ m which with the theoretical gravity field are exerted to the inversion algorithm coded in Matlab. During inversion, ρ is constant and the model parameters, z and R are improved iteratively. The allowable values for error (misfit, J), iteration and damping factor (λ) are 0.00000001 mGal, 100 and 15, respectively. The initial damping factor is 0.5.

The misfit, J, reduces intensely from its initial value of 0.25 mGal at the first iteration to 0.0014 mGal at the end of the 5th iteration and then gradually reaches 0.000000034 mGal after the 9th iteration and its value at the 10th iteration becomes 0.00000000014 mGal which is smaller than the

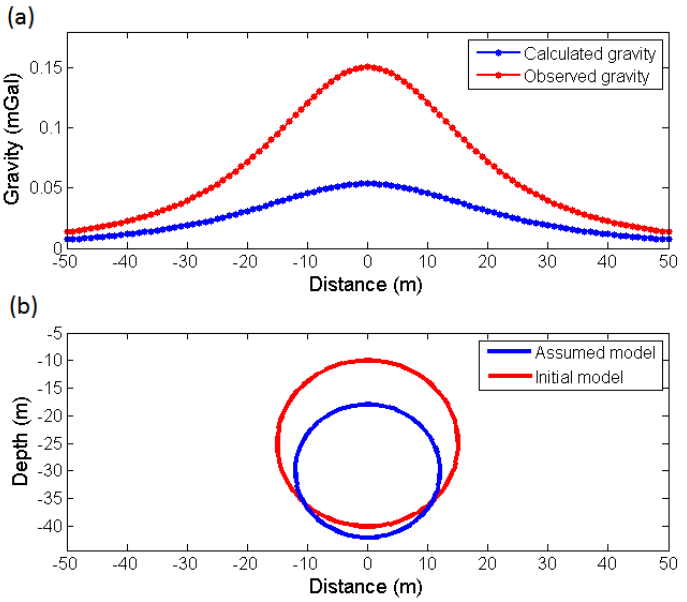

Fig. 2. (a) Theoretical and calculated gravity due to, (b) initial and assumed sphere models.

allowable error value (Fig. 3c). The iteration terminated at 10th echo and therefore the estimated parameters at 9th iteration are the final results of the inversion.

Fig. 3a and 3b illustrates the variations of the model parameters z and R during inversion with increasing the iteration number. The conclusive obtained parameters values are $z = 24.998$ m and $R = 15.001$. Fig. 4a shows the computed gravity anomaly from the inferred structure which is shown in Fig. 4b. The error value in the estimation of the model parameters, that is, depth and radius are 0.008 m and within 0.007 m, respectively.

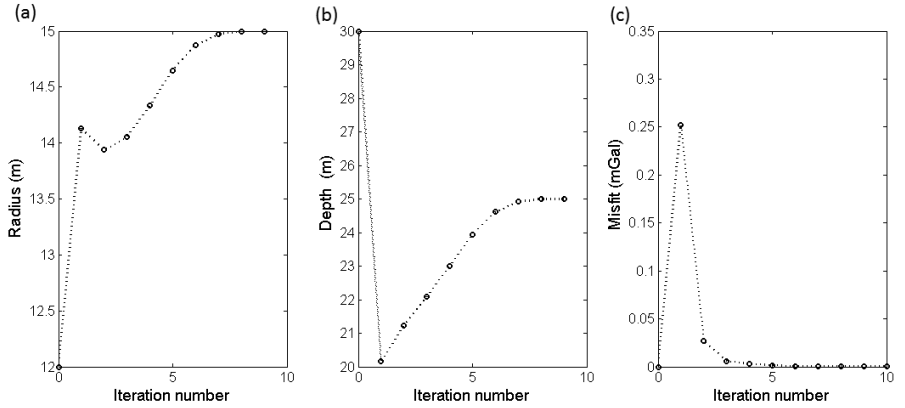

Fig. 3. Improvements of the structures parameters and misfit function versus iteration number for the assumed sphere model in Fig. 2.

The efficacy of error has been evaluated by adding 10% random noise to the gravity response of the initial sphere model (Fig. 5a) using the following expression:

$$g_{nois}(x_i) = g_{obs}(x_i)\left[(1 + RND(i) - 0.5) \times 0.1\right], \tag{11}$$

where $g_{nois}(x_i)$ is the noise corrupted synthetic data at x_i, and $RND(i)$ is a pseudorandom number whose range is between 0 to 1.

The initial values for the parameters of the assumed sphere model are given as $z = 22$ m and $R = 12.5$ m (Fig. 5b). The allowable values for error (misfit, J), iteration and damping factor (λ) are 0.00001 mGal, 100 and 15, respectively. The initial damping factor is 0.2. The misfit, J, reduces rapidly from its initial value of 0.061 mGal at the first iteration to 0.00088 mGal

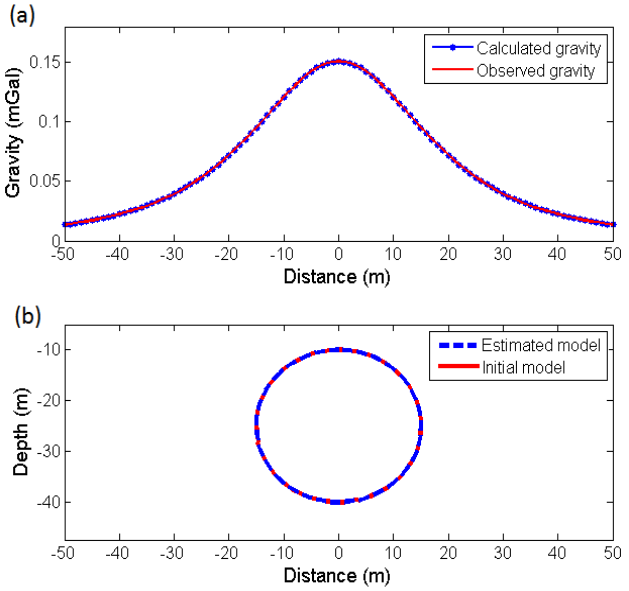

Fig. 4. (a) Theoretical and calculated gravity due to, (b) initial and estimated sphere models.

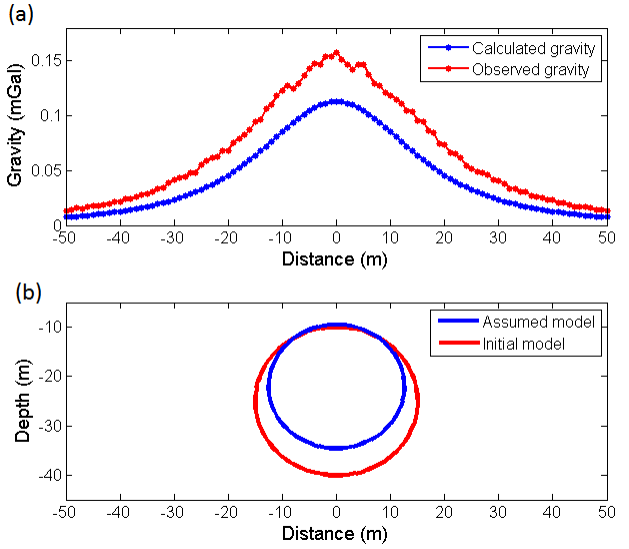

Fig. 5. (a) 10% noise corrupted theoretical gravity and calculated gravity due to, (b) initial and assumed sphere models.

at the end of the 6th iteration and then gradually reaches 0.000465 mGal after the 10th iteration and this value remained constant until the last iteration (Fig. 6c). After completing the iteration number, the damping factor, depth and radius attained 0.0000976, 24.97 m and 14.98 m values, respectively (Fig. 6a and 6b). The amount of error in the estimation of the model parameters, that is, depth and radius are 0.12 m and within 0.133 m, respectively.

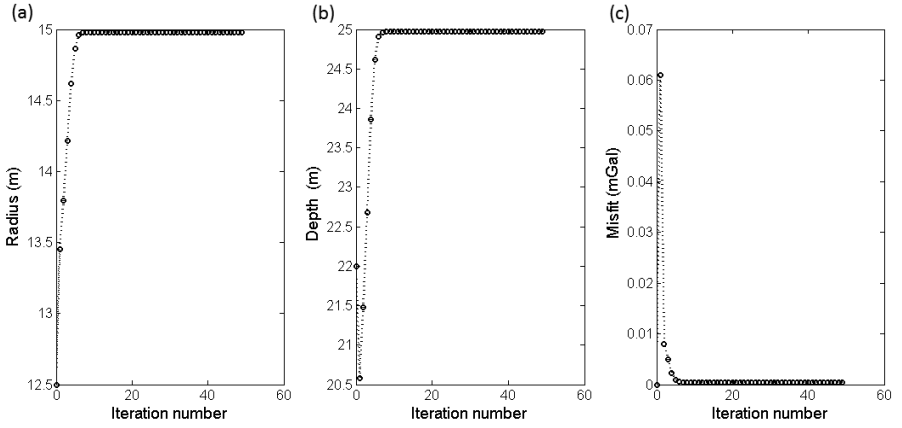

Fig. 6. Improvements of the structures parameters and misfit function versus iteration number for the assumed sphere model in Fig. 5.

Fig. 7a shows the computed gravity anomaly from the inferred structure which is shown in Fig. 7b. The numerical results for the free noise data and contaminated data with the random noise are summarized in Tables 1 and 2, respectively.

Table 1. Numerical results evaluated from the initial and assumed structural parameters for the each three models.

Model	Sphere		Horizontal cylinder		Vertical cylinder	
Parameter	Depth (m)	Radius (m)	Depth (m)	Radius (m)	Depth (m)	Radius (m)
Initial	25	15	30	10	30	10
Assumed	30	12	35	7	34	8
Estimated	24.998	15.001	29.999	9.997	30	10
Error %	0.008	0.007	0.003	0.03	0	0

Table 2. Numerical results evaluated from the initial and assumed structural parameters for the each three models after adding 10% noise to the gravity response of the initial parameters.

Model	Sphere		Horizontal cylinder		Vertical cylinder	
Parameter	Depth (m)	Radius (m)	Depth (m)	Radius (m)	Depth (m)	Radius (m)
Initial	25	15	30	10	30	10
Assumed	22	12.5	27	12	27	11.8
Estimated	24.97	14.98	30.035	9.96	29.84	9.92
Error %	0.12	0.133	0.12	0.4	0.53	0.8

To test the stability of the Marquardt inversion, two different initial sphere models were assumed to investigate the gravity anomalies related to them with and without a random noise of 10% (Table 3 and 4). The inferred structural parameters simulate almost the assumed ones.

Table 3. Numerical results evaluated from the various initial and assumed structural parameters for the each three models.

Model	Sphere				Horizontal cylinder				Vertical cylinder			
Parameter	Depth (m)	Radius (m)	Depth (m)	Radius (m)	Depth (m)	Radius (m)	Depth (m)	Radius (m)	Depth (m)	Radius (m)	Depth (m)	Radius (m)
Initial	35	18	27	10	34	15	27	8	20	15	45	25
Assumed	42	11	19	18	25	10	40	16	13	21	36	30
Estimated	35	18.001	26.997	10	33.998	15.002	27	8.001	20	15	45.003	25
Error %	0	0.006	0.01	0	0.006	0.013	0	0.013	0	0	0.007	0

Table 4. Numerical results evaluated from the various initial and assumed structural parameters for the each three models after adding 10% noise to the gravity response of the initial parameters.

Model	Sphere				Horizontal cylinder				Vertical cylinder			
Parameter	Depth (m)	Radius (m)	Depth (m)	Radius (m)	Depth (m)	Radius (m)	Depth (m)	Radius (m)	Depth (m)	Radius (m)	Depth (m)	Radius (m)
Initial	35	18	27	10	34	15	27	8	20	15	45	25
Assumed	42	11	19	18	25	10	40	16	13	21	36	30
Estimated	35.02	18.04	27.043	9.987	33.76	14.87	27.08	7.96	19.95	14.96	45.063	25.04
Error %	0.057	0.22	0.16	0.13	0.71	0.87	0.3	0.5	0.25	0.27	0.14	0.16

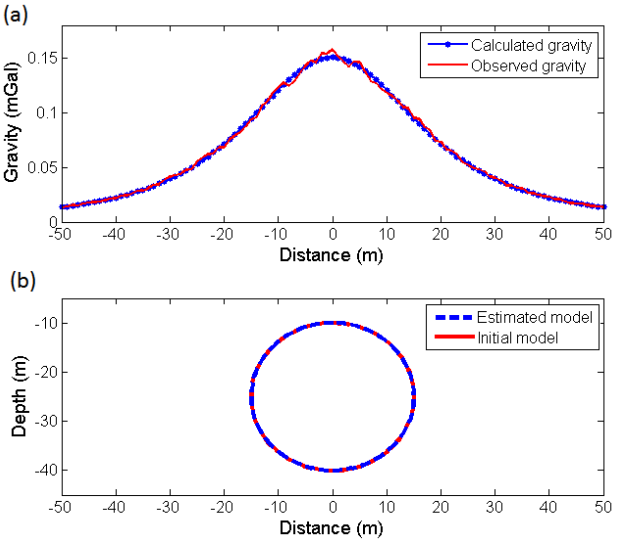

Fig. 7. (a) 10% noise corrupted theoretical gravity and calculated gravity due to, (b) initial and estimated sphere models.

4.2. Horizontal cylinder model

Fig. 8a shows the theoretical and calculated gravity field variations with 1 m interval along a 100 m profile due to an initial horizontal cylinder model with the parameters $z = 30$ m and $R = 10$ m and an assumed horizontal cylinder model with parameters z=35 m and R=7 m (Fig. 8b) where the maximum is the center of the profile and the density contrast is given as $\rho = 1000$ kg/m^3. Hence, the input initial parameters are $z = 35$ m and $R = 7$ m. During inversion, ρ is constant and the model parameters, z and R are progressed iteratively. The allowable values for error (misfit, J), iteration and damping factor (λ) are 0.00000001 mGal, 50 and 12, respectively. The initial damping factor is 0.5.

The misfit, J, reduces intensely from its initial value of 0.265 mGal at the first iteration to 0.0013 mGal at the end of the 6th iteration and then gradually reaches 0.00000000753 mGal at the 15th iteration (Fig. 9c). Because the misfit, J, obtained a value smaller than the allowable error value at the 15th echo, the iteration stopped and therefore the depth and radius

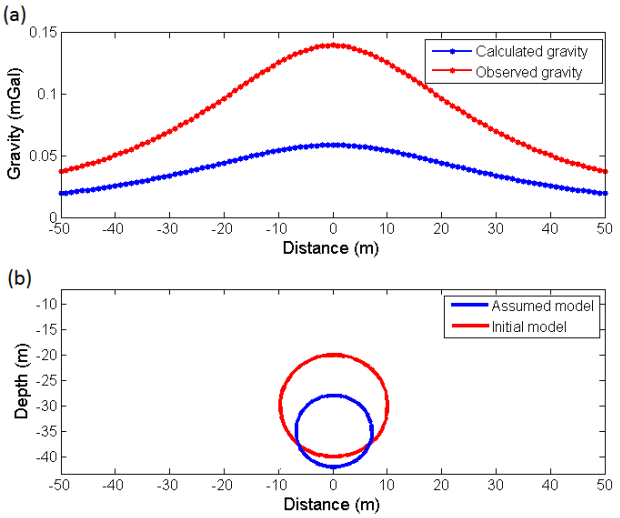

Fig. 8. (a) Theoretical and calculated gravity due to, (b) initial and assumed horizontal cylinder models.

estimates at 14th iteration are the best response of the inverse modeling process.

Fig. 9a and 9b shows the variations of the model parameters z and R versus the iteration number. The conclusive obtained parameters values

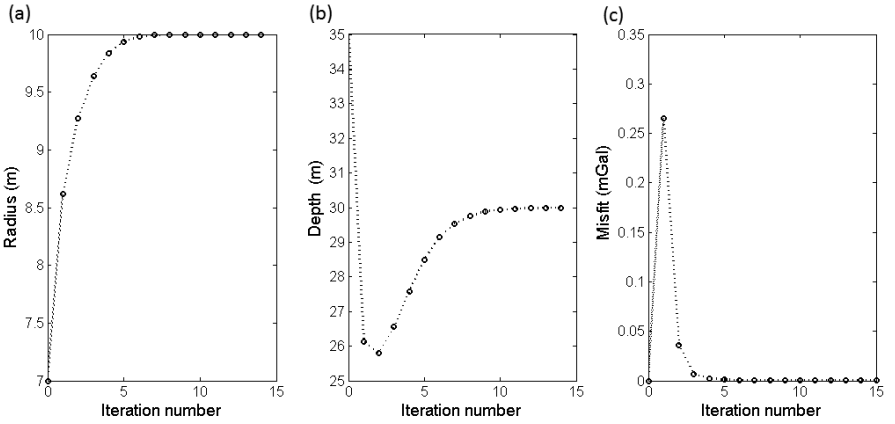

Fig. 9. Improvements of the structures parameters and misfit function versus iteration number for the assumed horizontal cylinder model in Fig. 8.

are $z = 29.999$ m and $R = 9.997$. Fig. 10a exhibits the computed gravity anomaly from the resulted model which is shown in Fig. 10b. The error value in the appraisal of the model parameters, that is, depth and radius are 0.003 m and about 0.03 m, respectively.

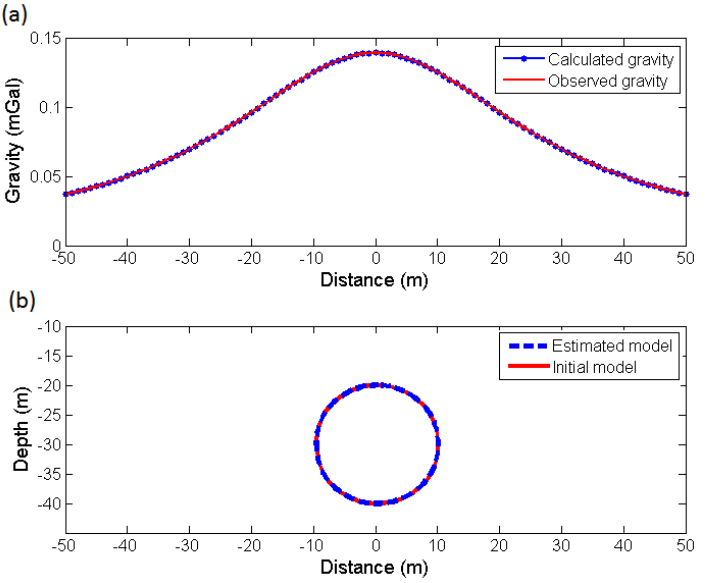

Fig. 10. (a) Theoretical and calculated gravity due to, (b) initial and estimated horizontal cylinder models.

The efficacy of error has been evaluated by adding 10% random noise to the gravity response of the initial horizontal cylinder model (Fig. 11a) using the equation (11). The initial values for the parameters of the assumed horizontal cylinder model are given as $z = 27$ m and $R = 12$ m (Fig. 11b). The allowable values for error (misfit, J), iteration and damping factor (λ) are 0.00001 mGal, 100 and 15, respectively. The initial damping factor is 0.2. The misfit, J, reduces quickly from its initial value of 0.247 mGal at the first iteration to 0.0016 mGal at the end of the 4th iteration and then incrementally attains 0.00074 mGal after the 79th iteration (Fig. 12c). The iteration finished at the 79th iteration where the damping factor value exceeded from the allowable value. The final values of the evaluated depth and radius are 30.035 m and 9.96 m, respectively (Fig. 12a,b). The error value in the estimation of the model parameters, that is, depth and radius

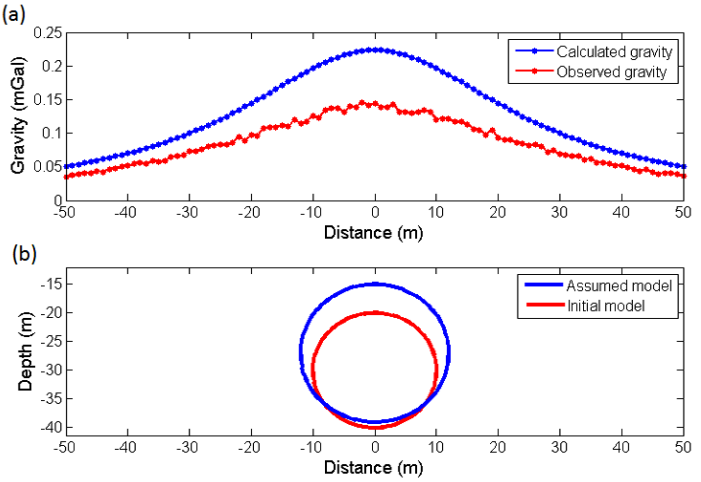

Fig. 11. (a) 10% noise corrupted theoretical gravity and calculated gravity due to, (b) initial and assumed horizontal cylinder models.

are about 0.12 m and 0.4 m, respectively.

Fig. 13a shows the generated gravity anomaly of the final structure that is derived from the estimated parameters as shown in Fig. 13b. The numerical results for the gravity data, with and without random noise are tabulated in Tables 2 and 1, respectively.

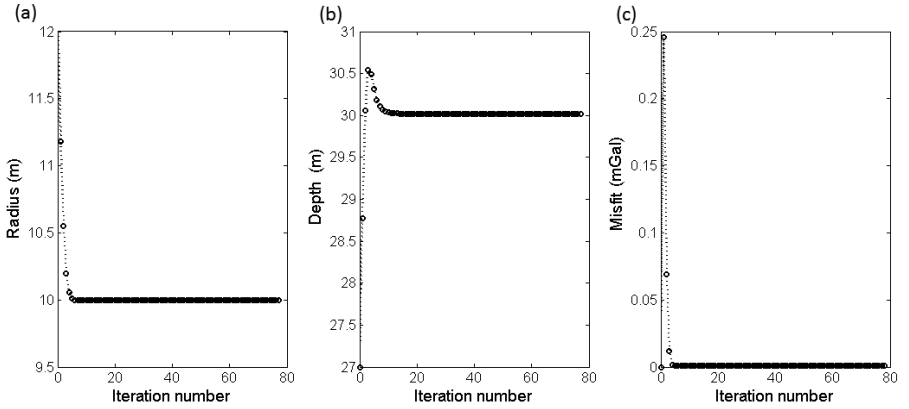

Fig. 12. Improvements of the structures parameters and misfit function versus iteration number for the assumed horizontal cylinder model in Fig. 11.

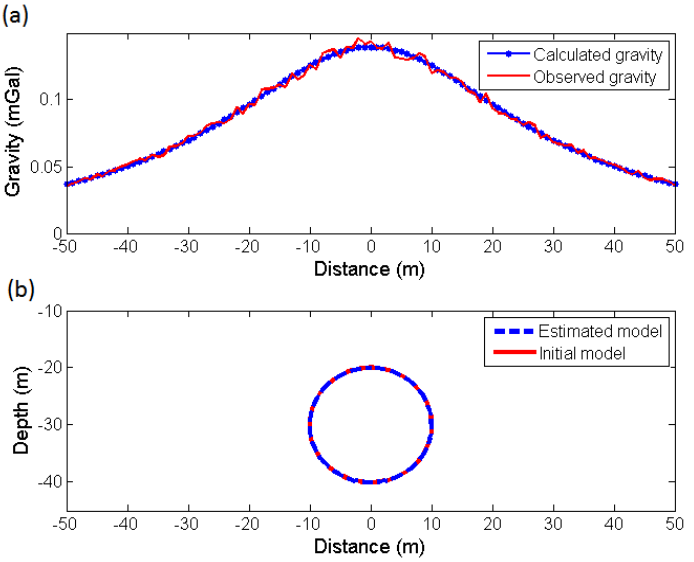

Fig. 13. (a) 10% noise corrupted theoretical gravity and calculated gravity due to, (b) initial and estimated horizontal cylinder models.

For evaluating the convergence of the Marquardt inversion, two different initial horizontal cylinder models were assumed to consider the gravity anomalies related to them with and without a random noise of 10% (Table 3 and 4). The estimated structural parameters approximately mimic the supposed ones.

4.3. Vertical cylinder model

The theoretical and calculated gravity field variations with 1 m interval along a 100 m profile due to an initial infinite vertical cylinder model with the parameters $z = 30\,\mathrm{m}$ and $R = 10\,\mathrm{m}$ is shows in Fig. 14a and an assumed infinite vertical cylinder model with parameters $z = 34$ m and $R = 8$ m is shown in Fig. 14b, as the maximum is the center of the profile and the density contrast is given as $\rho = 1000\,\mathrm{kg/m^3}$. Hence, the input initial parameters are $z = 34\,\mathrm{m}$ and $R = 8\,\mathrm{m}$. During inversion, ρ is fixed and the model parameters, z and R are amended iteratively. The allowable values for error (misfit, J), iteration and damping factor (λ) are $0.0000000001\,\mathrm{mGal}$, 50 and 15, respectively. The initial damping factor is 0.5.

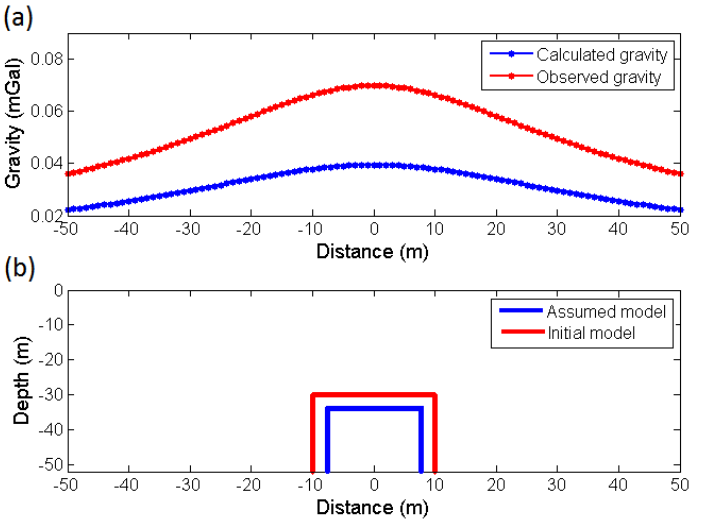

Fig. 14. (a) Theoretical and calculated gravity due to, (b) initial and assumed vertical cylinder models.

The misfit, J, decreases intensely from its initial value of 0.053 mGal at the first iteration to 0.00064 mGal at the end of the 5th iteration and then gradually reaches 0.000000000675 mGal at the 9th iteration and finally attains zero at the end of 10th iteration (Fig. 15c). The depth and radius estimates at 9th iteration are the final evaluated results.

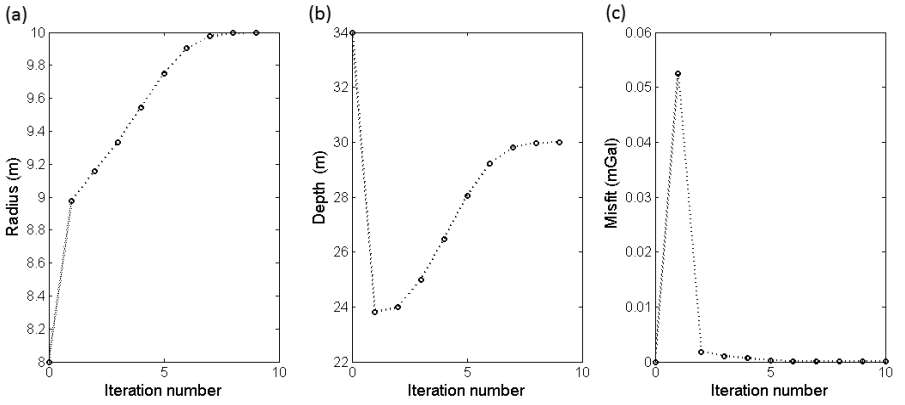

Fig. 15. Improvements of the structures parameters and misfit function versus iteration number for the assumed vertical cylinder model in Fig. 14.

Fig. 15a,b shows the variations of the model parameters z and R versus the iteration number. The values of the final obtained parameters are $z = 30$ m and $R = 10$. Fig. 16a displays the calculated gravity anomaly from the resulted model which is shown in Fig. 16b.

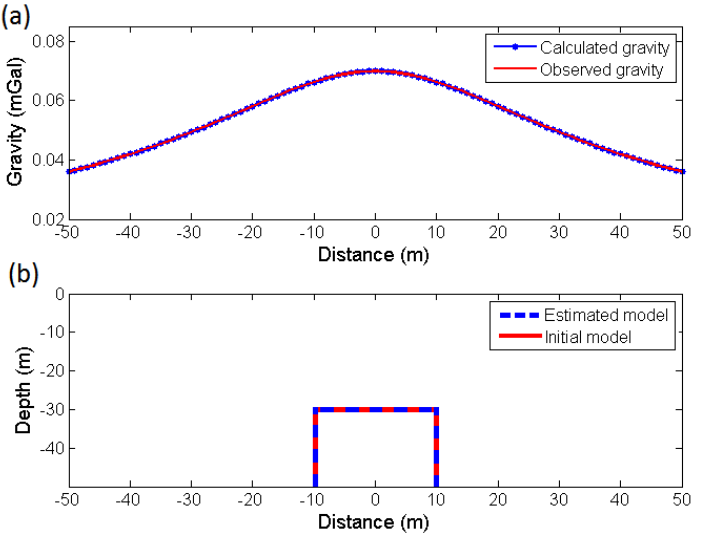

Fig. 16. (a) Theoretical and calculated gravity due to, (b) initial and estimated vertical cylinder models.

The efficiency of the Marquardt inversion method has been investigated by adding 10% random noise to the gravity response of the initial infinite vertical cylinder model (Fig. 17a) using the equation (11). The initial values for the parameters of the assumed vertical cylinder model are given as $z = 27$ m and $R = 11.8$ m (Fig. 17b). The allowable values for error (misfit, J), iteration and damping factor (λ) are 0.0001 mGal, 50 and 12, respectively. The initial damping factor is 0.2. The misfit, J, abates sharply from its initial value of 0.075 mGal at the first iteration to 0.00063 mGal at the end of the 4th iteration and then progressively attains 0.000241 mGal after the 9th iteration as this value remained constant until the iteration number finished (Fig. 18c). The final values of the evaluated depth and radius are 29.84 m and 9.92 m, respectively (Fig. 18a,b). The amount of error in the estimation of the model parameters, that is, depth and radius are about 0.53 m and 0.8 m, respectively.

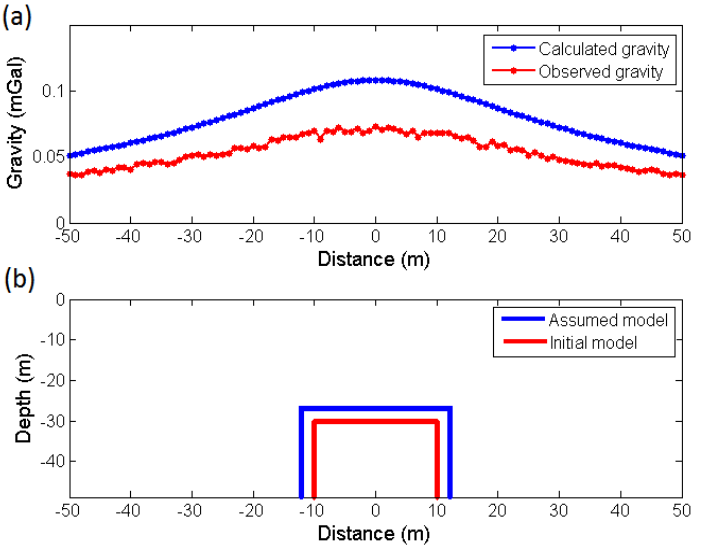

Fig. 17. (a) 10% noise corrupted theoretical gravity and calculated gravity due to, (b) initial and assumed vertical cylinder models.

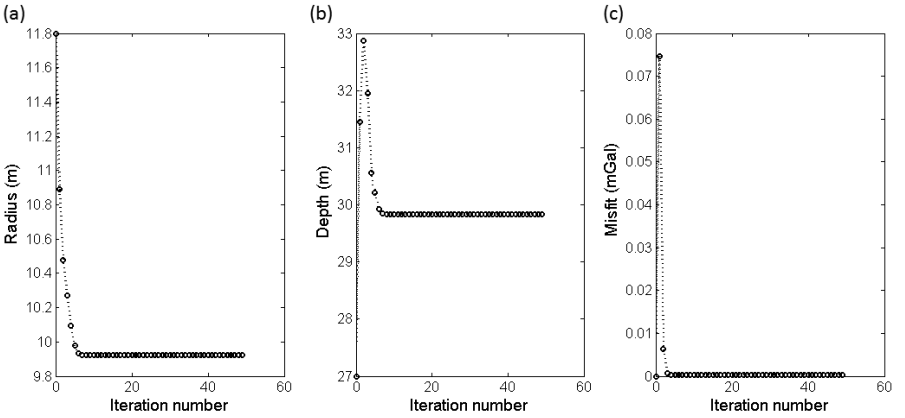

Fig. 18. Improvements of the structures parameters and misfit function versus iteration number for the assumed vertical cylinder model in Fig. 17.

Fig. 19a shows the generated gravity anomaly of the final structure which is inferred from the estimated parameters as shown in Fig. 19b. The numerical results of the gravity data analysis, with and without random noise are given in Tables 2 and 1, respectively.

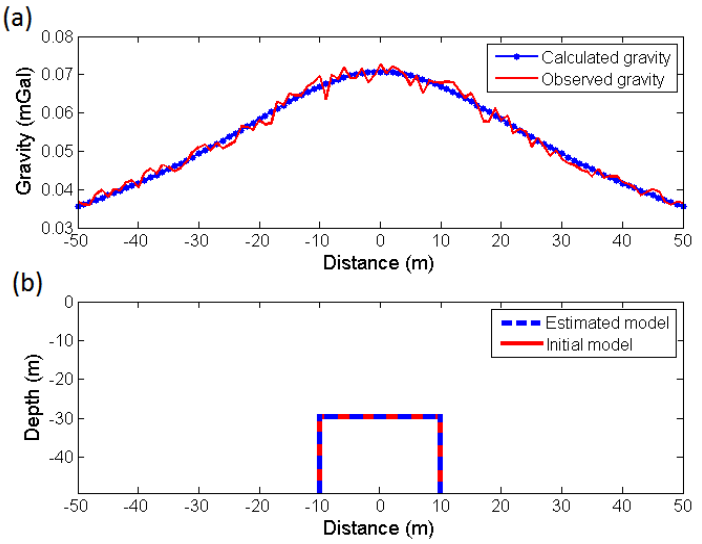

Fig. 19. (a) 10% noise corrupted theoretical gravity and calculated gravity due to, (b) initial and estimated vertical cylinder models.

To examine the constancy and efficiency of the Marquardt inversion, two different initial vertical cylinder models were presumed to analyze the gravity anomalies related to them with and without a random noise of 10% (Table 3 and 4). The estimated structural parameters are almost corresponding to the assumed ones.

5. Field example

The site under survey is located in the east of Iran, around Sabzevar. The outcomes of the stones in the this area are mostly the alkali and ultrabasic igneous rocks and ophiolite as the chromite mineralization can be found in these rocks (Fig. 20).

In this region, the chromite deposits are massive. Fig. 21 shows the Bouguer gravity anomalies map of the area under consideration. It is worth mentioning, the average density computed by the Nettleton's graphical method for this area is given as 2.8 gr/cm^3. The value obtained for the density has been considered for the Bouguer correction. The gravity measurement was done along 12 profiles with a station interval of about 10 m.

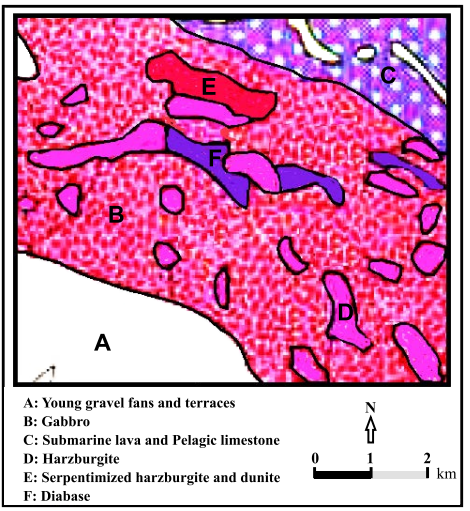

Fig. 20. The geological map of the region under investigation adapted from the Sabzevar 1/250000 geological map (Geological Survey & Mineral Explorations of Iran – *GSI, 2019*).

The gravity data covering a 120 × 100 m area of the Sabzevar region.

For reaching to the residual gravity anomalies which is our desire, the regional gravity anomalies must be removed using a trend (degree 2) from the Bouguer anomaly. Fig. 22 displays the map of the computed local grav-

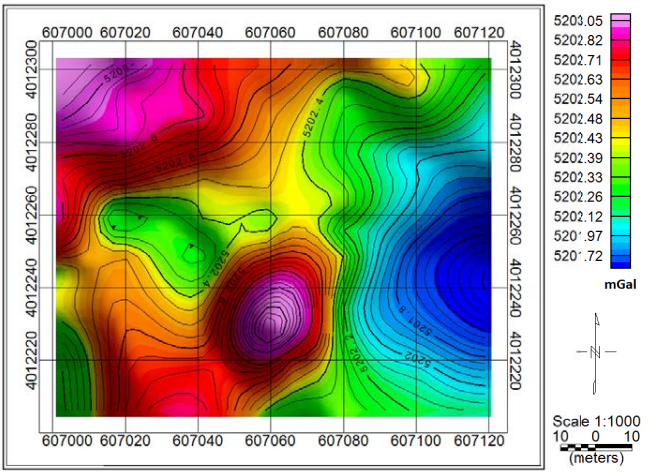

Fig. 21. The Bouguer gravity anomalies map of the area under consideration.

ity field. The host rock of the chromite have the positive density contrast than the surrounding formation, therefore on the residual gravity anomalies map is appeared as the positive anomaly. The average density of the chromite mass is about $4.5\,\mathrm{gr/cm^3}$, whereas the density of the encompassing formation is between $3\,\mathrm{gr/cm^3}$ to $3.5\,\mathrm{gr/cm^3}$. The positive gravity anomaly related to the chromite deposit has been outlined with gray in Fig. 22. Here, we analyze the residual gravity field variations along the profile AA' which runs across the chromite mineral mass in a approximately W–E direction as is shown in Fig. 22. The length of profile is 42 m and the gravity sampling interval is given as 2 m.

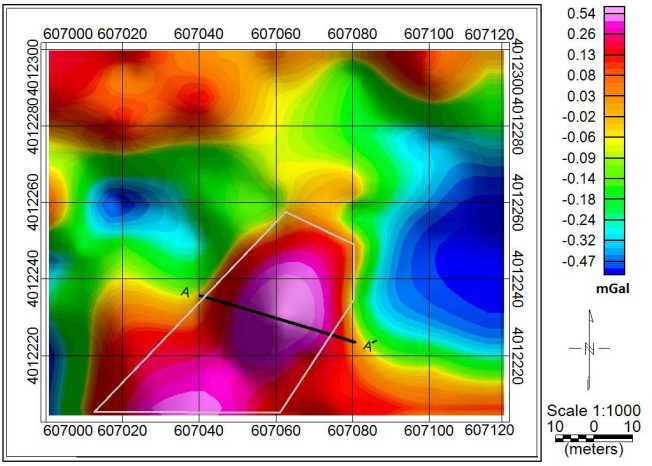

Fig. 22. The local gravity anomalies map. Gravity data from the chromite mass outlined in gray. Profile AA' has been shown on the positive gravity anomaly in a approximately W–E direction.

We applied the Marquardt inversion for the real gravity data where the causative mass shape was assumed as a sphere, an infinite horizontal cylinder and a semi-infinite vertical cylinder, separately. The initial values of the depth and radius parameters are given as $z = 50$ m and $R = 15$ m for the sphere model, $z = 40$ m and $R = 25$ m for the infinite horizontal cylinder model and $z = 25$ m and $R = 15$ m for the semi-infinite vertical cylinder model (Table 5). For each three supposed structure under consideration, the assigned values for misfit (J), iteration and damping factor (λ) are 0.001 mGal, 100 and 20, respectively. The variability of each shape param-

eter and misfit of the sphere, infinite horizontal cylinder and semi-infinite vertical cylinder geometry models against the iteration number during inversion process are shown in Figs. 23–25, respectively.

The performed iteration for the sphere, infinite horizontal cylinder and semi-infinite vertical cylinder configurations are 89, 74 and 77, respectively, before it was ceased, as in the end of these iteration numbers, the damping factor obtained a value greater than the allowable value. The depth and radius parameters and misfit abided constant after the 9th iteration in the case of the sphere shape, the 11th iteration in the case of the horizontal cylinder shape and the 6th iteration in the case of the vertical cylinder shape. The inverted structural parameters are given in Table 5.

Table 5. Inferred numerical results from analyzing the real gravity data along the profile AA' cross-section and the gravity response of the assumed parameters for the each three structural shapes.

Model	Sphere		Horizontal cylinder		Vertical cylinder	
Parameter	Depth (m)	Radius (m)	Depth (m)	Radius (m)	Depth (m)	Radius (m)
Assumed	50	15	40	25	25	15
Estimated	24.7	19.8	8.1	11.6	7.4	11.7
Misfit (mGal)	1.192		0.176		0.375	

The theoretical gravity anomaly along profile AA' and modeled gravity anomalies corresponding to the estimated parameters in the latest misfit function values are shown in Fig. 26. Since the least misfit function value

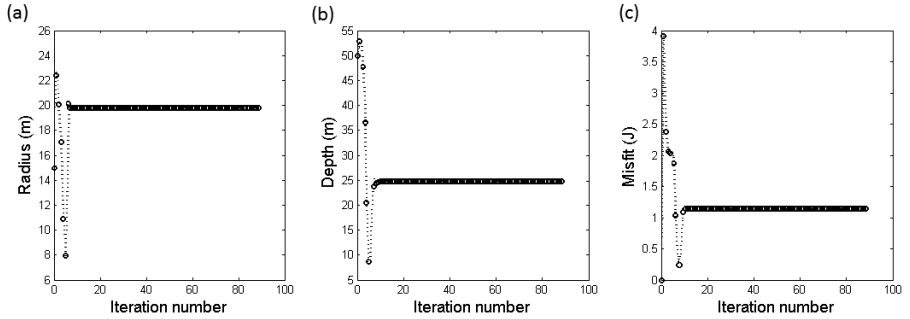

Fig. 23. Modifications of the structures parameters and misfit function versus iteration number based on assumed parameters for the sphere model as given in Table 5.

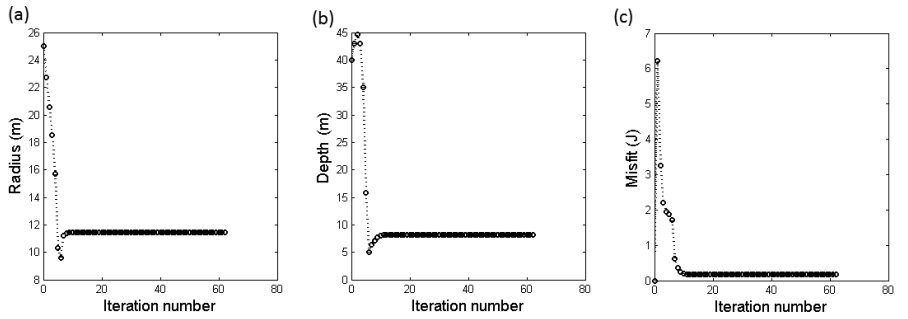

Fig. 24. Modifications of the structures parameters and misfit function versus iteration number based on assumed parameters for the horizontal cylinder model as given in Table 5.

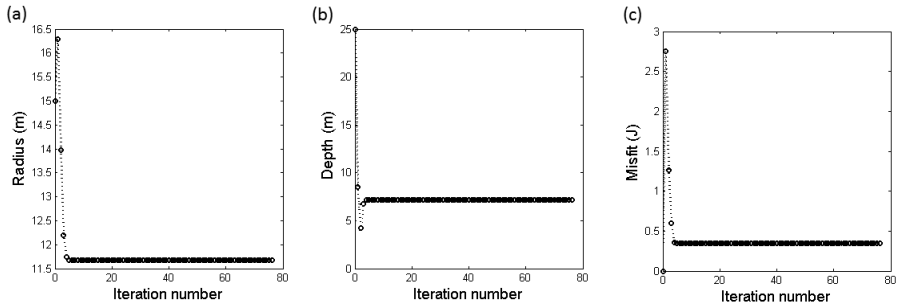

Fig. 25. Modifications of the structures parameters and misfit function versus iteration number based on assumed parameters for the vertical cylinder model as given in Table 5.

(minimum error) indicate the best shape for the anomaly sources, with attention to Table 5, the horizontal cylinder model with a misfit value of 0.176 mGal, a depth of 8.1 m and a radius of 11.55 m must be the best form that can imagine for the anomaly causative body. But the computed structural parameter demonstrate a unrealistic structure, because if a subsurface source with the horizontal cylinder feature whose depth be 8.1 m, the maximum value which the radius can possess, is equal the depth of the center of the model, while the inverted radius for the horizontal cylinder model is 11.6 m. The average values of the depth and radius parameters estimated by the Marquardt inversion for the vertical cylinder model are 7.45 m and 11.7 m and for the sphere model are 24.8 m and 19.9 m, respectively. There is a sharp discrepancy between the observed gravity (green curve in Fig. 26) and computed gravity response based on the inverted sphere model param-

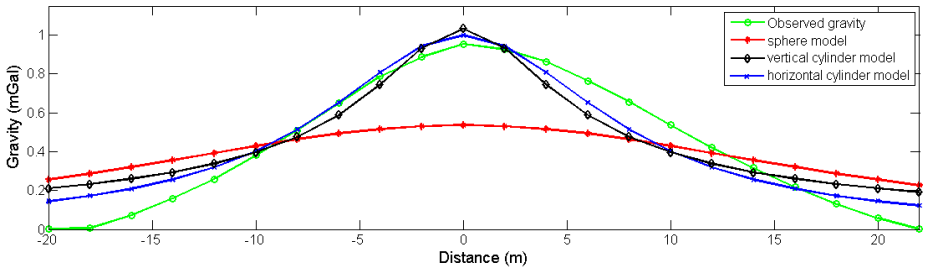

Fig. 26. The observed gravity along the profile AA' (green curve) and inverted gravity from the interpreted parameters for the assumed sphere model (red curve), horizontal cylinder model (blue curve) and vertical cylinder model (black curve).

eters (red curve in Fig. 26). As a result, the obtained value for the misfit, is larger than two other models and indicate the gravity anomaly source can't be sphere shape. Therefore, the best suitable geometric shape which can consider for the anomaly causative mass, i.e. chromite deposit, is the vertical cylinder form, because obtained misfit for the vertical cylinder model is smaller than one calculated for the sphere model.

The permanency and isotropy of the interpreted parameters from the real gravity data were investigated using different assumed values for the each three case of the models. The input and output values are summarized in Table 6. The estimated structural parameters illustrate a very slight differences that confirm the stability of the method.

The Euler deconvolution method is a common technique in potential fields study which is widely used for estimating the depth of the anomaly

Table 6. Inferred numerical results from analyzing the real gravity data along the profile AA' cross-section and the gravity response of the different assumed parameters for the each three structural shapes.

Model	Sphere				Horizontal cylinder				Vertical cylinder			
Parameter	Depth (m)	Radius (m)	Depth (m)	Radius (m)	Depth (m)	Radius (m)	Depth (m)	Radius (m)	Depth (m)	Radius (m)	Depth (m)	Radius (m)
Assumed	28	10	55	30	35	20	30	15	18	12	10	15
Estimated	24.8	19.7	24.8	20.1	8.1	11.5	8.1	11.6	7.5	11.7	7.4	11.7
Misfit (mGal)	1.191		1.194		0.175		0.176		0.376		0.375	
Iteration	95		85		71		64		67		53	

source (*Thompson, 1982; Reid et al., 1990; Barbosa and Silva, 2011*). In this study, for comparison the depth estimates from gravity data, we have employed the Euler method for calculating the depth of the chromite mineral mass by choosing a structure index of 1 and a window size of 5×5 points. Fig. 27 show the solutions obtained from Euler deconvolution as plotted on the residual gravity anomaly map. The Euler solutions located on the gravity anomaly present a depth between 5 to 10 m for the buried deposit.

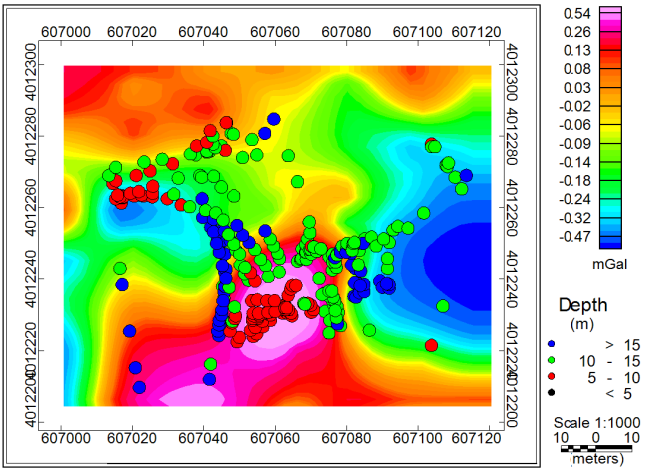

Fig. 27. The residual gravity anomalies overlaid by solutions of the 3D Euler method.

6. Conclusions

In this paper, we have introduced a optimization approach based on the Marquardt's algorithm for the inverse modeling of the residual gravity anomaly due to the simple geometric shapes, i.e. sphere, infinite horizontal cylinder and semi-infinite vertical cylinder. To check the constancy of the procedure and the convergency of the parameters attained from the Marquardt inversion, the free-noise and noise-impregnated theoretical gravity data related to the different initial models were used in each case and it was eventuated that the inversion yields almost the same solutions in all cases. Therefore, the stable and accurate solutions verify the reliability and applicability of the Marquardt's algorithm as a powerful and useful inverse modeling tools.

The method was applied for estimating the structure parameters and determining the geometric shape using the gravity anomaly of a chromite deposit from Iran. The minimum misfit value was considered as a criterion for selecting the best mass shape, provided that the estimated parameters depict a acceptable structure naturally. The amount of misfit obtained for the assumed sphere models after 95 and 85 iterations is 1.191 mGal and 1.194 mGal, for assumed horizontal cylinder models after 71 and 64 iterations is 0.175 mGal and 0.176 mGal and for assumed vertical cylinder models after 67 and 53 iterations is 0.376 mGal and 0.375 mGal, respectively. Although the lowest estimated misfit is related to the horizontal cylinder model, but with attention to the inferred parameters for the horizontal cylinder models from the inversion, that is an average depth and radius of 8.1 m and 11.55 m respectively, these amounts do not demonstrate a subsurface body. The inverted gravity from the final interpreted parameters of this procedure for various assumed vertical cylinder models is very close to the real gravity along profile AA' cross-section. Therefore, it can be found that the anomaly causative mass shape is approximately the vertical cylinder form geometrically and depth and radius of the deposit are about 7.4 m and 11.7 m. This evaluated depth has good conformity with the Euler solutions.

References

Abdelrahman E. M., Bayoumi A. I., Abdelhady Y. E., Gobashy M. M., El-Araby H. M., 1989: Gravity interpretation using correlation factors between successive least-squares residual anomalies. Geophysics, **54**, 12, 1614–1621, doi: 10.1190/1.1442629.

Abdelrahman E. M., Bayoumi A. I., El-Araby H. M., 1991: A least-squares minimization approach to invert gravity data. Geophysics, **56**, 1, 115–118, doi: 10.1190/1.1442946.

Abdelrahman E. M., El-Araby T. M., 1993a: A least-squares minimization approach to depth determination from moving average residual gravity anomalies. Geophysics, **58**, 12, 1779–1784, doi: 10.1190/1.1443392.

Abdelrahman E. M., El-Araby H. M., 1993b: Shape and depth solutions from gravity using correlation factors between successive least-squares residuals. Geophysics, **58**, 12, 1785–1791, doi: 10.1190/1.1443393.

Al-Garni M. A., 2013: Inversion of residual gravity anomalies using neural network. Arab. J. Geosci., **6**, 5, 1509–1516, doi: 10.1007/s12517-011-0452-y.

Asfahani J., Tlas M., 2008: An automatic method of direct interpretation of residual gravity anomaly profiles due to spheres and cylinders. Pure Appl. Geophys., **165**, 5, 981–994, doi: 10.1007/s00024-008-0333-9.

Barbosa V. C. F., Silva J. B. C., 2011: Reconstruction of geologic bodies in depth associated with a sedimentary basin using gravity and magnetic data. Geophys. Prospect., **59**, 6, 1021–1034, doi: 10.1111/j.1365-2478.2011.00997.x.

Bowin C., Scheer E., Smith W., 1986: Depth estimates from ratios of gravity, geoid, and gravity gradient anomalies. Geophysics, **51**, 1, 123–136, doi: 10.1190/1.1442025.

Chakravarthi V., Sundararajan N., 2004: Ridge-regression algorithm for gravity inversion of fault structures with variable density. Geophysics, **69**, 6, 1394–1404, doi: 10.1190/1.1836814.

Chakravarthi V., Sundararajan N., 2005: Gravity modeling of $2^{1/2}$-D sedimentary basins – a case of variable density contrast. Comput. Geosci., **31**, 7, 820–827, doi: 10.1016/j.cageo.2005.01.018.

Chakravarthi V., Sundararajan N., 2006: Gravity anomalies of 2.5-D multiple prismatic structures with variable density: A Marquardt inversion. Pure Appl. Geophys., **163**, 1, 229–242, doi: 10.1007/s00024-005-0008-8.

Chakravarthi V., Sundararajan N., 2007: Marquardt optimization of gravity anomalies of anticlinal and synclinal structures with prescribed depth-dependent density. Geophys. Prospect., **55**, 4, 571–587, doi: 10.1111/j.1365-2478.2007.00625.x.

Chakravarthi V., Sundararajan N., 2008: TODGINV-A code for optimization of gravity anomalies due to anticlinal and synclinal structures with parabolic density contrast. Comput. Geosci., **34**, 8, 955–966, doi: 10.1016/j.cageo.2007.11.002.

Eshaghzadeh A., Kalantari R. A., 2015: Anticlinal Structure Modeling with Feed Forward Neural Networks for Residual Gravity Anomaly Profile. Proceedings of the 8th Congress of the Balkan Geophysical Society, 5-8 October 2015, Chania, Greece, doi: 10.3997/2214-4609.201414210.

Eshaghzadeh A., Hajian A., 2018: 2D inverse modeling of residual gravity anomalies from Simple geometric shapes using Modular Feed-forward Neural Network. Ann. Geophys.-Italy, **61**, 1, SE115, doi: 10.4401/ag-7540.

Essa K. S., 2007: A simple formula for shape and depth determination from residual gravity anomalies. Acta Geophys., **55**, 2, 182–190, doi: 10.2478/s11600-007-0003-9.

Gupta O. P., 1983: A least-squares approach to depth determination from gravity data. Geophysics, **48**, 3, 357–360. doi: 10.1190/1.1441473.

Hammer S., 1977: Graticule spacing versus depth discrimination in gravity interpretation. Geophysics, **42**, 1, 60–65, doi: 10.1190/1.1440714.

GSI, 2019: Geological Survey & Mineral Explorations of Iran, website, accessed 15 May 2019, https://www.gsi.ir/.

Lines L. R., Treitel S., 1984: A review of least-squares inversion and its application to geophysical problems. Geophys. Prosp., **32**, 2, 159–186, doi: 10.1111/j.1365-2478.1984.tb00726.x.

Marquardt D. W., 1963: An algorithm for least-squares estimation of nonlinear parameters. J. Soc. Indust. Appl. Math., **11**, 2, 431–441, doi: 10.1137/0111030.

McCowan D. W., Abdelrahman E. M., 1990: On "A least-squares approach to depth determination from gravity data" by O. P. Gupta. Geophysics, **55**, 376–378, doi: 10.1190/1.1442846.

Mohan N. L., Anandababu L., Rao S., 1986: Gravity interpretation using the Mellin transform. Geophysics, **51**, 1, 114–122, doi: 10.1190/1.1442024.

Odegard M. E., Berg J. W., 1965: Gravity interpretation using the Fourier integral. Geophysics, **30**, 3, 424–438, doi: 10.1190/1.1439598.

Osman O., Muhittin A. A., Ucan O. N., 2006: A new approach for residual gravity anomaly profile interpretations: Forced Neural Network (FNN). Ann. Geophys.-Italy, **49**, 6, 1201–1208, doi: 10.4401/ag-3099.

Osman O., Muhittin A. A., Ucan O. N., 2007: Forward modeling with Forced Neural Networks for gravity anomaly profile. Math. Geol., **39**, 593–605, doi: 10.1007/s11004-007-9114-8.

Reid A. B., Allsop J. M., Granser H., Millet A. J., Somerton I. W., 1990: Magnetic interpretation in three dimensions using Euler deconvolution. Geophysics, **55**, 1, 80–91, doi: 10.1190/1.1442774.

Salem A., Ravat D., Johnson R., Ushijima K., 2001: Detection of buried steel drums from magnetic anomaly data using a supervised neural network. J. Environ. Eng. Geoph., **6**, 3, 115–122, doi: 10.4133/JEEG6.3.115.

Saxov S., Nygaard K., 1953: Residual anomalies and depth estimation. Geophysics, **18**, 4, 913–928, doi: 10.1190/1.1437945.

Sharma B., Geldart L. P., 1968: Analysis of gravity anomalies of two-dimensional faults using Fourier transforms. Geophys. Prosp., **16**, 1, 77–93, doi: 10.1111/j.1365-2478.1968.tb01961.x.

Shaw R. K., Agarwal N. P., 1990: The application of Walsh transforms to interpret gravity anomalies due to some simple geometrically shaped causative sources: A feasibility study. Geophysics, **55**, 7, 843–850, doi: 10.1190/1.1442898.

Thompson D. T., 1982: EULDPH: A new technique for making computer assisted depth estimates from magnetic data. Geophysics, **47**, 1, 31–37, doi: 10.1190/1.1441278.

sciendo

Contributions to Geophysics and Geodesy Vol. 49/2, 2019 (181–194)

Fracture zones detection for groundwater exploration integrating Resistivity Profiling and Very Low Frequency electromagnetic methods (Errachidia basin, Morocco)

Youssef AIT BAHAMMOU[1,*], Ahmed BENAMARA[2], Abdellah AMMAR[1], Ibrahim DAKIR[3]

[1] Mohammed V University, Laboratory of Geophysics and Natural Risks, Faculty of Sciences, Rabat-Agdal, Morocco; e-mail: y.aitbahammou@gmail.com, siadamammar@yahoo.fr

[2] Moulay Ismail University, Laboratory of Applied Geophysics, Faculty of Sciences and Techniques, Errachidia, Morocco; e-mail: benamara13003@gmail.com

[3] Abdelmalek Essaadi University, Faculty of Sciences, Department of Geology, Tetouan, Morocco; e-mail: dakiribrahim@gmail.com

Abstract: Resistivity Profiling and Very Low Frequency (VLF) electromagnetic methods were introduced to study fracture zones detection in Zaouia Jdida locality, within the Errachidia basin. The Horizontal Profiling was conducted in Wenner-α array, with $AB =$ 300 m and profile lines oriented NW–SE and NE–SW. The resistivity measurements were taken using MAE advanced geophysics instruments. The VLF profiles were implanted with the length reaches 1000 m and profile lines oriented in NE–SW direction. The VLF measurements were collected using T-VLF iris instrument and the data filtering was done using KHFFILT software. Two filters, Karous-Hjelt and Fraser, were applied to the real component of the secondary electromagnetic field. The qualitative interpretation of resistivity results, showed the presence of subsurface targets; fracture zones were detected at 70m, 240m and 450m positions along the profile P1, at 180m, 340m and 450m positions from the profile P2. The semi-quantitative interpretation of VLF results revealed the presence of two principal fracture zones at L3 and L5 locations, oriented NW–SE, at a depth range of 30 m to 60 m. The VLF anomaly observed at L3 location is confirmed by the resistivity measurements from the profile P1 (at 70m station). The identified fractures represent the potential zones for groundwater supply and then will have an implication on storage and movement of groundwater in the prospect area.

Key words: Errachidia basin, fracture zone, Resistivity, Very Low Frequency, data filtering, groundwater exploration

*corresponding author

doi: 10.2478/congeo-2019-0009

1. Introduction

The region of Errachidia-Tafilalt, which includes the study area, faces various environmental difficulties, including the scarcity and salinization of groundwater (*Ammary, 2007*). In this arid to semi-arid zone, the overexploitation of groundwater, as a result of demographic pressure and agricultural activities, has contributed to the decline in water table levels (*Ammary, 2007*). Given the scarcity of geophysical studies undertaken in the study area and for the sustainable use of water, it is necessary to implement geophysical investigation methods to better recognize the aquifer systems in the region.

The problematic aimed by this work, is around the potential groundwater within the area of Ain El Atti, in Zaouia Jdida locality. The present paper contributes to evaluate this potential by detecting fracture zones. The fracture zones represent a special target for hydrogeological exploration and can play an important role for groundwater supply and hydrogeological practice (*Kirsch, 2006*). Generally, fracture zones are considered hydraulic conductors (*Kirsch, 2006*). To achieve the purpose of this paper, on one hand, the working procedure will be based on the Resistivity Profiling, in order to determine the horizontal variation of resistivity. On the other hand, it will be based on the Very Low Frequency electromagnetic (VLF-EM) technique with the aim of measuring the parameters of the secondary electromagnetic field.

The Horizontal Profiling method was chosen for this study, because it is a common method to measure horizontal variation of electrical resistivity. It has been recognized to be more suitable for hydrogeological exploration of sedimentary basin. Generally, the resistivity method reveals an important result during the detection of fractured zones and metalliferous veins (*Dakir et al., 2019*). The VLF-EM method is widely used for the detection of buried conductive targets, including aquiferous faulting systems (*Ogilvy and Lee, 1991*). It offers relatively a fast approach to delineate the fractures (*Benson et al., 1997*). The advantage of this technique is that the measurements are easy to be interpreted in a qualitative manner (*Vargemezis, 2007*).

2. Geography and geological setting

The study area is located about 50 km south of Errachidia and 20 km north of Erfoud (Fig. 1). It is a part of Cretaceous basin of Errachidia (South-eastern Morocco). This basin is characterized by a stratigraphic series that ranges from Paleozoic to Quaternary. In the outcrop (Fig. 1), the basin is generally composed of carbonate deposits of Turonian (*Choubert and Faure-Muret, 1962*), sandstone and sand with gypsum intercalation attributed to Infracenomanian and sand clay with gypsum and anhydrite of Senonian (*Choubert, 1948*). Locally, from drilling data, the Infracenomanian deposits overlie the Paleozoic (angular discordance). The Quaternary is presented by alluvium and conglomerates. It shows varying thickness layers between 5 and 40 m (*Amharref, 1991*).

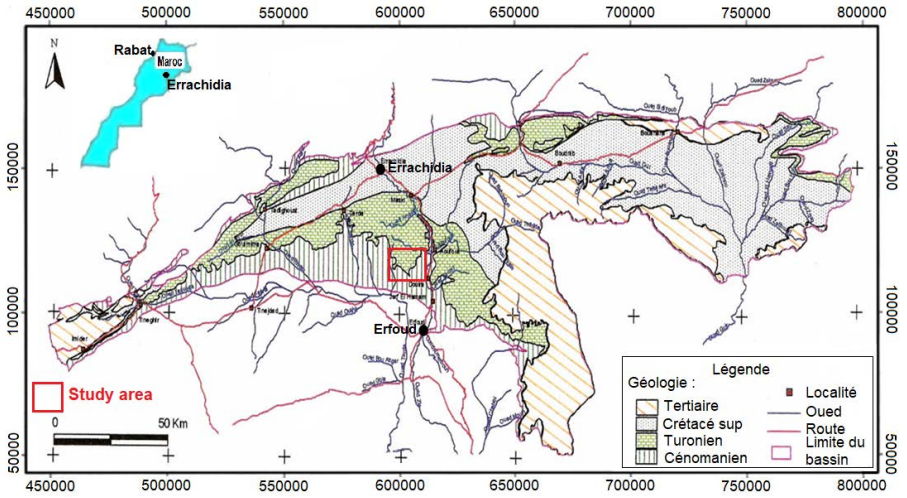

Fig. 1. Geographic situation and regional geology of the study area (*DRH-GRZ, 2007*) modified.

3. Hydrogeological data

The Errachidia basin consists of a multilayer aquifer system consisting of four main aquifer levels (*Margat, 1977*). The quaternary aquifer, in the south part of the Errachidia basin, is formed by alluvial deposits, which

contain the essential reserves of the tablecloth. The senonian aquifer, in the north section of the basin, consists of detritic sediments with some sandstone, sand, red marl, gypsum, sodium chloride and limestone. The turonian aquifer consists of fractured limestone and marine origin dolomite as karst facies. Concerning the infracenomanian artesian aquifer, it is made by continental deposits (sandstones and conglomerates) and lagoon sediments (sand, clay and marl). Its water quality varies from one sector to another (*Aoubouazza et al., 2013*); good quality at the NW of the Ain Al Atti, brackish at Aoufous and highly mineralized between Douira and foundation raft Erfoud (*Ammary, 2007*) where the residue reaches 16 gL^{-1}.

4. Materials and methods

4.1. Resistivity profiling survey

In Wenner array (Fig. 2), the four electrodes with a definite array spacing "a" are moving after each measurement. In each station, the value of resistivity is affected to the center of the array (*Kunetz, 1966*). The resistivity of the ground is measured by injected currents and the resulting potential differences at the surface. Two pairs of electrodes are required: electrodes A and B are used for current injections, while electrodes M and N are for potential difference measurements. The apparent resistivity ρ_a is calculated from the current I and the potential difference ΔV (Eq. 1). The coefficient K is called geometric factor. For Wenner configuration, the factor K can be calculated from the electrode spacing Eq. (2):

$$\rho_a = K \frac{\Delta V_{MN}}{I_{AB}}\,, \tag{1}$$

$$K = 2\pi a\,. \tag{2}$$

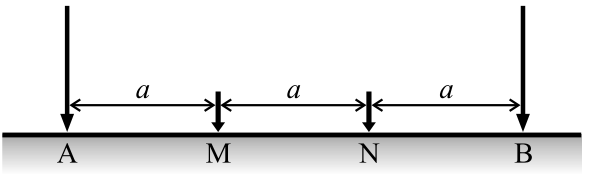

Fig. 2. Wenner configuration used in Resistivity Profiling.

The instrument used in this research work is MAE advanced geophysics instruments. The measure of the filed resistivity is done by a digital Georesistivimeter (4 iterations). The profiles, oriented in NW–SE and NE–SW directions, were conducted using Wenner-α configuration, where the voltage and the current electrodes are closely spaced and fixed to the center of the array. On the field, Four electric horizontal profiles (P1, P2, P3 and P4) with maximum electrode separation $AB = 300\,\mathrm{m}$ ($a = 100\,\mathrm{m}$), were carried out. For each profile, 50 measures were taken with a spacing of 10 m.

4.2. VLF electromagnetic survey

4.2.1. Principle and data acquisition

The Very Low Frequency electromagnetic (VLF-EM) is based on the use of radio waves in the range of 15 to 30 kHz (*Müller et al., 1984*). The signal (primary magnetic field H_p) emitted by the VLF stations, can be captured in the field by the VLF instruments. When a conductor (e.g. a fracture zone) is crossed by the H_p electromagnetic field, an induced current (Current of Foucault) flows through it and produces a secondary magnetic field H_s out-of-phase with H_p, oriented in any direction (*McNeill and Labson, 1991*). In this case, the conductive body acts as a second source (*Kaya et al., 2007*). The resulting field from the sum of H_p and H_s is elliptically polarized. This ellipse of polarisation has two components with the same frequency, but different amplitude and phase (*Eze et al., 2004*). The in-phase H_p is the real component (R_e) proportional to the tilt τ (inclination of the major axis of the ellipse), while the out of phase H_p is the imaginary component (I_m) proportional to the ellipticity ε (the ratio between the minor axis and the major axis b/a). These two components τ and ε are described by the equations (3 and 4) below (*Saydam, 1981*):

$$\tau = R_e/H_p\,, \tag{3}$$

$$\varepsilon = I_m/H_p\,. \tag{4}$$

During our study, the survey was carried out using the Receiver T-VLF Iris Instruments, operating in tilt angle mode, in order to measure the parameters of the ellipse of polarization, which are the tilt τ and the ellipticity ε (Fig. 3). In this mode, it is convenient to operate with a transmitter (VLF

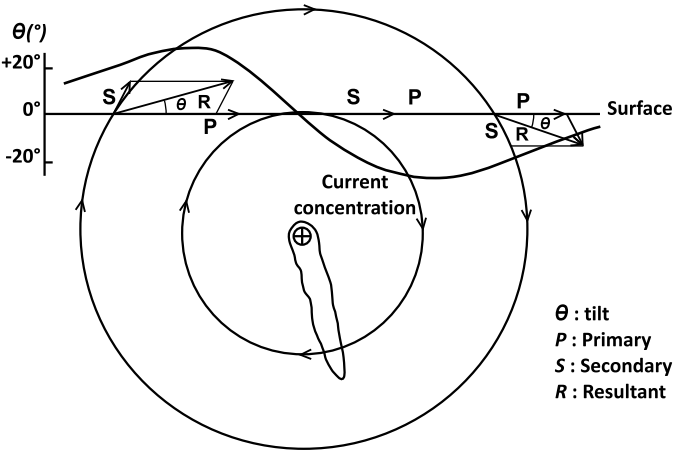

Fig. 3. Principle of induction in a subsurface conductive target and parameters of the ellipse of polarisation in tilt angle mode.

station) which is located in the supposed strike (±45°) of the prospected target for a maximum coupling. For detecting the supposed fractures in the study area, the GBR station located in Rugby (England) has been chosen, with a power of 750 kW, which emits a signal with a frequency of 16 kHz. On the fieldwork, five VLF-EM profiles were conducted, with profile length reaches 1000 m. Readings were taken respecting a spacing of 20 m. The profile lines were oriented in NE–SW direction and denoted as L1 to L5.

4.2.2. Data filtering and semi-quantitative interpretation

For our measurements, on one hand, the Karous and Hjelt (KH) filter has been applied to the real component. This filter permits the draw of apparent current density cross-sections, which show the response of the conductor in depth (*Karous and Hjelt, 1983*). Qualitatively, it is possible to discriminate between conductive and resistive structures using apparent current density cross-section (*Karous and Hjelt, 1977*), where a high positive value corresponds to conductive structure and low negative values are related to resistive one (*Benson et al., 1997; Sharma and Baranwal, 2005*). On the other hand, the Fraser filter has been applied to the real component too, and the filtered data were presented in the form of a contour map. Therefore, the filtered real component will always show a positive peak above

an anomalous zone (*Fraser, 1969*). In order to perform Karous-Hjelt and Fraser filtering on VLF EM data, the software KHFFILT is used in the interpretation of the measurements along VLF traverses.

To better visualize the location of resistivity profiles and VLF lines, the Fig. 4 represents the MNT of the prospect area and the study location.

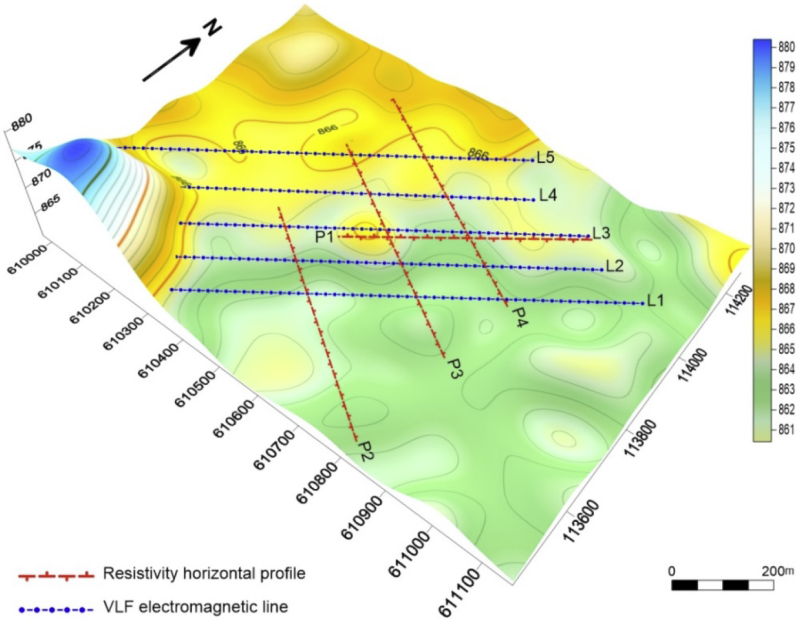

Fig. 4. MNT of the prospect area and study location.

5. Results and discussion

5.1. Resistivity profiling results

For resistivity data, the measurements were plotted against the distance (Fig. 5). For all electrical profiles, there are fluctuations of apparent resistivity curves, covering a distance of 500 m. From the profile P1 (Fig. 5a), a low apparent resistivity (46 Ωm) occurs at the beginning of the profile up to a distance of 70 m. Towards NE, two anomalous values of resistivity are observed; the first one (41 Ωm) is crossed at 240 m and the second (45 Ωm) is situated at 450 m. Along the profile P2 (Fig. 5b), from a distance of

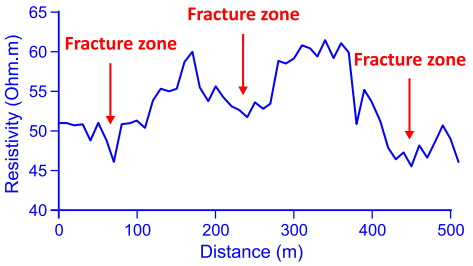

Fig. 5a. The apparent resistivity response against the distance along the profile P1 (NE–SW) with $AB = 300$ m.

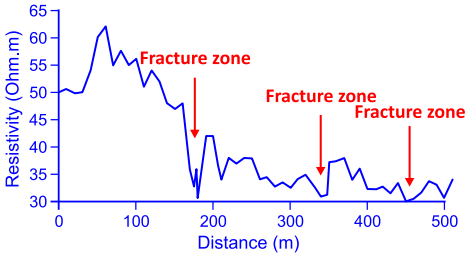

Fig. 5b. The apparent resistivity response against the distance along the profile P2 (NW–SE) with $AB = 300$ m.

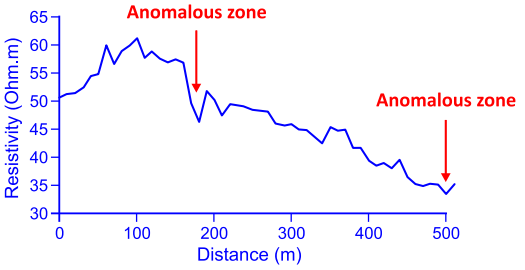

Fig. 5c. The apparent resistivity response against the distance along the profile P3 (NW–SE) with $AB = 300$ m.

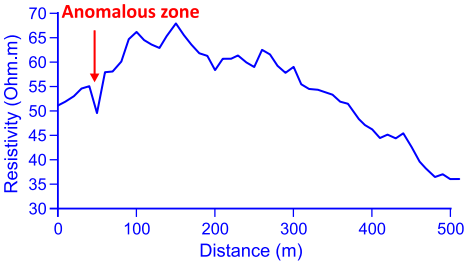

Fig. 5d. The apparent resistivity response against the distance along the profile P4 (NW–SE) with $AB = 300$ m.

60 m and towards SE, the resistivity decreases from 62 Ωm to a very low value of 30 Ωm up to a distance of 450 m. One prominent low resistivity is observed at position 180 m (30.6 Ωm), and two other anomalous zones are revealed at 290 m and 450 m positions. The profile P3 (Fig. 5c) shows that the resistivity increases from the beginning of the profile and reaches a maximum value of 61 Ωm at 100 m position. Towards SE and for the rest of the profile, the resistivity decreases. One anomalous resistivity value (46 Ωm) is observed at 180 m station. From the profile P4 (Fig. 5d), a low apparent resistivity (49 Ωm) appears at the beginning of the profile up to a distance of 50 m. At range distance between 60 m and 150 m, the resistivity increases and reaches 67 Ωm at 150 m position. From this station (150 m), the resistivity decreases for the rest of the profile.

The qualitative interpretation of these curves suggests that each low anomalous value of apparent resistivity observed along each profile, indicate the presence of a conductive zone, probably attributed to a fracture zone. Here we evidenced the presence of conductive zones at positions 70 m, 240 m and 450 m from P1, at positions 180 m, 340 m and 450 m from P2, at position 180 m on P3 and at position 50 m from P4. Along the profiles P1 and P2, these conductive zones were easily interpreted as fracture zones.

5.2. VLF results

For semi-quantitative interpretation and target visualisation, we focus the analysis on positive Karous-Hjelt and Fraser anomalies. Concerning KH filtered data, the apparent current density cross sections plots were produced. Here, the KH plots are represented for two VLF lines type; L3 and L5. The L3 plot (Fig. 6a) shows prominent positive response between 100–125 m, from the beginning of the profile, corresponding to a conductive axis, resulting in a fracture zone, located between 100–125 m, at a depth extending from 30 m to 60 m. The L5 plot (Fig. 6b) reveals a positive anomalous related to the presence of a conductive target between 90–120 m, from the beginning of the profile. It is interpreted as a fracture zone at a deep ranging from 20 m to 60 m. The KH data filtering from the rest of these lines show no pronounced anomalies. The VLF response is more prominent in L5 location. So, the subsurface target could be more interested in this location.

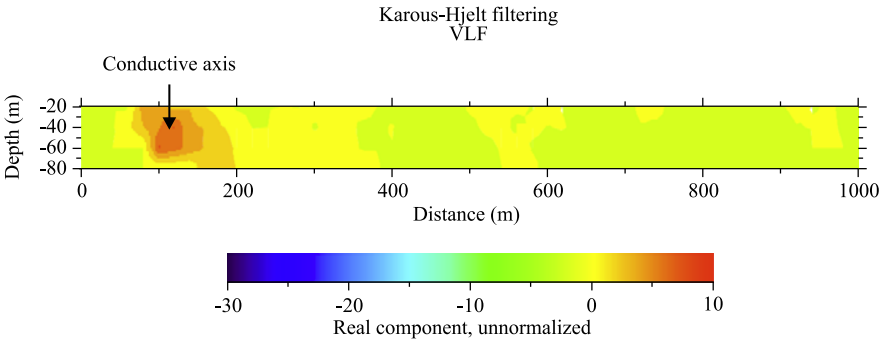

Fig. 6a. Apparent Current density cross section plot of real component data against distance from VLF lines L3 (NE–SW).

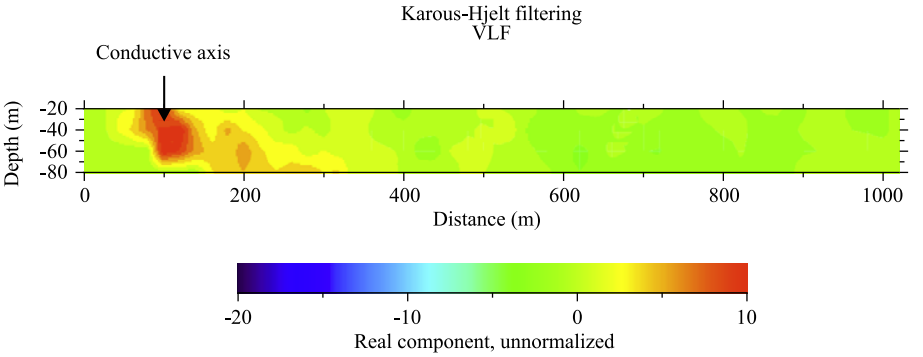

Fig. 6b. Apparent Current density cross section plot of real component data against distance from VLF lines L5 (NE–SW).

The Fraser filtered data are transformed into a contour map (Fig. 7). The Fraser filtered map reveals the presence of anomalies. Two several positive anomalies were distinguished, where the top of the anomalies was observed at L3 and L5 locations. These are related to the presence of conductive structures, interpreted as fracture zones. The low positive Fraser values represent other anomalies, particularly detected at L1 and L5 locations. These are related to other conductive targets, but the VLF response was moderate. Thus, two principal conductive axes oriented NW–SE were identified, which could be the principal fractures in the study area. The rest of anomalies may be associated to secondary conductive axes.

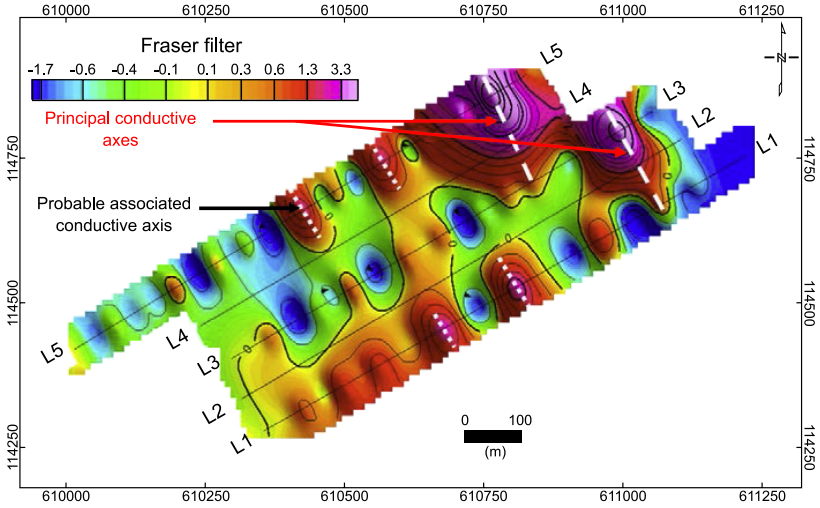

Fig. 7. Interpreted Fraser filtered contour map of real component from five VLF lines.

Taken into account both KH and Fraser filtered data, a 3D model was elaborated (Fig. 8). The model shows two several anomalies, related to the principal fractures zones oriented in NW–SE direction, at L3 and L5 location. The anomaly observed at L3 location is confirmed by the resistivity

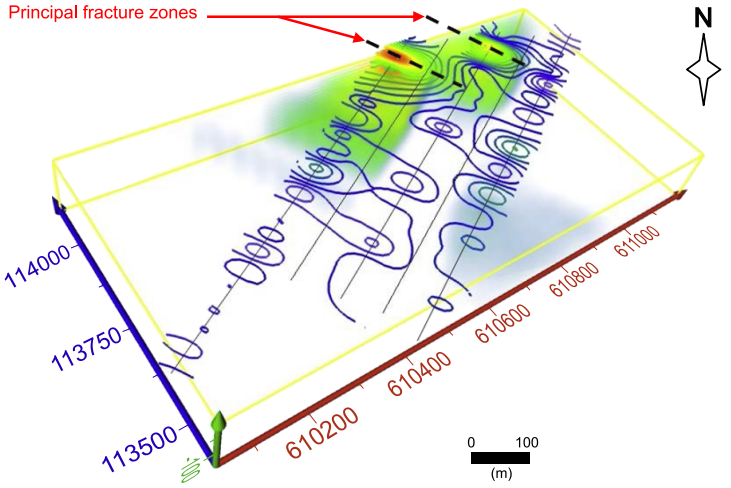

Fig. 8. Interpreted 3D model integrating both Fraser and Karous-Hjelt data filtering.

measurements along the profile P1 (at 70 m station). Integrated resistivity and VLF data confirm that the north part of the prospect area is more fractured, because the resistivity response and the VLF anomalies are more pronounced.

6. Conclusions

In this study, we contributed to the evaluation of the groundwater potential of Zaouia Jdida locality, by detecting fracture zones. Integrated resistivity results and VLF data confirm the presence of subsurface targets. The resistivity measurements revealed the presence of fracture zones at 70 m, 240 m and 450 m positions from the profile P1, at 180 m, 340 m and 450 m positions along the profile P2. The VLF filtered data showed two several anomalies at L3 and L5 locations, resulting in two principal fracture zones, oriented NW–SE, at a deep ranging from 30 m to 60 m. The identified fracture zones constitute the potential zones for hydrogeological practice. Thus, they will have an implication on the movement of groundwater and on its storage in the surveyed area.

Acknowledgements. The authors would like to thank the members of "Agence du Basin Hydraulique d'Errachidia" for the documents made available. Grateful thanks are extended to M. Hritta Driss, Manager of "Société Générale d'Etude et Consult" for the instruments made available. Special thanks are also due to students Ait Bahammou Ismail and Ait Brahim Brahim who helped with the measurements.

References

Amharref M., 1991: Contribution to the hydrogeological study of the valley of the Ziz: The respective effects of drought and the Hassan Addakhil dam on the downstream water resources (Contribution à l'étude hydrogéologique de la vallée de Ziz. Incidence respective de la sécheresse et du barrage Hassan Addakhil sur les ressources en eau en aval). Thesis, Uni. Besançon, 232 p. (in French).

Ammary B., 2007: Geochemical and isotopic study of the main aquifers of the Cretaceous Basibn of Errachidia and the Tafilalt plain (Etude géochimique et isotopique des principaux aquifčres du bassin Crétacé d'Errachidia et de la plaine de Tafilalt). Thesis, Doc. Uni. Med V Agdal, Rabat, 134 p. (in French).

Aoubouazza M., Stichler W., Maloszewski P., 2013: Preliminary Interpretation of Environmental Isotope Data in the Ain El Atti Area (Tafilalt). J. Environ. Anal. Toxicol., **3**, 2, 170, doi: 10.4172/2161-0525.1000170.

Benson A. K., Payne K. L., Stubben M. A., 1997: Mapping groundwater contamination using DC resistivity and VLF geophysical methods–A case study. Geophysics, **62**, 1, 80–86, doi: 10.1190/1.1444148.

Choubert G., 1948: Essay on the paleogeography of Moroccan Mesocretacea (Essai sur la paléogéographie du Mésocrétacé marocain). Volume Jubilaire, Société des Sciences Naturelles du Maroc, 1920–1945, 307–329 (in French).

Choubert G., Faure-Muret A., 1962: Evolution of Moroccan Atlas domain since the Paleozoic times (Evolution de domaine atlasique marocain depuis les temps paléozoïques). In: Durand-Delga M. (Ed.): Livre mémoire P. Fallot, Mém. h. ser. Soc. Géol. France, Paris, 1 447–527 (in French).

Dakir I., Benamara A., Aassoumi H., Ouallali A., Ait Bahammou Y., 2019: Application of Induced Polarization and Resistivity to the Determination of the Location of Metalliferous Veins in the Taroucht and Tabesbaste Areas (Eastern Anti-Atlas, Morocco). Int. J. Geophys., **2019**, Article ID: 5849019, 11 p., doi: 10.1155/2019/5849019.

DRH-GRZ (Direction régionale de l'Hydraulique des bassins Versants Guir-Rheris-Ziz), 2007: Hydrogeological synthesis study of cretaceous Errachidia basin (Etude Synthèse hydrogéologique du bassin crétacé d'Errachidia). Report, 44p. (in French).

Eze C. L., Mamah L. I., Israel-Cookey C., 2004: Very low frequency electromagnetic (VLF-EM) response from a lead sulphide lode in the Abakaliki lead/zinc field, Nigeria. Int. J. Appl. Earth Obs., **5**, 2, 159–163, doi: 10.1016/j.jag.2004.01.004.

Fraser D. C., 1969: Contouring of VLF-EM data. Geophysics, **34**, 6, 958–967, doi: 10.1190/1.1440065.

Karous M., Hjelt S. E., 1977: Determination of apparent current density from VLF measurements: report. Contribution No. 89, Department of geophysics, University of Oulu., p. 19.

Karous M., Hjelt S. E., 1983: Linear filtering of VLF dip-angle measurements. Geophys. Prosp., **31**, 5, 782–794, doi: 10.1111/j.1365-2478.1983.tb01085.x.

Kaya M. A., Özürlan G., Şengül E., 2007: Delineation of soil and groundwater contamination using geophysical methods at a waste disposal site in Çanakkale, Turkey. Environ. Monit. Assess., **135**, 1-3, 441–446, doi: 10.1007/s10661-007-9662-x.

Kirsch R., 2006: Groundwater Geophysics – A Tool for Hydrogeology. Springer-Verlag, Berlin Heidelberg, 548 pp., doi: 10.1007/978-3-540-88405-7.

Kunetz G., 1966: Principles of direct current – resistivity prospecting. Geoexploration Monographs, Number 1, Gebr. Borntraeger, Berlin.

Margat J., 1977: Hydrogeological study of the quaternary basin of Tafilalet (Etude hydrogéologique du bassin quaternaire de Tafilalet). Ressources en Eau du Maroc, 310–380 (in French).

McNeill J. D., Labson V. F., 1991: Geological mapping using VLF radio fields. In: Nabighian M. C. (Ed.): Electromagnetic Methods in Applied Geophysics: Volume 2, Application, Parts A and B. Society of Exploration Geophysicists, 521–640, doi: 10.1190/1.9781560802686.ch7.

Müller I., Gibert J., Laurent R., 1984: Application of geophysical, electro-magnetic VLF (very low frequency) and micro-seismic methods to the study of the karst of Dorvan Cleyzieu (Southern Jura, France) (Application des méthodes géophysiques, électromagnétiques VLF (Very Low Frequency) et micro-sismique à l'étude du karst de Dorvan Cleyzieu (Jura méridional, France)). Bulletin du Centre d'hydrogologie, **5**, 3, Université de Neuchâtel, Centre d'hydrogéologie, 145–162 (in French).

Ogilvy R. D., Lee A. C., 1991: Interpretation of VLF-EM in-phase data using current density pseudosections. Geophys. Prospect., **39**, 4, 567–580, doi: 10.1111/j.1365-2478.1991.tb00328.x.

Saydam A. S., 1981: Very low frequency electromagnetic interpretation using tilt angle and ellipticity measurements. Geophysics, **46**, 11, 1594–1605, doi: 10.1190/1.1441166.

Sharma S. P., Baranwal V. C., 2005: Delineation of groundwater-bearing fracture zones in a hard rock area integrating very low frequency electromagnetic and resistivity data. J. Appl. Geophys., **57**, 2, 155–166, doi: 10.1016/j.jappgeo.2004.10.003.

Vargemezis G., 2007: Interpretation of VLF measurements related to hydrogeological surveys. Bulletin of the Geological Society of Greece, **40**, 2, 593–604, doi: 10.12681/bgsg.16340.

sciendo

Contributions to Geophysics and Geodesy Vol. 49/2, 2019 (195–206)

Seismic activity on the territory of Slovakia in 2017

Róbert KYSEL[1,2,*], Andrej CIPCIAR[1,2], Zuzana CHOVANOVÁ[1,3], Kristián CSICSAY[1], Lucia FOJTÍKOVÁ[1,4], Jozef KRISTEK[1,2]

[1] Earth Science Institute of the Slovak Academy of Sciences, Dúbravská cesta 9, P. O. Box 106, 840 05 Bratislava, Slovak Republic

[2] Faculty of Mathematics, Physics and Informatics, Comenius University in Bratislava, Mlynská dolina, 842 48 Bratislava, Slovak Republic

[3] Faculty of Natural Sciences, Comenius University in Bratislava, Mlynská dolina, Ilkovičova 6, 842 15 Bratislava, Slovak Republic

[4] Institute of Rock Structure and Mechanics of the Czech Academy of Sciences, V Holesovickach 94/41, 182 09, Prague 8, Czech Republic

Abstract: The National Network of Seismic Stations of Slovakia (NNSS) consists of eight short period and five broadband permanent seismic stations and a data centre located at the Earth Science Institute of the Slovak Academy of Sciences (ESI SAS). The NNSS recorded and detected 10 719 seismic events from all epicentral distances in 2017. Totally 73 earthquakes originated in the territory of Slovakia in 2017. This paper provides basic information on the configuration of the NNSS, routine data processing, seismic activity on the territory of Slovakia in 2017 as well as macroseismic observations collected in 2017.

Key words: Slovakia, National Network of Seismic Stations, seismicity, macroseismic observations

1. Introduction

The aim of this paper is to provide a quick overview of earthquakes which originated on the territory of Slovakia or were macroseismically felt on the territory of Slovakia in 2017. The seismic activity on the territory of Slovakia and adjacent areas has been reported on the daily basis by the so called Seismo Reports published on the web sites of the Department of Seismology, ESI SAS `http://www.seismology.sk/Seismo_Reports/reports.html` and in annual reports as a part of the project Partial monitoring system – Geological factors (*Liščák et al., 2018*) which is solved with a contract between ESI SAS and State Geological Institute of Dionýz Štúr.

*corresponding author: e-mail: robert.kysel@savba.sk

doi: 10.2478/congeo-2019-0010

2. Seismic stations operating in 2017

The seismic monitoring of the Slovak territory is provided by the NNSS operated by the ESI SAS (*ESI SAS, 2004*), *Local Seismic Network in Eastern Slovakia* operated by the Faculty of Mathematics, Physics and Informatics of the Comenius University in Bratislava and local network of seismic stations around NPPs Jaslovské Bohunice and Mochovce operated by Progseis Ltd. company. The networks of seismic stations cooperate and the exchange of data is on the regular basis. The positions of the seismic stations on the territory of Slovakia are shown in Fig. 1.

In 2017 the NNSS consisted of thirteen permanent seismic stations, from which eight are short period and five are broadband. Broadband stations are: Červenica (CRVS), Kolonické sedlo (KOLS), Modra (MODS), Vyhne (VYHS) and Železná studnička (ZST). Short period stations are: Hurbanovo (HRB), Izabela (IZAB), Iža (SRO1), Kečovo (KECS), Liptovská Anna (LANS), Moča (SRO2), Stebnícka Huta (STHS) and Šrobárová (SRO). The HRB is the oldest NNSS seismic station that has been in operation since 1909 (*Pajdušák, 1997*). In the year 2017 no significant changes were realized in instrumental equipment of the seismic stations. The NNSS permanent seismic stations and their instrumentation are summarized in Table 1. More

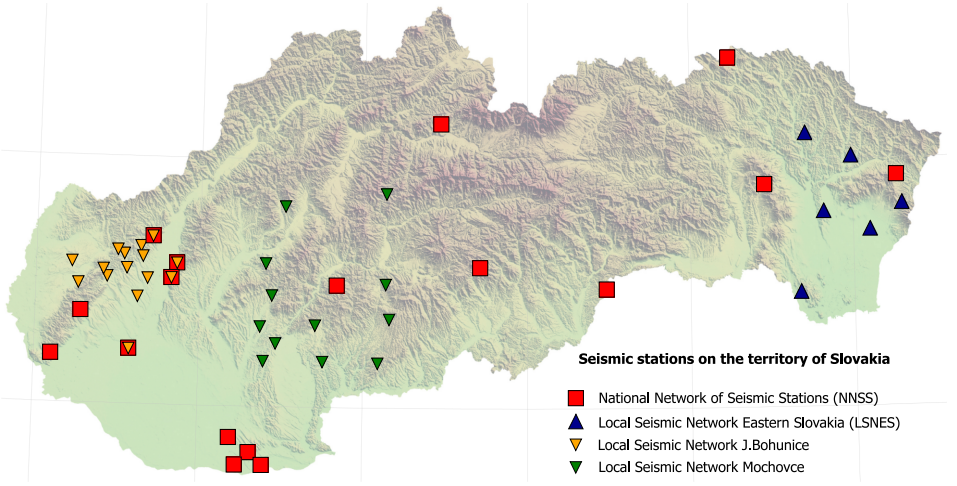

Fig. 1. Seismic stations operational on the territory of Slovakia in 2017.

details can be found on the web page `http://www.seismology.sk/National_Network`.

Table 1. Equipment of seismic stations of the NNSS operating in 2017.

Station	ISC code	Lat. [°N]	Long. [°E]	Alt. [m]	Sensor	DAS	Sampl. freq.	Data format
Bratislava Žel. Studnička	ZST	48.196	17.102	250	3×SKD	Wave24	100/sec	mSEED
Červenica	CRVS	48.902	21.461	476	STS-2	Wave24	100/sec	mSEED
Vyhne	VYHS	48.493	18.836	450	STS-2	Wave24	100/sec	mSEED
Modra-Piesok	MODS	48.373	17.277	520	STS-2	Wave32	100/sec	mSEED
Hurbanovo	HRB	47.873	18.192	115	2× Mainka	Analog	–	smoked paper
Izabela	IZAB	48.569	19.713	450	3×SM3	Wave24	100/sec	mSEED
Iža	SRO1	47.7622	18.2328	111	ViGeo	Gaia	100/sec	mSEED
Kečovo	KECS	48.483	20.486	345	LE3D	Wave24	100/sec	mSEED
Kolonické sedlo	KOLS	48.933	22.273	460	Guralp-6T-30s	Wave32	100/sec	mSEED
Liptovská Anna	LANS	49.151	19.468	710	LE3D	SEMS	100/sec	mSEED
Moča	SRO2	47.763	18.394	109	Guralp-40T-1s	Wave24	100/sec	mSEED
Stebnícka Huta	STHS	49.417	21.244	534	LE3D	Wave24	100/sec	mSEED
Šrobárová	SRO	47.813	18.313	150	3× SKM-3	Wave24	100/sec	mSEED

Four additional short period seismic stations has been operated on the jointly bases of ESI SAS and the other institutions. The seismic stations Banka (BAN), Podolie (POD) and Jalšové (JAL) located in the Little Carpathians have been operated in cooperation with Progseis Ltd. company and the Institute of Rock Structure and Mechanics of the Czech Academy of Sciences (IRSM CAS) (*Fojtíková et al., 2015*). The seismic station Pusté Úľany (PULA) has been operated in cooperation with the IRSM CAS. These stations have been installed as temporary seismic stations.

3. Data processing

Digital data from all NNSS stations (except the analog seismic station HRB) are transferred in real-time to the data centre at the ESI SAS either by the internet or satellite telemetry. Software package SeisComp3 (*Weber et al., 2007*) and SeedLink server are used for data acquisition and exchange.

Beside observations from the NNSS stations the data centre at ESI SAS also use the data from the above mentioned local networks of seismic stations in Slovakia and observations from networks of neighbouring countries: Austrian Seismic Network (*ZAMG – Zentralanstalt für Meterologie und Geodynamik, 1987*), Czech Regional Seismic Network (*Institute of Geophysics, Academy of Sciences of the Czech Republic, 1973*), Hungarian National Seismological Network (*Kövesligethy Radó Seismological Observatory, 1992*), Local seismological network for monitoring NPP Dukovany (*Institute of Physics of the Earth Masaryk University, 2014*), GEOFON Seismic Network (*GEOFON Data Center, 1993*), *Polish Seismological Network*. These stations form a so-called Regional Virtual Network of ESI SAS that consists of approximately 55 seismic stations.

Routine analysis of the digital recordings at the ESI SAS has been performed by the Unix package Seismic handler (*Stammler, 1993*). Interactive locations of seismic events within Seismic Handler are performed by external program LocSat. The collected digital observations are manually processed on the daily basis. The epicentre locations are based on the IASPI91 traveltime curves. Local magnitudes have been determined from the maximum vertical trace amplitudes of Sg waves, using the pre-defined Seismic Handler formula for local events. Continuous raw seismic data from the NNSS are stored in a local archive and seismic data interpretations (together with information on equipment of stations) are stored in a web accessible database.

4. Seismic activity in 2017

The NNSS analyzed 10719 local, regional and teleseismic events in 2017. More than 42200 seismic phases were determined. Seismic events identified as quarry blasts were excluded from further processing and were not included in the event statistics. All events recorded by the NNSS and analyses at the data centre at ESI SAS has been reported in the so called Seismo Reports and published on the above mentioned web sites of the Department of Seismology, ESI SAS.

Altogether 73 seismic events located by the NNSS originated in the territory of Slovakia in 2017 (Fig. 2). Known quarry blasts are not included in this number. 40 earthquakes reached local magnitude 1.0 or more and

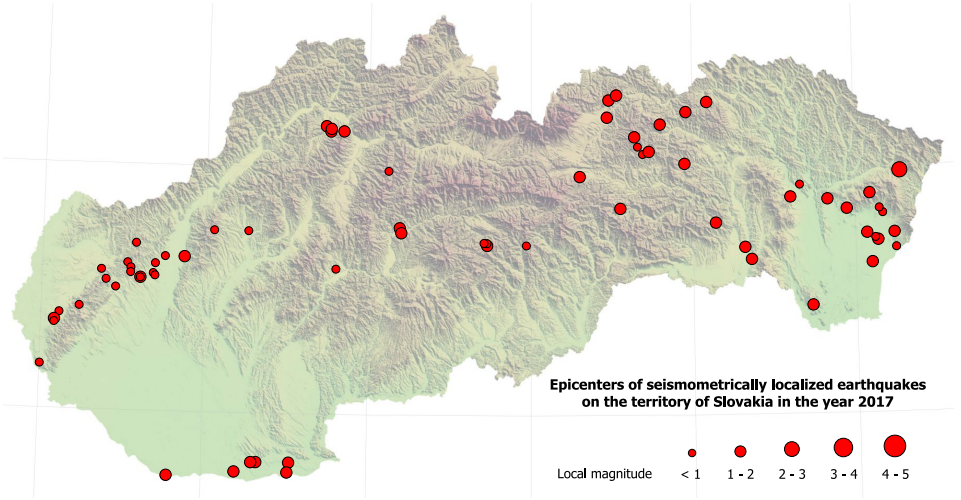

Fig. 2. Map of epicentres of local earthquakes originated on the territory of Slovakia in 2017. Diameters of the circles are proportional to local magnitudes.

are listed in Table 2. The strongest earthquake was detected on June 16 at 13:38 UTC with local magnitude M_L 2.3.

The seismicity of the Slovak territory is dominated by the Little Carpathians and Komárno seismic source zones (*Hók et al., 2016*). The strongest earthquake in the Little Carpathians source zone was detected on the March 25 at 19:11 UTC with local magnitude M_L 1.7. The strongest earthquake in the Komárno source zone was detected on the December 12 at 16:28 UTC with local magnitude M_L 1.8. Although the low level of seismic activity from the last decades remained unchanged also in 2017, these two source zones remain of the primary interest for the monitoring of seismic activity within the territory of Slovakia.

5. Macroseismic observations

Five earthquakes were macroseismically felt on the territory of Slovakia in 2017 (Table 3), all of them with the epicentre on the territory of Slovakia (Fig. 3). These five earthquakes were also seismometrically observed and processed. Intensities were estimated by the European Macroseismic Scale 1998 (EMS-98) introduced by *Grünthal (1998)*.

Table 2. List of earthquakes originated on the territory of Slovakia in 2017 with $M_L \geq 1.0$.

Date [YYYY-MM-DD]	**Origin Time (UTC) [HH:MM:SS]**	**Lat. [°N]**	**Lon. [°E]**	**Depth [km]**	M_L **[NNSS]**	I_0 **[°EMS]**	**Region**
2017-01-21	22:16:21.06	48.36	17.08	0	1.6		Little Carpathians
2017-02-12	08:55:25.40	47.74	17.79	3.3	1.4		Gabčíkovo – Komárno – Štúrovo
2017-02-22	11:59:15.95	47.80	18.53	1.5	1.0		Gabčíkovo – Komárno – Štúrovo
2017-02-23	01:35:37.53	49.15	18.84	0	1.3		Žilina region
2017-03-01	12:36:27.73	48.89	22.09	7.9	1.9		Vihorlat Mts.
2017-03-16	11:29:22.88	48.84	20.55	3.1	1.4		Volovec Mts.
2017-03-17	11:44:02.90	48.87	21.83	0	1.3		Vihorlat Mts.
2017-03-25	19:11:39.40	48.54	17.60	2.6	1.7		Little Carpathians
2017-04-15	04:12:26.38	48.76	19.19	0.1	1.6	3	Banská Bystrica region
2017-04-15	04:23:45.82	48.74	19.20	0	1.4	felt	Banská Bystrica region
2017-04-24	07:31:54.76	48.88	21.60	0.2	1.0		Slanské Hills
2017-05-03	01:49:27.05	48.73	22.24	4	1.5		Vihorlat Mts.
2017-05-14	21:50:06.53	47.76	18.20	4.9	1.4		Gabčíkovo – Komárno – Štúrovo
2017-05-18	10:16:48.78	48.78	21.14	0	1.3		Volovec Mts.
2017-05-26	08:35:03.48	49.13	20.64	0	1.5		Levoča Mts.
2017-05-31	11:55:04.23	48.70	22.14	0	1.3		Eastern Slovak Lowland
2017-06-05	14:32:21.41	49.23	20.96	0	1.5		Čergov Mts.
2017-06-06	08:41:54.08	49.21	20.47	0	1.3		Levoča Mts.
2017-06-07	10:10:28.05	49.27	21.09	0	1.6		Čergov Mts.
2017-06-16	13:38:20.58	48.98	22.28	10.8	2.3		Bukovec Mts.
2017-06-29	15:03:14.18	49.02	20.95	10	1.6		Šariš region
2017-06-30	23:53:22.30	48.69	19.73	0	1.4		Vepor Mts.

Table 2. Continued from the previous page.

Date [YYYY-MM-DD]	Origin Time (UTC) [HH:MM:SS]	Lat. [°N]	Lon. [°E]	Depth [km]	M_L [NNSS]	I_0 [°EMS]	Region
2017-07-13	03:25:02.68	48.73	22.07	7.7	1.6		Eastern Slovak Lowland
2017-08-21	10:37:34.91	48.63	21.36	0	1.1		Slanské Hills
2017-08-21	10:44:09.68	49.18	20.80	0	1.0		Levoča Mts.
2017-09-04	15:30:13.37	48.61	22.10	5.2	1.9		Eastern Slovak Lowland
2017-09-12	14:58:34.96	49.28	20.48	0	1.6		Spiš Magura
2017-10-09	08:14:28.58	48.83	21.95	5.9	1.1		Vihorlat Mts.
2017-10-15	04:06:42.66	49.30	20.53	0	1.2		Spiš Magura
2017-10-23	01:04:11.48	48.97	20.30	0	1.1		Spiš region
2017-10-23	14:42:22.25	48.68	21.32	0	1.1		Košice basin
2017-11-02	11:49:04.77	49.07	20.73	0	1.6		Levoča Mts.
2017-11-10	07:50:48.82	49.17	18.73	0	1.0	felt	Žilina region
2017-11-14	16:22:45.98	49.15	18.76	2.3	1.5	3	Žilina region
2017-11-15	15:34:05.16	48.44	21.73	0	1.2		Zemplén Mts.
2017-12-08	10:33:14.35	47.76	18.52	8.6	1.3		Gabčíkovo – Komárno – Štúrovo
2017-12-11	13:04:56.46	49.16	18.76	0	1.5		Žilina region
2017-12-12	06:53:27.88	48.63	17.87	1.1	1.4		Považský Inovec Mts.
2017-12-12	16:28:32.89	47.80	18.33	10	1.8	3	Gabčíkovo – Komárno – Štúrovo
2017-12-12	23:05:36.16	47.80	18.30	0	1.7		Gabčíkovo – Komárno – Štúrovo

The earthquake on April 15 at 4:12 UTC with epicentre near Banská Bystrica and local magnitude 1.6 was macroseismically felt on 2 locations (Table 4). 5 macroseimic questionnaires were filled. The event was described as a light trembling. The epicentral intensity was determined at 3° EMS-98. The aftershock with local magnitude 1.4 occurred 11 minutes

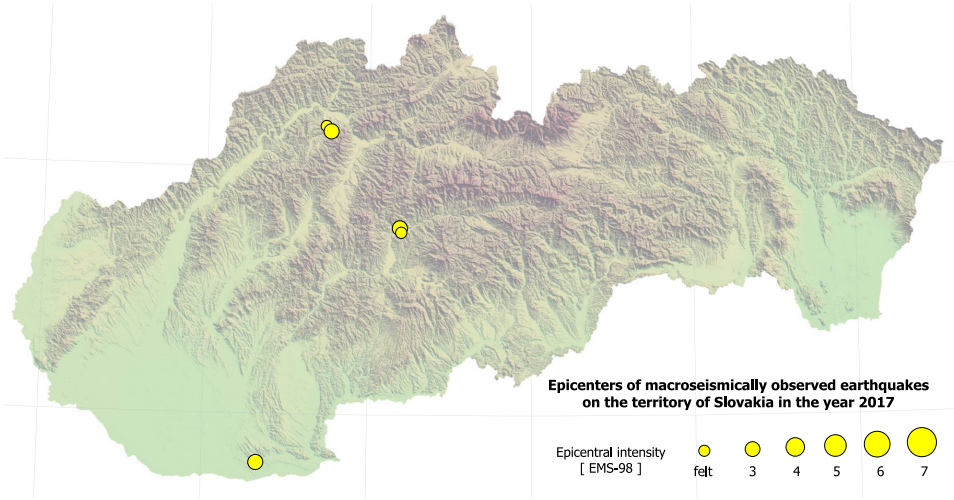

Fig. 3 Map of epicentres of macroseimically observed earthquakes on the territory of Slovakia in 2017. Diameters of the circles are proportional to epicentral intensity.

Table 3. List of macroseismically observed earthquakes on the territory of Slovakia in 2017.

Date [YYYY-MM-DD]	**Origin Time (UTC) [HH:MM:SS]**	**Lat. [°N]**	**Lon. [°E]**	**Depth [km]**	M_L **[NNSS]**	I_0 **[°EMS]**	**Region**
2017-04-15	04:12:26.4	48.76	19.19	0.1	1.6	3	Banská Bystrica
2017-04-15	04:23:45.8	48.74	19.20	0	1.4	–	Banská Bystrica
2017-11-10	07:50:48.8	49.17	18.73	0	1.0	–	Žilina
2017-11-14	16:22:45.9	49.15	18.76	2.3	1.5	3	Žilina
2017-12-12	16:28:32.9	47.80	18.33	10	1.8	3	Komárno

Table 4. Macroseismic observations for April 15, 2017 earthquake, 4:12 UTC.

Locality	**Lat. [°N]**	**Lon. [°E]**	**No. of questionnaires**	I **[°EMS-98]**
Banská Bystrica	48.733	19.143	4	3
Selce	48.764	19.207	1	felt

later at 4:23 UTC. Because of lack of macroseismic data it was not possible to determine the epicentral intensity of the aftershock (Table 5).

The earthquake on November 10 at 7:50 UTC with epicentre near Žilina and local magnitude 1.0 was macroseismically felt on 1 location (Table 6). Because of lack of macroseismic data it was not possible to determine the epicentral intensity.

The earthquake on November 14 at 16:22 UTC with epicentre near Žilina and local magnitude 1.5 was macroseismically felt on 6 locations (Table 7). 27 macroseimic questionnaires were filled. The event was described as a light trembling. Some people reported acoustic effects – light detonation similar to a blast in a distant quarry. The epicentral intensity was determined at 3° EMS-98.

The earthquake on December 12 at 16:28 UTC with epicentre near the village Marcelová (Komárno source zone) and local magnitude 1.8 was macroseismically felt on 1 location (Table 8). 7 macroseimic questionnaires were filled. All people reported acoustic effects – explosion similar to an explosion of a gas cylinder. The event was described as a light trembling. The epicentral intensity was determined at 3° EMS-98.

Table 5. Macroseismic observations for April 15, 2017 earthquake, 4:23 UTC.

Locality	**Lat.** [°**N**]	**Lon.** [°**E**]	**No. of questionnaires**	***I*** [°**EMS-98**]
Banská Bystrica	48.733	19.143	1	felt

Table 6. Macroseismic observations for November 10, 2017 earthquake, 7:50 UTC.

Locality	**Lat.** [°**N**]	**Lon.** [°**E**]	**No. of questionnaires**	***I*** [°**EMS-98**]
Turie	49.149	18.753	1	felt

Table 7. Macroseismic observations for November 14, 2017 earthquake, 16:22 UTC.

Locality	**Lat.** [°**N**]	**Lon.** [°**E**]	**No. of questionnaires**	***I*** [°**EMS-98**]
Turie	49.149	18.753	21	3
Porúbka	49.154	18.725	2	3
Poluvšie	49.121	18.697	1	3
Bytčica	49.178	18.739	1	felt
Lietava	49.170	18.673	1	felt
Lietavská Svinná	49.152	18.675	1	felt

Table 8. Macroseismic observations for December 12, 2017 earthquake, 16:28 UTC.

Locality	**Lat.** [°**N**]	**Lon.** [°**E**]	**No. of questionnaires**	***I*** [°**EMS-98**]
Marcelová	47.792	18.283	7	3

6. Conclusion and discussion

The NNSS is operated by the ESI SAS, Bratislava. Data from all stations (except station HRB) are transferred in real-time to the data centre at Bratislava. Data processing and routine analysis are performed digitally by interactive seismological software Seismic Handler. Digital data are accessible both on-line and off-line in standard data format. So called Seismo Reports of seismic events recorded by NNSS are published on the web page of the ESI SAS `http://www.seismology.sk/Seismo_Reports/reports.html`.

The lack of system approach to financing of the NNSS persisted also in 2017. The costs of NNSS are higher than a financial contribution from the budget of the Slovak Academy of Sciences. Besides this fact, only finances for a day-to-day operation were provided with no amount for an equipment modernization.

Epicentres and local magnitudes were determined for 73 earthquakes originated in the territory of Slovakia in 2017. Weak seismic activity was recorded from several seismic source zones: Little Carpathians., Komárno, Banská Bystrica, Vihorlat Mts. and Levoča Mts.

Acknowledgements. The authors have been supported by the Slovak Foundation Grant VEGA 2/0188/15 and The Slovak Research and Development Agency Grant APVV-16-0146.

References

ESI SAS (Earth Science Institute of the Slovak Academy of Sciences), 2004: National Network of Seismic Stations of Slovakia. Deutsches GeoForschungsZentrum GFZ, Other/Seismic Network, `doi: 10.14470/FX099882`.

Fojtíková L., Kristeková M., Málek J., Sokos E., Csicsay K., Záhradník J., 2015: Quantifying capability of a local seismic network in terms of locations and focal mechanism solutions of weak earthquakes. Journal of Seismology, **20**, 1, 93–106, `doi: 10.1007/s10950-015-9512-1`.

GEOFON Data Center, 1993: GEOFON Seismic Network. Deutsches GeoForschungsZentrum GFZ, Other/Seismic Network, doi: 10.14470/TR560404.

Grünthal G. (Ed.), 1998: European Macroseismic Scale 1998 EMS-98. Cahiers du Centre Européen de Géodynamique et de Séismologie, **15**, Luxembourg, 101 p., online, accessed 6 April 2019, available from: http://gfzpublic.gfz-potsdam.de/pubman/item/escidoc:56109:4/component/escidoc:56108/EMS-98_Original_englisch_pdf.pdf.

Hók J., Kysel R., Kováč M., Moczo P., Kristek J., Kristeková M., Šujan M., 2016: A seismic source zone model for the seismic hazard assessment of Slovakia. Geol. Carpath., **67**, 3, 273–288, doi: 10.1515/geoca-2016-0018.

Institute of Geophysics, Academy of Sciences of the Czech Republic, 1973: Czech Regional Seismic Network. International Federation of Digital Seismograph Networks, Other/Seismic Network, doi: 10.7914/SN/CZ.

Institute of Physics of the Earth Masaryk University (Czech), 2014: IPE_EDU. International Federation of Digital Seismograph Networks, Other/Seismic Network, doi: 10.7914/SN/D1.

Kövesligethy Radó Seismological Observatory (Geodetic and Geophysical Institute, Research Centre for Astronomy and Earth Sciences, Hungarian Academy of Sciences (MTA CSFK GGI KRSZO)), 1992: Hungarian National Seismological Network. Deutsches GeoForschungsZentrum GFZ, Other/Seismic Network, doi: 10.14470/UH028726.

Liščák P., Petro Ľ., Papčo J., Cipciar A., Csicsay K., Kristeková M., Stercz M., Pacajová K., Bednárik M., Briestenský M., Bella P., 2018: Partial Monitoring System – Geological Factors, Subsystem 02: Tectonic and seismic activity of the territory, Geological work number 207, Report for 2017 (Čiastkový monitorovací systém – Geologické faktory, Podsystém 02: Tektonická a seizmická aktivita, číslo geologickej úlohy 207, správa za obdobie: rok 2016), State Geological Institute of Dionýz Štúr, Regional centre Košice, 36, online, accessed 6 April 2019, available from: http://dionysos.gssr.sk/cmsgf/files/Hodn_monitor_2017/02_Tektonicka_aktivita_2017.pdf (in Slovak).

Local Seismic Network of Eastern Slovakia. Faculty of Mathematics, Physics of the Earth and Informatics, Comenius University, html://www.fyzikazeme.sk/mainpage/index_en.htm.

Pajdušák P., 1997: Historical seismic instruments at the stations Hurbanovo (HRB) and Skalnaté pleso (SPC) of Slovakia. Cahiers du Centre Européen de Géodynamique et de Séismologie, **13**, 49–60.

Polish Seismological Network (PLSN), Institute of Geophysics Polish Academy of Sciences, https://www.igf.edu.pl/stacje-en.php.

Stammler K., 1993: Seismichandler—Programmable multichannel data handler for interactive and automatic processing of seismological analyses. Computers & Geosciences, **19**, 2, 135–140, doi: 10.1016/0098-3004(93)90110-Q.

Weber B., Becker J., Hanka W., Heinloo A., Hoffmann M., Kraft T., Pahlke D., Reinhardt J., Thoms H., 2007: SeisComp3 – automatic and interactive real time data processing. Geophysical Research Abstracts In EGU General Assembly, **9**, 09129.

ZAMG – Zentralanstalt für Meterologie und Geodynamik, 1987: Austrian Seismic Network. International Federation of Digital Seismograph Networks, Other/Seismic Network, doi: 10.7914/SN/OE.

sciendo

Contributions to Geophysics and Geodesy Vol. 49/2, 2019 (207–227)

High-precision local gravity survey along planned motorway tunnel in the Slovak Karst

Pavol ZAHOREC[1], Juraj PAPČO[2], Peter VAJDA[1], Stanislav SZABÓ[3]

[1] Division of Geophysics, Earth Science Institute, Slovak Academy of Sciences, Dúbravská cesta 9, P. O. Box 106, 840 05 Bratislava, Slovak Republic; e-mail: zahorec@savbb.sk

[2] Department of Theoretical Geodesy, Faculty of Civil Engineering, Slovak University of Technology, Bratislava, Slovak Republic

[3] DPP s.r.o., Žilina, Slovak Republic

Abstract: Results from a detailed gravity survey realized along the planned highway tunnel in the karstic area of Slovak Karst in the eastern Slovakia are presented. Detailed gravity profiles crossed an area of rugged topography, therefore the terrain corrections played a crucial role in the gravity data processing. The airborne laser scanning technique (LiDAR) was used in order to compile a high-resolution digital terrain model (DTM) of the surrounding area and to calculate terrain corrections properly. The difference between the Bouguer anomalies calculated with an available nationwide DTM and those with new LiDAR-based model can be significant in some places as it is presented in the paper. A new method for Bouguer correction density analysis based on surface data is presented. Special underground gravity measurements in the existing nearby railway tunnel were also conducted in order to determine the mean density of the topographic rocks. The Bouguer anomalies were used to interpret lithological contacts and tectonic/karstic discontinuities.

Key words: detailed gravimetry, terrain correction, LiDAR, DTM, Bouguer correction density

1. Introduction

Two parallel profiles of detailed gravimetric survey were realized in the frame of the detailed engineering geological and hydrogeological exploration in the area of the planned road tunnel of the R2-highway project Rožňava–Jablonov nad Turňou. The planned tunnel is situated in a protected area of the Slovak Karst national park characterized by karstic relief. Gravimetry, as a suitable non-destructive geophysical prospecting method was carried out with the objective of verifying the occurrence of tectonic and karst-

doi: 10.2478/congeo-2019-0011

weathered lineaments and lithological interfaces of blocks with diverse rock densities.

Since the gravity profiles cross a rough terrain relief, the critical component in compiling the complete Bouguer anomalies (CBA) are the near-zone terrain corrections (e.g., *LaFehr et al., 1988; Schiavone et al., 2009*). Recently we have dealt in detail with the topic of computing accurate terrain corrections, especially within the near zone (*Zahorec et al., 2010*). We have developed and we are continuously enhancing our own software for their computation. The most significant requirement for accurate evaluation of terrain corrections is a detailed digital terrain model (DTM) of the given region. For that sake the nearby vicinity of the survey profiles was imaged by air-borne laser scanning (LiDAR). By comparing the LiDAR-derived DTM with the available detailed DMR-3 model based on scanned topographic maps and covering the whole Slovak territory, it is possible to document the high impact of the used LiDAR derived terrain model on the quality of the resulting complete Bouguer anomalies.

Another important element in compiling the complete Bouguer anomalies, especially in rugged terrain, is the choice of the correct topographic density. The correct choice can be assisted by laboratory density analyses of rock samples from boreholes. However, of great value is the analysis of surface gravimetric measurements themselves (*Nettleton, 1939*), and moreover, the utilization of underground gravimetric observations (e.g. *Hammer, 1950*). To precise the estimate of the mean density of rocks of the given region we performed a detailed density analysis based on the approach of *Mikuška et al. (2017)*, as well as we also performed methodological measurements of gravity acceleration in the existing nearby parallel railway tunnel (at the depth of about 200 m below the surface), at spots where the surface gravimetric profiles cross the railway tunnel (*Zahorec and Papčo, 2018*).

Based on constraining geological data from boreholes 2D density vertical sections were constructed that helped to finetune the geological and tectonic structure in the area of the planned tunnel.

2. Site description

The planned tunnel passes through a region, which geomorphologically belongs to the Inner Western Carpathian Subprovince, the Slovak Ore Moun-

tains area, the Slovak Karst unit, with subunits of the Silica Plateau and the Horný vrch Plateau. Geological-tectonic structure of the rock massif is complicated (Fig. 1), manifesting distinctive karstification. The Slovak Karst has a typical karst relief with flat plateaus divided by deep gorges with hollows, lapies, abbyses and caves. The rock environment of the tunnel consists of Early-Middle Triassic rocks of the Silica and Horný vrch plateaus of the Silica Nappe and of Quaternary deluvial-proluvial sediments. The central part of the investigated area is built by massive light-coloured, organogenic, in some places brecciated limestones (mainly Wetterstein and Steinalm types) with karstification features. Less prominent are carbonates of the Gutenstein formation. The marginal parts of the investigated area are built by Szin Beds represented by shales and marlstones that are weakly metamorphosed (phyllitic schists). The Bódvaszilas Beds (schists and sandstones) form the SE part of the region. Both geological and tectonic settings in the investigated area are very complex. We found out that the boundary between Szin and Gutenstein Formation is tectonic. The Gutenstein limestones/dolomites of Silicicum are displaced north-vergently over the Szin

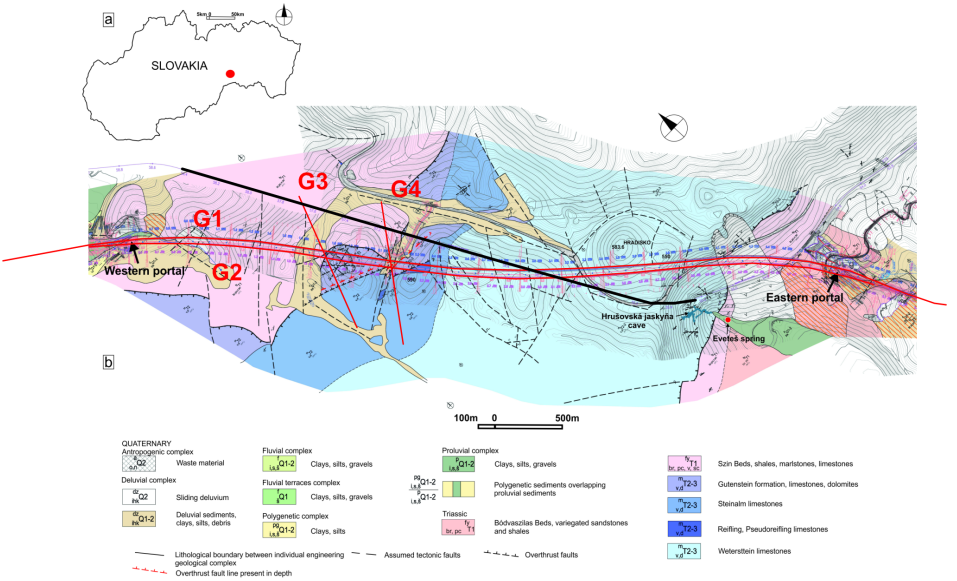

Fig. 1. Engineering geological map of the area (*Szabó in Grenčíková et al., 2018*) with the gravimetric profiles (red curves: the long profiles G1 and G2 are situated along the planned road tunnel tubes) and the trajectory of the railway tunnel (thick black curve).

Beds belonging probably to Turnaicum. The most distinct fault systems in the tunnel area are those of NE–SW and E–W, as well as ESE–WNW direction dipping to the NW and N, fault systems of NW–SE direction dipping to the NE and fault systems of N–S direction dipping to the W and also to the E (Fig. 1). The trajectory of the tracer currents carried away by groundwater currents from the exploration borings towards the Eveteš groundwater source and springs in the Krásnohorska Dlha Lúka locality, that are present along the tunnel route, was due to the NW–SE and E–W, as well as ESE–WNW trending faults.

At a distance of 2.1 km from the western side of the Soroška tunnel, the Szin Beds are tectonically reduced along a steep S-vergent overthrust zone trending E–W to ESE–WNW and dipping to the N, on which Werfenian rocks (Szin Beds) were displaced over the limestone massif. This overthrust zone is permeable and filled with water, (*Szabó et al., 2018*).

The investigated area had been covered by gravimetric mapping in the scale 1:25 000 (4–6 points/km^2) conducted in the period 1965–1975 (*Bárta et al., 1969 in Steiner et al., 1991*). Regional profile gravimetric measurements in a wider vicinity of the investigated area were performed as a part of the project by *Steiner et al. (1991)*. These are, however, of insufficient detail and do not directly reach into our area.

3. Data acquisition and processing

Profile gravimetric measurements were carried out with the step of 10 m totalling 12 km during two observation campaigns. In the first campaign measurements along the two main profiles G1 and G2 were performed above the two projected tunnel tubes. Based on the preliminary results of the first campaign additional measurements of the second campaign were proposed in the form of lateral transverse verification profiles G3 and G4 (Fig. 1).

Positioning of the profile gravimetric stations was conducted by the combination of terrestric measurements (the spatial polar method) by means of the total station Trimble S8 and GNSS measurements (RTK VRS method using the SKPOS service, `http://www.skpos.gku.sk/en/`) by means of the Trimble R10 rover (receiver). GNSS observations of at least 20 sec were taken at each point. The observations were taken in the frame of the ETRS-89 coordinate system and subsequently transformed by the official

transformation procedure (`http://skpos.gku.sk/en/o-skpos.php#uvod`) into the Slovak national reference system S-JTSK coordinate system, realisation JTSK03. Ellipsoidal heights were transformed to the physical heights (Molodenski normal heights) in Baltic vertical reference system 1957 using the Slovak official quasigeoid model DVRM (*Klobušiak et al., 2005*).

Horizontal positions and heights of the majority of the gravimetric points were determined with the accuracy of or better than 0.04 m. Heights above sea level of the gravimetric points range from about 246 to 613 m a.s.l.

3.1. Airborne laser scanning – LiDAR

For the sake of accurate terrain correction calculation in the nearest vicinity of the gravimetric points the region of interest with an area of 6.4 km^2 was scanned by airborne laser scanning technology with the Trimble Harrier 68 system. Processing, adjustment, and filtering of the whole point cloud to the points located on the ground relief (classification "ground") was carried out in software package LAStools v. 170322 (`https://rapidlasso.com/lastools/`). The average point density on the ground reached 12 points/m^2.

The Digital Surface Model (DSM, including vegetation and man-made objects) and the Digital Terrain Model (DTM, needed for terrain correction calculations) were created in software package Surfer v. 13 (`https://www.goldensoftware.com/products/surfer`), with kriging method using a step of 0.5 m, see Fig. 2.

The height accuracy of the resulting model was verified by a set of independent ground control points as well as by gravimetric points. Ground control points were distributed uniformly over the entire scanned region on the site. The differences between the directly observed height and the height interpolated from the DTM at these control points agree at the majority of points to within 0.05 m, which points to a very high quality of the created DTM. Height differences at the majority of gravimetric points are within ±0.15 m. Greater differences occured at points in heavily vegetated locations, or at spots with more extremely rough relief (grikes) and at the margins of the region of interest.

The DTM (Fig. 2 right) served not only for computation of precise terrain corrections, but also for very detailed geomorphologic evaluation of the region, identification of local karst phenomena and tectonic features, etc.

Fig. 3 shows the comparison of our LiDAR-derived DTM with the available nationwide detailed model DMR-3 with the resolution of 10 m (based on scanned topographic maps, *TOPÚ, 2012*).

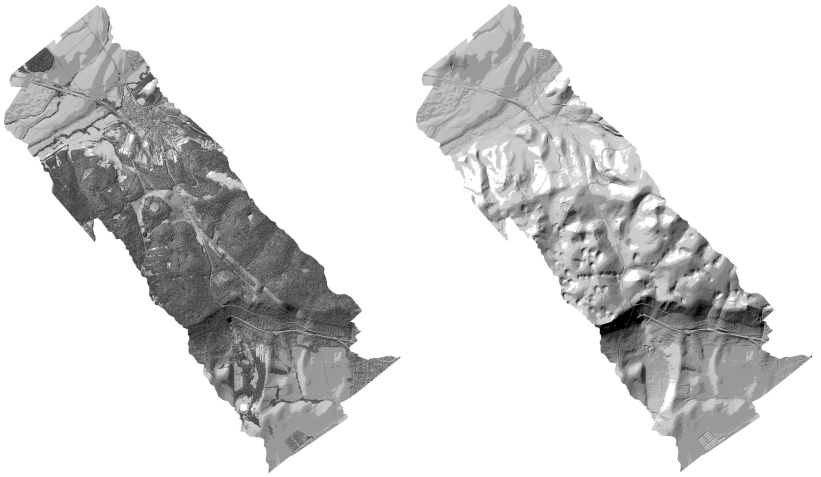

Fig. 2. Comparison of the LiDAR-derived Digital Surface Model (left) and the Digital Terrain Model (right) in our region.

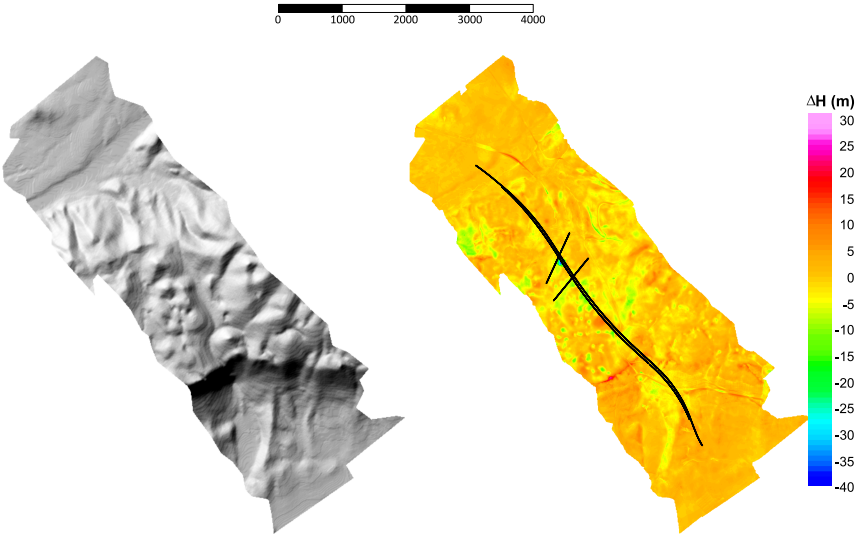

Fig. 3. The available nationwide model DMR-3 (left) and its vertical deviation from the LiDAR DTM (right, cf. Fig. 2). Black curves indicate the gravimetric profiles.

3.2. Gravity data

The measurements of gravity acceleration were carried out by means of the relative gravimeter Scintrex CG-5 during 14 field days in the period November 2016 – April 2017. The measurement were tied two or three times a day to a reference point (situated in the middle of the survey region, easily accessible by car) for the purpose of controlling the drift of the gravimeter. The reference point was tied to the state gravimetric network (point No. 3834.01 Hrhov). The observed gravity values are hence referenced in the valid National reference gravimetric system S-Gr95. The residual daily drifts during our observations (calculated based on repeat measurements at the reference point) ranged from 10 to 60 μGal per day. During each observation day repeated measurements were conducted also at selected gravimetric points on the profiles (about 10% of the overall points) that served for calculating the measurement error. The standard deviation was determined from these repeated measurements at the level of $\pm 10\,\mu$Gal ($1\,\mu\text{Gal} = 10^{-8}\,\text{m/s}^2$).

The values of complete Bouguer anomalies (CBA) were calculated based on the standard procedure:

$$CBA(P) = g(P) - \gamma(P_0) - \delta\gamma_F(P) - \delta g_{sph}(P) + T(P) + \delta g_{atm}(P)\,,$$

where $g(P)$ is the observed gravity (corrected for gravimeter drift and tides) in the S-Gr95 gravimetric system, $\gamma(P_0)$ is normal gravity at the level ellipsoid according to the Pizetti-Somigliana formula with parameters of the reference ellipsoid GRS80, $\delta\gamma_F$ is the height correction (also called free-air correction) with a second order approximation (*Wenzel, 1985 in Torge, 1989*), so that $\gamma(P) = \gamma(P_0) + \delta\gamma_F(P)$ gives the value of normal gravity evaluated at the observation point, $\delta g_{sph}(P)$ is the gravitational effect of the spherical cap with radial (spherical) radius 166.7 km and with thickness equal to the height of the evaluation point P (*Mikuška et al., 2006*) – the so called Bouguer correction, $T(P)$ is terrain correction and δg_{atm} is atmospheric correction computed according to *Wenzel (1985) in Torge (1989)* modified for the territory of Slovakia based on an approximation of the gravitational effect of atmospheric masses which takes into account the real topographic relief (*Mikuška et al., 2008*).

To compute the terrain correction (up to radial distance 166.7 km from the evaluation point P) we used the Toposk software (*Zahorec et al., 2017*).

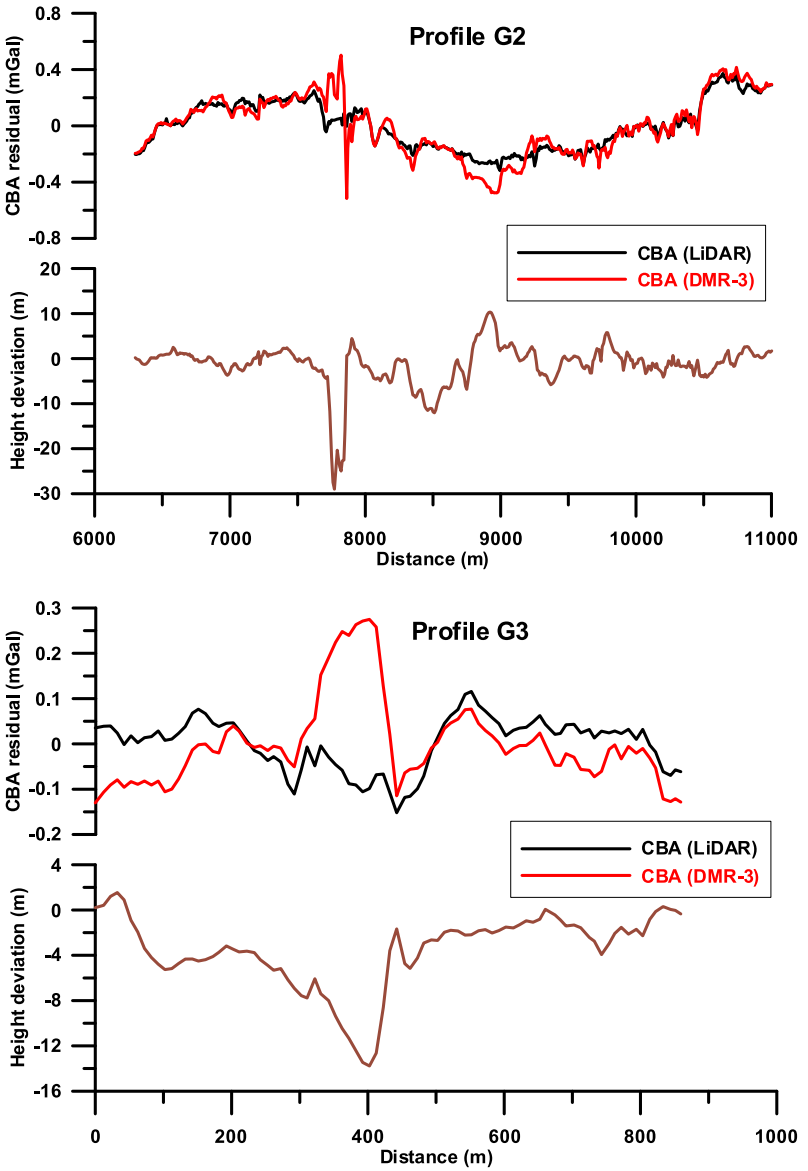

Fig. 4. Two examples of comparison of the residual Bouguer anomalies (upon removal of a linear regional trend, cf. also Fig. 8) computed with terrain corrections T1 from DMR-3 and from LiDAR-DTM. Brown curves are height deviations of gravimetric points from the DMR-3.

The computation is carried out in the usual way in four zones, whereby in each zone a different DTM is adopted, the closer the zone to the point P the more detailed (the higher the resolution of) the model. For the distant zones T31 (5.24–28.8km) ad T32 (28.8–166.7km) we used the SRTM (*Jarvis et al., 2008*) with resolution 3 and 30 arcsec, respectively. For the nearer zones T1 (0–250m) and T2 (250–5240m) we use standardly the above mentioned detailed model DMR-3 (*TOPÚ, 2012*), while in the innermost zone we use the concept of interpolated heights, which reduces the computation error originating from the misalignment of DTM with the real height of measured points (*Zahorec, 2015*). However, for the most accurate computations even this model becomes insufficient. For this reason we have used within the T1 zone the above described DTM obtained from airborne laser scanning. The LiDAR-derived DTM facilitated, as expected, unprecedented accuracy in computing the terrain correction when compared to the use of DMR-3 (Fig. 4). Prominent differences are manifested mainly in the central part of our site, which is characterized by pronounced rough relief (surface mine pit, sinkholes) and in addition it is also forested.

The differences in the computed terrain corrections within T1 (and consequently in CBA) reflect the height deviations of DMR-3 from real heights (brown curves in graphs of Fig. 4). One can see that in critical parts of the profiles significant local false anomalies arise due to the topography deviations. These false anomalies can lead to misinterpretations, as well as to masking the true less pronounced anomalies. Thanks to the roughness of the relief the terrain correction represent the key contribution to the overall interpretation value of the final CBA curves.

3.3. Bouguer correction density analysis based on gravity measurements

For choosing a proper correction density (used in the Bouguer cap term and in the terrain correction) for computing the CBA, we adopt the well known fact that the profiles cross carbonate rocks (mainly limestones), for which we assume that their mean density does not depart significantly from $2.67\,\mathrm{g/cm^3}$. Laboratory density analyses were performed as a part of the engineering geological and hydrogeological prospection, which indicate slightly higher values of the bulk densities (on average about $2.7\,\mathrm{g/cm^3}$). These densities, however, do not account for the contribution of significant karstifica-

tion (karst-weathering) of the rock environment in this region. Therefore we decided to pay close attention to the analysis of the observed gravity data with the objective of estimating the proper correction density. Our analysis originated from data observed along the profiles as well as from additional underground gravity observations conducted for that sake.

3.3.1. Surface gravity data analysis

To estimate the proper correction density, a method arising from visual correlation of CBA curves with topographic relief is often used in practice (*Nettleton, 1939*). In Fig. 5 this method is illustrated for the profile G1. One can see that the CBA curve for correction density of 2.67 g/cm^3 (black) approximately represents the minimum correlation with the terrain relief compared to other CBA curves (compiled with different correction densities).

A more proper and more accurate method can be opted for, which is based on numerical estimate of the correction density making use of Free-Air Anomalies (FAA) and the values of the topographic effect (the Near Topographic Effect – NTE). This approach again requires a more pronounced rugged terrain relief with sufficient height differences between individual points of evaluation (gravimetric points) and at the same time a high-quality DTM for accurate NTE computation. Fig. 6 shows the dependence of the FAA values on the NTE ones (for the density of 1 g/cm^3). The linear regression coefficient corresponds to the value of the sought correction density (*Mikuška et al., 2017*). One can see that the graph constructed from the original FAA vs. NTE values (Fig. 6a) has two "branches", which is caused by the presence of a regional trend in the original FAA values (and also in CBA values, cf. Fig. 7). The branching of the graph deforms the value of correction density (2.61 g/cm^3), therefore it is necessary to remove the regional trend from the data. The first possibility is to determine the regional trend based on the CBA curve (for the assumed density of 2.67 g/cm^3). When we apply the linear trend obtained in such a way to the FAA values, the branching in the graph disappears and the regression coefficient (the correction density) attains a more reliable value of 2.66 g/cm^3 (Fig. 6b).

Another approach to computing regional trend, which we explored, is based on the analysis of the linear tendencies in the FAA and NTE fields

(*Mikuška et al., 2012*). The linear regression coefficient determined from the residual values obtained in such way leads to the value of 2.67 (Fig. 6c), which is very close to the preceding one, and at the same time, corresponds to the realistically anticipated correction density value.

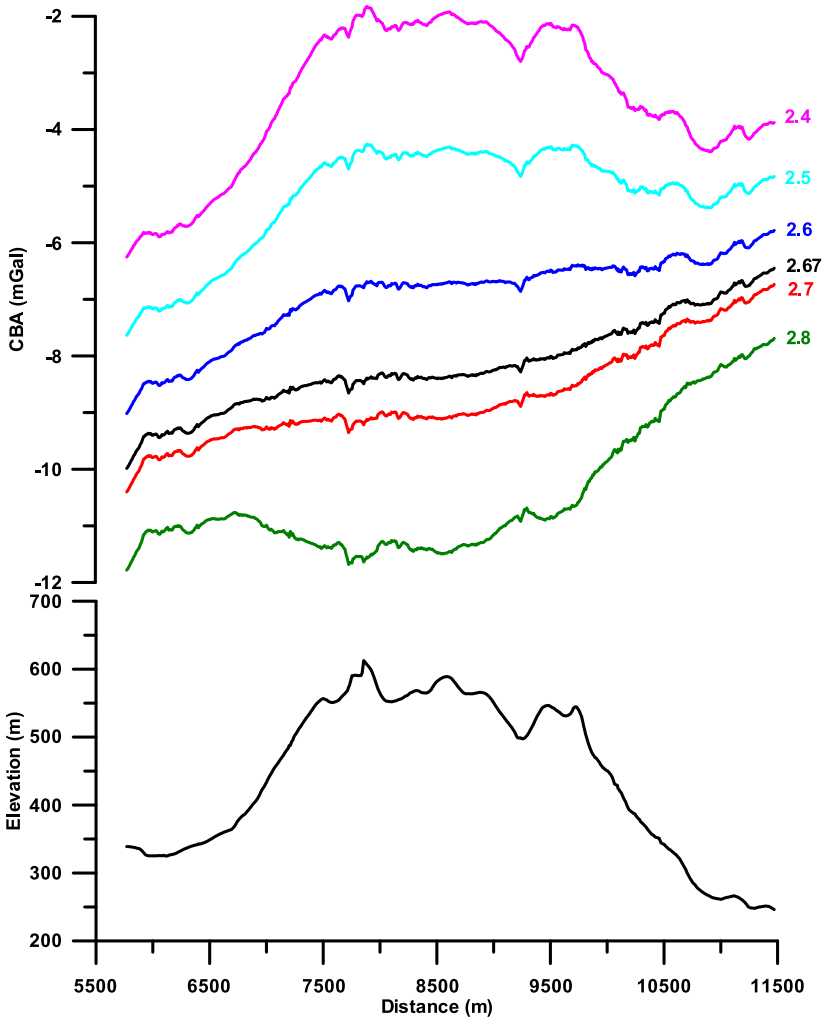

Fig. 5. Approximate selection of the proper correction density based on correlating CBA curves computed for various correction densities (upper graph) with terrain relief (bottom graph) along profile G1.

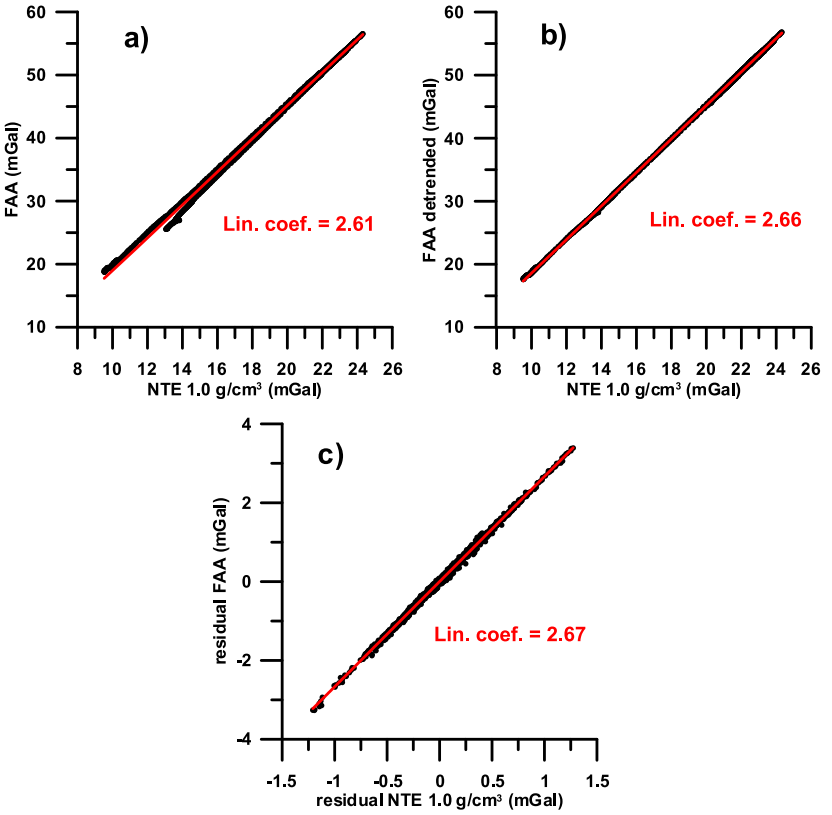

Fig. 6. Estimation of the correction density by means of linear regression coefficient for the dependence of FAA vs. NTE: a) original FAA and NTE values, b) de-trended FAA values (based on regional trend determined from the CBA) and original NTE values, c) residual FAA and NTE values calculated on the basis of the linear tendencies.

3.3.2. Underground gravity data analysis

We took advantage of the presence of the nearby Jablonov railway tunnel and utilized it to carry out underground measurements of gravity. The depth of the railway tunnel tube in the spot where it crosses horizontally the main gravimetric profiles (see Fig. 1) is about 200 m below the surface. This central part of the profiles is respective to geological structure composed of light-grey limestones (Wetterstein limestones) with a lot of karst

phenomena. Based on the difference between the surface gravity and that at vertically projected points inside the railway tunnel we are able to estimate the mean density of the rock massif inbetween the tunnel level and the surface, upon applying respective corrections to the measured gravity due to the gravitational effects of topography, to the tunnel tube void, as well as to the effect of the normal gradient of gravity (*Zahorec and Papčo, 2018*). As a result we obtained the value of 2.66 g/cm^3. Compared to the density received from laboratory analyses this value indicates an obvious karstification of this volumetric domain. At the same time this value is

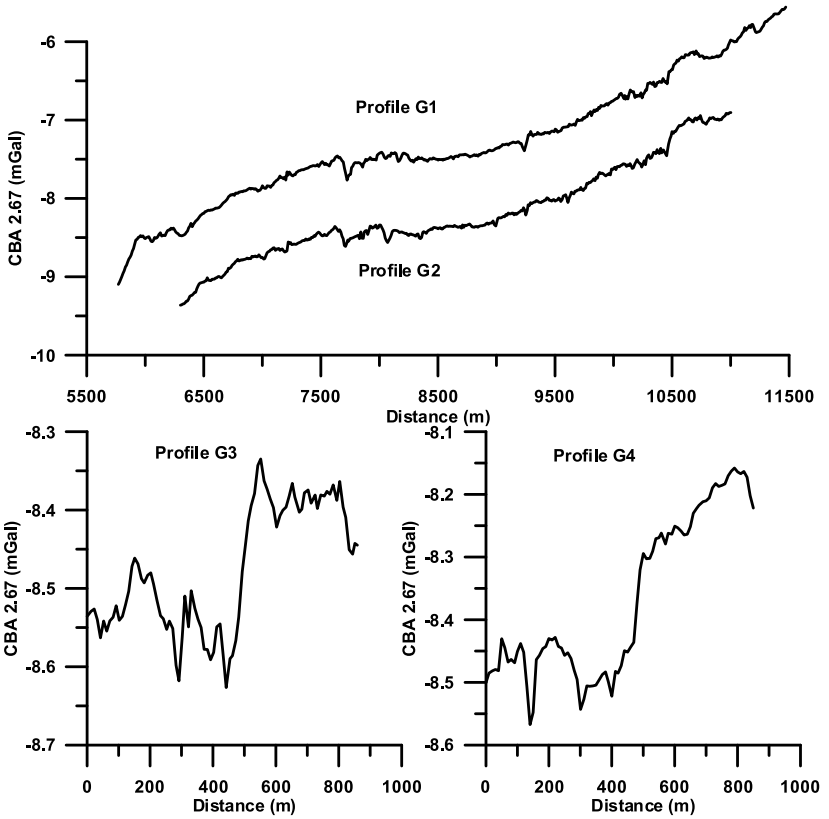

Fig. 7. Complete Bouguer anomaly curves computed with correction density 2.67 g/cm^3. The main profiles G1 and G2 are shown in one graph, but for transparency they are vertically shifted (separated). Note that the additional transverse profiles G3 and G4 have different scales, both vertical and horizontal.

very close to the density values estimated based on the analyses of surface profile gravity measurements. Taking into consideration all the above mentioned approaches, the correction density of $2.67\,\mathrm{g/cm^3}$ was finally adopted for compilation of the CBA curves and for their subsequent interpretation (Fig. 7).

4. Interpretation of gravity measurements

It is clear, upon examining graphs in Fig. 7, that the course of the CBA values along the main profiles G1 and G2 is significantly influenced by a rising regional trend that reflects the deeper geological structure, which is not a part of our subject of exploration. Due to the shape of the curves this regional trend can be approximated by a simple linear function. The removal of the linear trend results in curves of CBA residuals, which constitute the basis for our interpretation (Fig. 8).

The amplitudes of the residual anomalies are very low, at the level of the first tenths of mGal. This is an evidence for the presumed hypothesis that the density differences among the individual rock types in our region of interest are inexpressive. Despite this observation we are able from the qualitative point of view, based on the residual CBA curves, to mark several density (lithological) contacts (interfaces) in the horizontal direction (in the spots of significant gradients in the course of the residual anomalies curves), or alternatively the possible corrupted (weathered, disrupted rock) zones based on the occurrence of sharp local negative anomalies.

A relevant quantitative interpretation can be conducted based on constraining information such as borehole data that facilitate defining approximate spatial geometry of anomalous bodies, to assign geological meaning to them, and to estimate their density parameters, and subsequently to reduce in this way the principal ambiguities of the interpretation. With the help of the said constraining information we have constructed schematic density sections by the method of 2D (profile) density modelling in the Geosoft GM-SYS software environment (`https://www.geosoft.com/products/gm-sys`), which gives us information about lithological structure and about disruption zones. Since the two profiles are close to each other and their density sections exhibit little differences, we show the interpretation of the densiy model only for the longer northern profile G1.

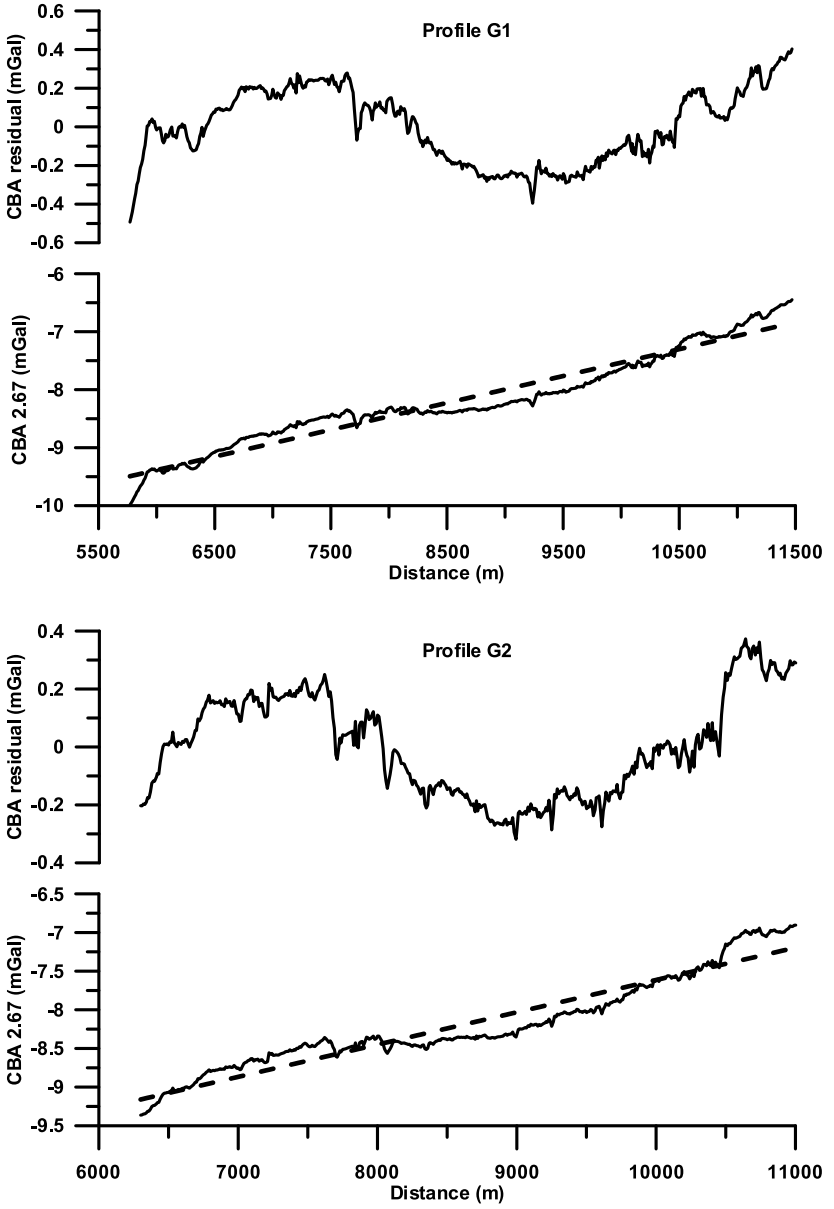

Fig. 8. Residual CBA curves upon removal of linear regional trend (dashed line).

The additional transverse short profiles G3 and G4 were executed for the purpose of verifying the slanted lithological contact in the spots where the profiles cross (see also Fig. 10). The contacts are manifested by steep gravity gradients in CBA curves (Fig. 7, bottom graphs).

4.1. Density modelling along profile G1

On the graph of the residual anomalies (Figs. 8 and 9) one can see that in terms of the whole profile a central wide negative gravity anomaly dominates, which we interpret based on the available geological information as the effect of a robust body of limestones (Wetterstein and Steinalm limestones) affected by karstification. The reduced density of this environment was independently confirmed also by additional subsurface measurements in the nearby railway tunnel. The shape of the contact surface (interface) bordering the surrounding blocks depthwise is finetuned based on information from boreholes. At the eastern side, where this interface is not captured by boreholes, its shape downward is questionable, and we model it as subvertical. We interpret the sharp negative anomaly at footage 9230 m as a disrupted (karstified) zone within the massif, which correlates with the

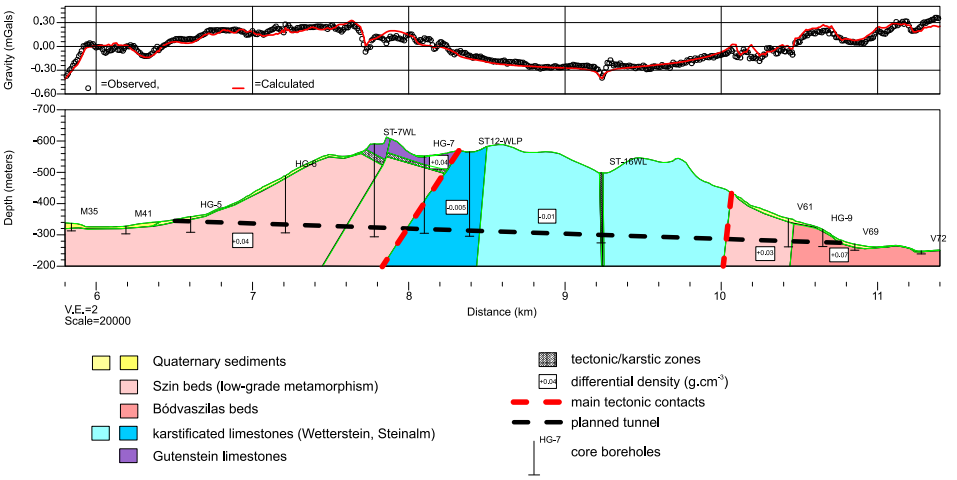

Fig. 9. Cross-section density model of the rock environment along profile G1 (the northern tunnel tube) based on 2D density modelling in GM-SYS software package. Thick red dashed lines indicate the probable tectonic contacts between limestones (Silicicum) and Szin beds (Turnaicum). The vertical scale of the section is magnified by the factor of 2.

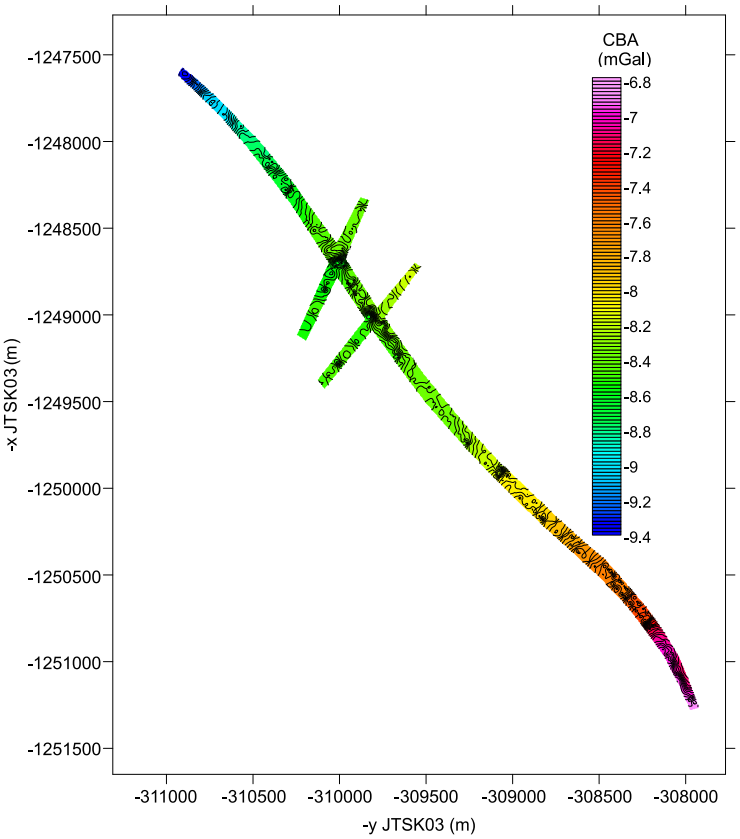

Fig. 10. Quasi-areal map of CBA constructed in the close vicinity of gravity profiles.

occurence of caverns at borehole ST-16WL. The disrupted zone (of W–E elongation) with occurrence of karst phenomena is visible also in the images from airborne laser scanning. The extension of this zone downwards is only schematic.

On both sides of the limestone massif we model bodies with positive differential densities. According to geological cognition they correspond to the so-called Szin beds (marlstones, shales). The reason for their paradoxically higher density relative to the limestones is likely the mentioned karstification of the limestones, and also a low grade of metamorphism of these rocks (phylittic schists), which was revealed by analysis of borehole cores. Our modelling catches a body with the highest differential density

(+0.07 g/cm^3) paradoxically at the end of the profile (beyond footage of about 10 500 m). This we more or less attribute to the marginal deformation of the model, since we know that in the superficial parts of this area the so called Bódvaszilas horizons (shales, sandstones) were identified, for which we do not expect (based on analysis of cores) higher density. But we can expect rocks of higher density below these layers.

In the space at the footage interval from about 7700 to 8300 m we model above the Szin Beds the Gutenstein limestones found in the boreholes. Although we assign to them a slightly higher density (+0.04 g/cm^3), based on published works as well as on borehole core densities, compared to other types of limestones, due to their identified low thickness they have a low gravitational signature. They are significantly tectonically limited from the west (a sharp negative anomaly at around 7720 m of footage), where we interpret a significant disruption zone. Its downward course we model based on the borehole core results.

From the qualitative viewpoint what is interesting regarding the CBA curve is a steep gravity gradient (rise) at the beginning of the profile (footage of about 5900 m). This contact we model by increased thickness of quaternary sediments. However, there is a possibility that it can be caused already by the contact with Neogene filling of the basin.

We interpret several less pronounced negative anomalies along the profile (at about 6200 to 6500 m, then 10700 to 11000 m, and also 11200 to 11300 m) by a varying thickness and character of of quaternary sediments, which despite their low thicknesses generate measureable effects, as we assign to them high differential densities (−0.5 to −0.7 g/cm^3), the highest among all lithological types.

We can make use of the fact that the profiles run close to each other. We correlate between them the more pronounced density contacts to gain an idea about their course in horizontal direction. In Fig. 10 we show the quasi-areal map of the CBA constructed based on measurements along all profiles (including the transversal ones), which yields in the close vicinity of the profiles quasi-areal information about the course (shape) of density interfaces, based on the course (shape) of the isolines. Of course we emphasize that this is very limited areal information and it is not possible to extrapolate it outside of the close vicinity of the gravity profiles. Despite its limitation, such areal view yielded several interesting additional pieces

of information. For instance the course (shape) of isolines between profiles G1 and G2 in spots where the transversal profiles cross indicated that at those spots the density interfaces are either in oblique or in sub-parallel orientation to the profiles, which was one of the reasons to select the location of the transverse profiles at these spots. Similar is the situation at the SE margin of the profiles, where the course (shape) of the isolines also indicates a parallel course of density interfaces, which has been documented also in existing boreholes. Such knowledge reinforces the awareness of weaknesses of the 2D modeling approach at such spots where the model can deviate significantly from reality.

5. Conclusions

The presented results of the detailed gravimetric exploration in demanding rugged karst terrain demonstrated the potential of detailed interpretation when using a modern approach to computing terrain corrections based on a DTM acquired by airborne laser scanning (LiDAR) of the surrounding region. Terrain corrections have proved to be the key factor from the viewpoint of the quality of processing and interpretation of gravimetric observations in mountainous or hilly terrain. Another important aspect is the choice of proper correction density for computing the complete Bouguer anomaly (CBA). A detailed density analysis of surface gravity data based on correlating the free air anomalies (FAA) with the topographic effect yields reliable estimate of the correction density, whereby it is in agreement with the classical method according to Nettleton. The underground gravity observations carried out in a nearby parallel railway tunel proved to be an independent confirmation of the correctness of the selection of the correction density. All of the applied approaches confirmed that the assumed density of $2.67\,\mathrm{g/cm^3}$ was correct. In addition, this finding confirmed the well known fact that the estimate of the correction density acquired in this way may disagree with the results of laboratory density analyses of rock samples.

The results of 2D density modelling supported by borehole data yielded information about density (lithological) properties, as well as about assumed disruption zones en-route the planned Soroška tunnel trajectory. As the most significant finding of our exploratory survey we consider the density distinguishing of the blocks of the massive karstified limestones from the

(weakly metamorphosed) Szin Beds. An important contribution is also the mapping (delineation) of more pronounced zones of disruption that underwent the anticipated karstification. The small mutual separation of the profiles facilitates also areal view (though very limited) on the course (shape) of the investigated interfaces (contact surfaces). This view indicates that the courses (angles) of the lithologic contacts are of a variety of orientations with respect to the course of the planned tunnel. This variety of orientations becomes also a limiting factor for the 2D approach to modelling.

Acknowledgements. This work was carried out under contract by DPP Ltd. (contract No. I./452/2016/R). This work was partially supported also by Vega grant agency under project No. Vega 1/0462/16. We are grateful to Jana Bučová for her assistance with contract realisation.

References

Grenčíková A., Szabó S., Copláková J., Majerčák J., Moravanský D., Mitter P., Gaži P., Bučová J., Otruba M., Sklenárová D., 2018: Highway R2 Rožňava – Jablonov nad Turňou. Detailed engineering geological and hydrogeological survey. Final report, DPP, Žilina (unpublished; in Slovak).

Hammer S., 1950: Density determination by underground gravity measurements. Geophysics, **15**, 4, 637–652, doi: 10.1190/1.1437625.

Jarvis A., Reuter H. I., Nelson A., Guevara E., 2008: Hole-filled SRTM for the globe Version 4, available from the CGIAR-CSI SRTM 90m Database: http://srtm.csi.cgiar.org.

Klobušiak M., Leitmanová K., Ferianc D., 2005: Realization of obligatory transformation between national coordinates and height reference system into ETRS89. Proceedings of the International Conference Tatry 2005 (in Slovak).

LaFehr T. R., Yarger H. L., Bain J. E., 1988: Comprehensive treatment of terrain corrections with examples from Sheep Mountain, Wyoming. 58th Ann. Internat. Mtg., Soc. Explor. Geophys., Expanded Abstacts, 361–363, doi: 10.1190/1.1892191.

Mikuška J., Pašteka R., Marušiak I., 2006: Estimation of distant relief effect in gravimetry. Geophysics, **71**, J59–J69, doi: 10.1190/1.2338333.

Mikuška J., Marušiak I., Pašteka R., Karcol R., Beňo J., 2008: The effect of topography in calculating the atmospheric correction in gravimetry. SEG Las Vegas 2008 Annual Meeting, SEG Technical Program Expanded Abstracts, 784–788.

Mikuška J., Marušiak I., Pašteka R., Bielik M., 2012: Linear tendencies intrinsic to the Bouguer anomalies in areas of topographic relief. SEG Las Vegas 2012 Annual Meeting, SEG Technical Program, Expanded Abstracts, 1–5.

Mikuška J., Zahorec P., Papčo J., Karcol R., Marušiak I., 2017: Surface rock density interpretation from detailed gravity measurements based on free-air anomalies and near topographic effects in a terrain with sufficient relative relief. XII Slovak Geophysical Conference, 28–29 September, 2017, Bratislava (oral, abstract).

Nettleton L. L., 1939: Determination of density for reduction of gravimeter observations. Geophysics, **4**, 3, 176–183, doi: 10.1190/1.0403176.

Schiavone D., Capolongo D., Loddo M., 2009: Near-station topographic masses correction for high-accuracy gravimetric prospecting. Geophys. Prospect., **57**, 4, 739–752, doi: 10.1111/j.1365-2478.2009.00799.x.

Steiner A., Kandrík M., Mikuška J., Mello J., Šefara J., Bujňáková M., Gnojek I., Filo M., Kubeš P., Halmešová S., Marušiaková D., Pospíšil L., Zima L., Krčmář B., 1991: Map of geophysical indications and interpretations. Slovenský kras region. Final report, Geofyzika Bratislava s.e., division Spišská Nová Ves (unpublished; in Slovak).

Szabó S., Copláková J., Soták J., Majerčák J., Otruba M., Moravanský D., Mitter P., Gaži P., Bučová J., Grenčíková A., Malík P., 2018: Engineering-geological, geotechnical and hydrogeological parameters of the Soroška tunnel rock sequences. Mineralia Slovaca, **50**, 101–124.

TOPÚ – Topographic Institute, 2012: Digital terrain model version 3 (online). http://www.topu.mil.sk/14971/digitalny-model-reliefu-urovne-3-%28dmr-3%29.php.

Torge W., 1989: Gravimetry, W de G, Berlin, New York.

Zahorec P., Pašteka R., Papčo J., 2010: The estimation of errors in calculated terrain corrections in the Tatra Mountains. Contrib. Geophys. Geod., **40**, 4, 323–350, doi: 10.2478/v10126-010-0014-4.

Zahorec P., 2015: Inner zone terrain correction calculation using interpolated heights. Contrib. Geophys. Geod., **45**, 3, 219–235, doi: 10.1515/congeo-2015-0021.

Zahorec P., Marušiak I., Mikuška J., Pašteka R., Papčo J., 2017: Numerical Calculation of Terrain Correction Within the Bouguer Anomaly Evaluation (Program Toposk), 79–92. In book: Pašteka R., Mikuška J., Meurers B (eds): Understanding the Bouguer Anomaly: A gravimetry Puzzle. Elsevier, ISBN 978–0-12–812913–5.

Zahorec P., Papčo J., 2018: Estimation of Bouguer correction density based on underground and surface gravity measurements and precise modelling of topographic effects – two case studies from Slovakia. Contrib. Geophys. Geod., **48**, 4, 319–336, doi: 10.2478/congeo-2018-0015.